

APPROVAL SHEET

Title of Dissertation: Analysis of Sensory Feedback in the Lamprey  
Central Pattern Generator for Locomotion

Name of Candidate: Nicole S. Massarelli  
Doctor of Philosophy, 2016

Dissertation and Abstract Approved: \_\_\_\_\_

Dr. Kathleen Hoffman

Professor

Department of Mathematics and Statistics

Date Approved: \_\_\_\_\_

[ABSTRACT]

Title of dissertation: Analysis of Sensory Feedback in the Lamprey Central Pattern Generator for Locomotion

Nicole S. Massarelli, Doctor of Philosophy, 2016

Dissertation directed by: Dr. Kathleen Hoffman  
Department of Mathematics & Statistics  
University of Maryland, Baltimore County

Sensory feedback is an integral part of the complex closed-loop system of locomotion. Lampreys are model organisms for vertebrate locomotion. Lamprey locomotion is driven by a central pattern generator (CPG), a circuit of neurons located in the spinal cord that produces a traveling wave of neural activity that innervates muscles for swimming. The CPG is capable of producing this activity independently of descending control or sensory feedback, however, sensory feedback is essential in responding to perturbations and adjusting the CPG output. Our goal is to model sensory feedback from edge cells, proprioceptor organs on the margin of the spinal cord, to the lamprey CPG in order to complete a closed-loop model of lamprey swimming.

Entrainment is a property of the CPG where the rhythmic output of the CPG will tend to approach the same frequency as a periodic stimulus. The lamprey CPG is modeled using a chain of coupled oscillators, where each oscillator corresponds to an anatomical segment of the spinal cord. We model entrainment experiments in two CPG models: a neural model where unit oscillators are represented by several classes of cells and a derived phase model where unit oscillators are represented by a single variable, its phase. In both models we included the effects of bending by including input from edge cells at the

location of the forced oscillator. Both models required asymmetry in the ascending and descending connection strengths in order to qualitatively match experimental entrainment data. Additionally, we showed that the model agreed with experimental results that the CPG is highly robust in response to large levels of noise added to the bending signal.

From a different perspective, we experimentally record edge cell activity, and analytically characterized edge cells responses to ramp bending experiments. While some cells respond to static stretch, the strongest responses are seen during the active periods of stretch when movement was occurring. We further used frequency domain techniques, for both the experimental data and model simulations, to compute a map, called the harmonic transfer function, from perturbations of the input signal to changes in the output signal. Results reveal that an under-damped harmonic oscillator with phase dependent forcing that depends on the sinusoidal bending captures key features of the experimental data, and thus, represents the mapping from bending to edge cell output.

Analysis of Sensory Feedback in the Lamprey Central Pattern Generator for  
Locomotion

by

Nicole S. Massarelli

Dissertation submitted to the Faculty of the Graduate School of the  
University of Maryland, Baltimore County in partial fulfillment  
of the requirements for the degree of  
Doctor of Philosophy  
2016

Advisory Committee:  
Dr. Kathleen Hoffman  
Dr. Tim Kiemel  
Dr. Eric Tytell  
Dr. Brad Percy  
Dr. Hye-Won Kang  
Dr. Phyllis Robinson

© Copyright by  
Nicole S. Massarelli  
2016



*To...*

To my parents who supported and encouraged me to continue my education and persevere through all the stressful milestones along the way. I could not have done it without you.

## Table of Contents

List of Figures	v
List of Abbreviations	xi
<b>1 Introduction</b>	<b>1</b>
1.1 Properties of the Lamprey CPG	3
1.2 Mathematical Models of CPGs	5
1.3 Sensory Feedback and Entrainment	9
1.4 Forced Chains of Coupled Oscillators	11
1.5 Edge Cells	15
1.6 Outline of Work	16
<b>2 CPG Models and Entrainment</b>	<b>19</b>
2.1 Overview	19
2.2 Neural Model	20
2.3 Derived Phase Model	23
2.3.1 Coupling Functions	28
2.3.2 Forcing Connections	32
2.4 Entrainment Ranges	33
2.4.1 Entrainment Ranges as a Function of Forcing Strength	35
2.4.2 Entrainment Ranges as a Function of Forcing Position	38
2.5 Loss of Entrainment	40
2.6 Discussion	45
<b>3 Stochastic Entrainment</b>	<b>49</b>
3.1 Overview	49
3.2 Noisy Bending Experiments	50
3.3 Modeling Noisy Bending Experiments	55
3.4 Stochastic Entrainment Ranges	57
3.5 Discussion	60
<b>4 Role of Edge Cells During Entrainment</b>	<b>66</b>
4.1 Overview	66
4.2 Mechanosensory Neurons	67
4.3 Experimental Methods	68
4.4 Spike Sorting	69

4.5	Response to Bending Angle and Bending Velocity . . . . .	71
<b>5</b>	<b>Frequency Domain Analysis</b>	<b>81</b>
5.1	Overview . . . . .	81
5.2	Frequency Response Functions . . . . .	82
5.3	FRF and IRF for Edge Cell Activity . . . . .	92
5.4	Fitting Frequency Response Function . . . . .	94
5.5	Harmonic Transfer Functions . . . . .	96
5.6	Modeling the Phase-Dependent Impulse Response . . . . .	102
<b>6</b>	<b>Conclusions and Future Work</b>	<b>105</b>
6.1	Modeling Entrainment . . . . .	105
6.2	Modeling Entrainment with Sensory Perturbations . . . . .	106
6.3	Edge Cell Response During Swimming . . . . .	108
6.4	Future work . . . . .	111

## List of Figures

1.1	Schematic of the different tracts seen in the excised lamprey spinal cord. Note ventral roots occur periodically on the left and right sides of the notochord right under the spinal cord. . . . .	4
2.1	Connectivity of one segmental oscillator. Cell classes are excitatory interneurons (E), lateral inhibitory interneurons (L), crossed inhibitory interneurons (C), and edge cells (EC). Bars and circles indicate excitatory and inhibitory connections, respectively. We assume edge cells are only active in the segment at which bending occurs. . . . .	23
2.2	Stain of an edge cell showing the dendrites synapsing onto the side of the spinal cord and the axon extending down the lateral tract. Image courtesy of Tytell and Buchanan (2015). . . . .	23
2.3	Steady state solution of the cell voltages in the first segment of a chain of coupled oscillators defined by (2.1) for two cycles without forcing. For this simulation weak intersegmental coupling, defined by $A_a = 0.0004$ , $A_d = 0.0002$ , and $\lambda_a = \lambda_d = 4$ , was used to connect oscillators. Since weak coupling was used, the simulation provides a good approximation of the voltages within a single segment of an uncoupled oscillator. Note the spatiotemporal symmetry between left and right cells. The voltage of the left cells is the same as the voltage of the right cells except for a phase shift of half a period. . . . .	25
2.4	The PRCs are plotted for the left E, L, and C cells. Each PRC describes the resulting phase shift that occurs when that cell's voltage is perturbed by $10^{-6}$ , at various initial phases. PRCs for right E, L and C cells are the same except for a phase shift of 0.5 due to the right-left symmetry within each oscillator. . . . .	30
2.5	For each type of neural connection between E, L, and C cells, an $H_c$ function is computed to represent the effects of neurons on the voltage of the neuron within the oscillator. The six $H_c$ functions are computed for connections from L to E cells, C to E cells, C to L cells, E to C cells, L to C cells, and C to C cells. These six connections represent only half of the neuron-to-neuron connections in Figure 2.1 since the other six connections can be determined from the left-right symmetry within each oscillator. . . . .	31
2.6	Relative strengths $\alpha_{rc}/\alpha_r$ of different connection types as a function of connection length $r$ and connection type $c$ . . . . .	31

2.7	For each type of neural connection from edge cells, an $H_{f,c}$ function is computed that describes the strength of that connection as a function of relative phase between the edge cell and the oscillator where forcing is applied. . . . .	32
2.8	Illustration of our elliptical two-parameter continuation method used to find entrainment ranges as a function of forcing strength. The dotted circles denote how the values of $\delta = \omega_f - \omega_0$ and $\alpha_f$ are updated at each continuation step. The plus signs denote points on the entrainment range that are detected by the continuation circles. This allows us to detect sharp corners that may be missed with standard one-parameter continuation. . . . .	35
2.9	Entrainment ranges for the neural and derived phase models as a function of forcing strength. Figure 2.9A on the left illustrates entrainment ranges as a function of forcing strength for weak intersegmental coupling corresponding to $A_a = 0.0004$ , $A_d = 0.0002$ , and $\lambda_a = \lambda_d = 4$ . Figure 2.9B on the right illustrates entrainment ranges for 100 times stronger intersegmental coupling with $A_a = 0.04$ and $A_d = 0.02$ . Note that the size of the entrainment range scales with the coupling strength, that is, the entrainment ranges in B are 100 times larger than the entrainment ranges shown in A. For weak coupling the entrainment ranges for the neural and derived phase models match closely while for strong coupling the entrainment ranges start to differ as forcing strength increases. The dashed line on both plots represents Hopf bifurcations that occur when entrainment is lost. Smooth lines denote saddle-node bifurcations. The arrows in Figure 2.9B correspond to the forcing strength values $\alpha_f$ where loss of entrainment is depicted in Figures 2.12. . . . .	36
2.10	Entrainment ranges as a function of forcing position for varying intersegmental connections. Uniform coupling asymmetry is illustrated in A with $A_a = 0.0004$ , $A_d = 0.0002$ , and $\lambda_a = \lambda_d = 4$ . All of the ascending coupling strengths are stronger than descending for all connection lengths. This coupling scheme is used to produce monotonic entrainment ranges as a function of forcing position, seen in C. Nonuniform coupling asymmetry is depicted in B with $A_a = 0.006$ , $A_d = 0.0004$ , $\lambda_a = 0.75$ , and $\lambda_d = 4$ . For our choice of parameters, ascending connections become stronger at connections of length 3. Nonuniform coupling is used to compute the entrainment range in D, where see non-monotonic entrainment ranges. . . . .	37
2.11	Entrainment ranges as a function of forcing position for varying intersegmental connections in the neural model. Figure 2.11a shows the entrainment range for strong uniform coupling asymmetry with $A_a = 0.04$ , $A_d = 0.02$ , and $\lambda_a = \lambda_d = 4$ . Figure 2.11b shows the entrainment range for strong nonuniform coupling asymmetry with $A_a = 0.6$ , $A_d = 0.04$ , $\lambda_a = 0.75$ , and $\lambda_d = 4$ . Note that even with strong intersegmental coupling the neural model requires nonuniform coupling asymmetry to produce non-monotonic entrainment ranges. . . . .	39

2.12	Comparison of loss of entrainment for the neural (A-D) and derived phase (E-H) models. Figures 2.12A and E show phase relative to the forcer for external loss of entrainment with $\alpha_f = 0.5$ and $\omega_f - \omega$ is $+0.0002$ above the entrainment range as indicated by arrow 1 in Figure 2.9B, where A is a simulation of the neural model and E is a simulation of the derived phase model. Figures 2.12C and F show relative phase for internal loss of entrainment with $\alpha_f = 2$ and $\omega_f - \omega$ is $+0.0002$ above the entrainment range indicated by arrow 2 in 2.9B. Figures 2.12B and F and 2.12D and H show cycle period for external and internal loss of entrainment respectively. . . .	43
3.1	Experimental recordings from ventral roots along the excised lamprey spinal cord in a bath of neurotransmitter. Figure A shows the experimental recording configuration. Glass suction electrodes are used to record from ventral roots along the notochord while bending the spinal cord back and forth. The three large arrows indicate three suction electrodes placed at different locations along the spinal cord. The smaller triangles indicate where the spinal cord was pinned down in the bath. The double set of pins to the right of arrows 2 and 3 denote the point of bending. Figure B shows a sample recording of the ventral root signals from segments along the spinal cord at positions indicated by the arrows in A for a stationary spinal cord without bending. . . . .	51
3.2	Comparison of experimental data from one section of the spinal cord with a deterministic sinusoidal forcing signal (A-C) and noisy sinusoidal forcing (D-F) applied to the last segment. Figures A, D show the relationship of the sinusoidal bending to the ventral root recording. Figures B, E show that the oscillators have entrained to the 1.6 Hz forcing frequency. Figures C, F show the phase of the spikes relative to the forcing frequency. The noisy bending produces figures very similar to deterministic bending, indicating the lamprey CPG is robust to noise. . . . .	53
3.3	Simulation of the derived phase model with sinusoidal (A-D) and noisy sinusoidal (E-H) forcing. Figure A shows the sinusoidal forcing signal applied to the tenth oscillator. Figure B shows the relative phases of several oscillators with sinusoidal forcing for $m = 10$ where $f - f_0 = 0.0005$ and Figure D shows the relative phases for oscillators 3 through 7 when $m = 5$ . Figure C plots the frequency for oscillators 9 and 10 during the entire bending signal. Figure E illustrates the noisy sinusoidal forcing signal applied to the $m$ th oscillator. Figure F shows the relative phases of oscillators 4, 8, 9, and 10 with $f - f_0 = 0.0005$ , forcing strength $\alpha_f = 3$ and noise level $\sigma = 0.15$ . Figure G plots the frequency for oscillators 9 and 10 throughout the entire bending signal for $m = 10$ . Note that the noise is clearly visible in oscillator 10, where forcing is applied, but the amplitude of the noise is dramatically decreased in oscillator 9. Figure H plots the relative phases of oscillators 3 through 7 when $m = 5$ . . . . .	58

3.4	Experimental and computational results indicate that the CPG is highly robust to noise. Figure A shows a sample recording showing entrainment of the CPG activity (black) to a noisy bending signal (blue) with SNR of 10. Figures B and C show the experimental (B) and computational (C) entrainment results for signals with a range of SNR values. $R$ is the resultant vector length; $R > 0.8$ indicates entrainment. . . . .	61
4.1	Normalized ramp bending and raw edge cell recording. Note there are different units that respond during different portions of bending. Large spikes occur during active periods of bending and smaller spikes occur during hold times with positive bending angle. . . . .	70
4.2	Example of DataView spike sorting. A) All spike waveforms for a single unit are shown in gray. The red line denotes the average waveform over all the spikes classified into that unit. B) Clusters used to identify separate units within the recording. Different colors represent different types of units with similar spike shapes. The three dimensions of the plot represent three of the principal components used to determine different types of spikes based on features of their waveform. . . . .	72
4.3	For preliminary analysis, the ramps were broken up into six phases where spike rate was computed. This figure illustrates the three different phases: the swing outwards, the hold, and the return swing. Note that ramps can be applied to both sides of the body so in total there are 6 distinct phases to compare. . . . .	72
4.4	Examples of units with significant spike rates for the six phases of ramp bending. Each data point represents a spike rate for a single ramp. The trend line was found using linear regression. Figure 4.4(a) shows spike rate as a function of bending angle for spikes that occurred while the spinal cord was held to one side. Figures 4.4(b) and (c) show spike rate as a function of bending velocity for ramps to the right and left side of the body respectively.	75
4.5	Significant responses for each unit. Gray blocks indicate the units that had no significant responses to bending. Black blocks indicate the unit has a significant average spike rate for that particular phase. Blue blocks indicate that the unit had a significant average spike rate and a trend line with significant slope. A count of both types of significant responses for each ramp phase is shown in the histogram on the right. . . . .	76
4.6	Rate of adaptation. Figure 4.6(a) shows the ramp bending signal and a raster of spike times for a fast adapting unit. Spikes only occur at the beginning of the phase. Figure 4.6(b) shows the ramp bending signal and a raster of spike times for a slowly adapting unit. Spike occur at approximately the same rate for the entire phase. . . . .	77
4.7	Example of a single fit of firing rate as a function of duration of static bending. Firing rates for a unit with significant bending angle response plotted by red circles. Firing rate fit to an exponential curve of the form $a_1 e^{-b_1 t}$ with $a_1 = 327.6$ , and $b_1 = 136.4$ . . . . .	78

4.8	Distribution of fitted parameters for 3 types of units with significant position response, significant velocity response, or significant response to both. Firing rate as a function of duration of static bending is fit to $a_1 e^{-b_1 t}$ . Only significant fits ( $R^2 > 0.5$ ) were included. On average position responders have the slowest adaptation and units that respond to both position and velocity have the fastest adaptation. . . . .	79
5.1	Schematic of LTI system with input $u(t)$ and output $x(t)$ . . . . .	83
5.2	Bode plot for the LTI system given by $\dot{x}(t) = -x(t) + u(t)$ . The gain of the FRF shows that the output will have a smaller amplitude than the input for all frequencies and for large frequencies the output will be almost negligible. The phase of the FRF shows that as the input frequency increases the phase difference between the input and the output approaches $90^\circ$ . . . . .	85
5.3	Example of the input and output for the LTI system given by $\dot{x}(t) = -x(t) + u(t)$ for input $u(t) = \sin(2\pi t)$ . Note the output has the same frequency as the input. The output $y(t)$ has amplitude around 0.15 and is ahead of the input signal by approximately $80^\circ$ which is what is predicted by the Bode plot in Figure 5.2. . . . .	86
5.4	Comparison of window weights. a) Rectangular window weights used for computing the power spectral density. All points are weighted evenly. b) Hanning window weights used for computing the power spectral density. Points towards the middle of the window are weighted more than points on either end. c) Fourier transform of window weights for a 20 second long signal sampled at 100 Hz with spectral window length 1 second. The Fourier transform of the rectangular window is plotted in blue and the coefficients are nontrivial for larger frequencies. These are called side-lobes. The Fourier transform of the Hanning window is plotted in red and the coefficients approach zero much faster. Thus, the Hanning windows give a more accurate approximation of the power in the signal. . . . .	88
5.5	Example of a random signal split into three Hanning windows of length 20 seconds with 50% (10 seconds) overlap between windows. . . . .	90
5.6	Approximation of PSD of known analytic FRF given by $H(s) = 2\pi/(s^2 + \pi s + 4\pi^2)$ . The true PSD is shown in the black dashed line. PSD for rectangular windows with no overlap is plotted in blue. PSD for Hanning windows with 50% overlap plotted in red. Splitting the signal into Hanning windows with 50% overlap gives a better approximation to the true PSD than rectangular windows with no overlap. . . . .	91
5.7	Normalized noisy bending signal (red) and experimental edge cell recording (blue). . . . .	93
5.8	Bode plot for edge cell response data and best fit with model transfer function $H_a(s) = (a_1 s + a_0)/(b_2 s^2 + b_1 s + 1)e^{-\tau s}$ . Analytic transfer function fit to experimental FRF for edge cell response. Parameter values are $a_1 = -0.0012\text{Vs/deg}$ , $a_0 = 0.0015\text{V/deg}$ , $b_2 = 2.7 \times 10^{-7}\text{s}^2$ , $b_1 = -193.8\text{s}$ , and $\tau = 0.029\text{s}$ . . . . .	95

5.9	Sinusoidal bending and edge cell recordings. a) Normalized sinusoidal bending signal at 1 Hz and the normalized edge cell response recorded from the left lateral tract. b) Normalized noisy sinusoidal bending at 1 Hz and the normalized edge cell recording from the left lateral tract. Note in both recordings the edge cell response occurs towards the peak in bending to the right. . . . .	99
5.10	a) Recording from left lateral tract in response to noisy sinusoidal bending. b) Output signal used for FRF computation. Spike times found when edge cell recording crossed threshold of 0.4 mV. Spike times then convolved with normalized Gaussians of width 15 ms. Note the larger peaks in the output signal arise from two spikes that occur close together. . . . .	100
5.11	Experimental phase-dependent IRF from bending to edge cell activity. a) Normalized mean bending signal and edge cell activity signal. Note bending to the right is positive. b) Phase-dependent IRF from bending to edge cell activity. We only see response to perturbations applied during phases where edge cells are normally active, between phases 0 and 0.25. We see an increase in edge cell activity (red) followed by a decrease in activity (blue). . . . .	101
5.12	Impulse response for $\ddot{y} + a\dot{y} + ky = b(t)u(t - \tau)$ with $a = 40$ , $k = 4000$ , $b(t) = -30((1 + \cos(2\pi t - \pi/4))/2)^{16}$ , and $\tau = 0.15$ . . . . .	103

## List of Abbreviations

CPG	central pattern generator
EC	edge cell
LTI	linear time invariant
LTP	linear time periodic
FRF	frequency response function
IRF	impulse response function

## Chapter 1: **Introduction**

In vertebrates, the neural activity for rhythmic movements like walking and swimming is generated by a group of neurons in the spinal cord which make up a central pattern generator (CPG) [11]. CPGs have been found in both legged and non-legged vertebrates (see for example [75, 19, 68, 3]) but for legged locomotion less is known about the internal structure of the CPG. It has been shown that CPGs are capable of producing periodic neural activity without sensory input or descending control from the brain [19, 68, 3]. The study of the primitive vertebrate CPG is a first step to understanding the central nervous system and its role in locomotion.

CPGs have been found in almost every animal studied including those that walk [5, 35, 56], fly [75] or swim [11, 19, 52, 60, 71]. We focus on swimming and study lamprey locomotion. Lampreys have long been model organisms for vertebrate locomotion because they are primitive vertebrates with the same classes of neurons found in higher vertebrates, but orders of magnitude fewer neurons. Lamprey swimming consists of a simple undulation which produces a sine curve shape along the body and propels the animal forward [10]. The lamprey CPG consists of repeated subunits, each of which are oscillatory, and these units maintain a constant phase offset in order to produce a traveling wave of neural activity. This wave of neural activity travels from head to tail with a phase lag of 1% per cycle between adjacent segments [19, 70]. In the lamprey, several classes of neurons within the CPG have been identified based on morphology, size, and physiological properties (see [64]

for review of lamprey CPG). In other vertebrate models, such as zebrafish and mice, the organization of these neurons is not yet known. Additionally, the excised spinal cord can be preserved in a physiological saline for up to a week [63]. Moreover, neural activity in the excised spinal cord can be generated by excitatory neurotransmitters and the activity recorded from the ventral roots *in vitro* shows the same temporal characteristics as muscles in the intact swimming lamprey [11].

Rhythmic movements are driven by the CPG but locomotion is a complex system of interactions between sensory information, neural activity, and body kinematics. A perturbation or sudden change in the environment can cause a change in the body, which then activates mechanosensitive neurons. These sensory neurons send information to the central pattern generator (CPG). A CPG is a neural circuit that produces neural activity for locomotion and this activity can be altered by sensory information [20]. Thus, the sensory information from a perturbation will activate the neurons within the CPG which then send signals to muscles to produce movement. Although these systems are interconnected, in principle it is hard to study swimming in a complete, closed-loop system. As an alternative, open-loop experiments are used to investigate the properties of subsystems within the locomotion loop [61, 13]. This approach has been used to study blowflies [15] and electric fish [14, 45]. Studying the complex systems involved in locomotion requires an interdisciplinary approach which combines experiments and mathematical modeling. We now review the relevant contributions from lamprey experimental preparations and mathematical models of CPGs.

## 1.1 Properties of the Lamprey CPG

To investigate the properties of the lamprey CPG, biologists remove the spinal cord along with the notochord, a flexible rod under the spinal cord similar to cartilage, from the body and innervate the CPG with a bath of excitatory neurotransmitter, D-glutamate. Glass suction electrodes are placed along the side of the notochord and record activity from the ventral roots. A schematic of the lamprey spinal cord and the position of the ventral roots is shown in Figure 1.1. The electrodes record activity produced by the CPG which would innervate muscles for swimming in intact lamprey. From these recordings it has been shown that the duration of the ventral root bursting activity is proportional to the period of the cycle of activity (about 40%) [10]. Additionally, the activity from two ventral roots (left and right) in a single segment strictly alternates and the ventral root activity in two adjacent segments has a phase lag proportional to the period [10]. These phase lags account for the traveling wave of activity which activates muscles for undulatory swimming. The ventral root recordings for a CPG activated with neurotransmitters are referred to as “fictive swimming” because the neural activity is very similar to that seen in swimming fish [10]. Additionally, in the presence of a rhythmic stimulus the CPG tends to adjust the frequency of its output to match the stimulus frequency. This phenomena is known as entrainment. The ability of the CPG to adjust its frequency along the entire length of the spinal cord in response to a local stimulus indicates that the segments that comprise the CPG are interconnected. Anatomical investigation reveals there are several different tracts of fibers in the spinal cord [10]. The location of these tracts is illustrated in Figure 1.1. Note these regions are repeated across the midline so each half of the spinal cord is often referred to as a hemisegment. Lesions applied to different tracts

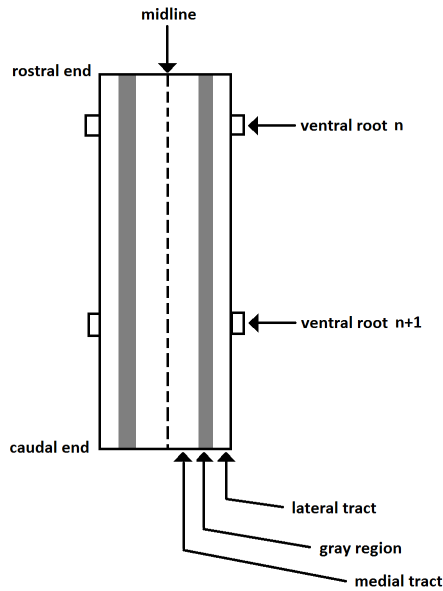


Figure 1.1: Schematic of the different tracts seen in the excised lamprey spinal cord. Note ventral roots occur periodically on the left and right sides of the notochord right under the spinal cord.

within the spinal cord are used to investigate the properties of intersegmental coupling and determine mechanisms by which the neural activity remains coordinated along the length of the cord. Cohen et al. [10] described the effects of different sized transverse lesions in various locations along the spinal cord. Recordings made above and below the lesion site were compared and often little change was seen until the lesions extended across the midline. Recordings suggest that there are many fibers in each tract that contribute to intersegmental coordination but the strength and direction of these fibers differ in the different regions [10]. Since it is quite difficult to measure the connection strengths between different pairs of segments along the spinal cord, we use mathematical models of the CPG to test various types of intersegmental coupling.

## 1.2 Mathematical Models of CPGs

While experiments have identified many aspects of the lamprey CPG, much is still unknown about the exact connections within each segment and between segments along the spinal cord. Experimentalists have hypothesized that there exists asymmetry in ascending and descending coupling due to experimental recordings with legions along the spinal cord. However, it is not known the exact length and strength of these connections. Thus, mathematical modeling is needed to inform what types of intersegmental coupling properties can produce stable solutions with the desired biological properties seen in the experimental CPG recordings.

One of the first models of the lamprey locomotor CPG was studied by Cohen et al. [10] before the internal structure of CPG segments had been investigated. Thus, the first step in modeling was to assume that a chain of coupled oscillatory units could produce a periodic output similar to the rhythmic output of the CPG. Since the individual neural make-up of each segment was not known, Cohen et al. [10] modeled each segment with a single variable  $\theta$  which represented the phase of the oscillation. This seminal work made two assumptions about the properties of oscillators in the chain: 1) a single oscillator is associated with each segment of the spinal cord, 2) each oscillator is coupled to its immediate neighbors and possibly to distant oscillators. Using these simplified models, Cohen et al. [10] analytically studied possible mechanisms in a chain of coupled oscillators which could produce a constant phase lag between oscillators as seen in experimental recordings from the lamprey CPG. In the phase model each segment  $i = 1, \dots, n$  is represented by  $\dot{\theta}_i = \omega_i + \sum_{j=1}^n \alpha_{ij} h(\theta_j - \theta_i)$ , where  $\omega_i = 2\pi/T_i$  is the uncoupled frequency of each oscillator. The oscillators are connected to one another through  $h$ , which is a bounded periodic

function. With the simple choice  $h(\theta) = \sin(\theta)$ , the phase model captures many experimental observations and indeed the slowly varying intracellular potentials of motoneurons are quasi-sinusoidal [11]. Uni-directional nearest neighbor coupling, bi-directional nearest neighbor coupling, and nearest neighbor with long distance coupling were used to connect the chain of oscillators. All models considered were able to produce a stable traveling wave with bi-directional coupling as long as oscillators are tuned [10]. Tuning oscillators here means that the intrinsic frequencies of the oscillators are graded so that the rostral oscillators have larger frequencies than the caudal oscillators. This produces a forward traveling wave of activity. If the oscillators are identical, ie.  $\omega_i = \Omega$  for all  $i$ , then the oscillators are in synchrony and there is no traveling wave solution. Thus, for coupled oscillators there must be a difference in the intrinsic frequency of each oscillator in order to get a traveling wave as seen in experimental recordings. However, solutions with constant phase lags do not correspond to constant speed wave solutions which are seen during steady state swimming [10]. Thus, the lamprey CPG must use a different mechanism to produce traveling waves of neural activity.

The seminal work of Cohen et al. [10] was followed by the work of Kopell and Ermentrout [38, 39, 41] who also studied chains of coupled oscillators, but with a more general coupling function  $H(\theta_i - \theta_{i+1})$ . Kopell and Ermentrout studied conditions on coupling that would produce stable phase lags between oscillators and also investigated possible mechanisms for adjusting the frequency of each oscillator in the chain [38, 39]. For chains of weakly coupled chains of oscillators with nearest neighbor coupling, with unspecified coupling functions  $H$ , it was shown that coupling symmetry affects the qualitative form of phase locked solutions (ie. solutions with constant phase lags between oscillators) [38]. Further phase lags are determined by the intrinsic frequency of each oscillator and

coupling strength. If the coupling function is such that  $H(0) \neq 0$ , which implies that oscillators at the same phase still influence one another, then identical oscillators with equal coupling can have nonzero phase lags [39]. Moreover, the phase lags produced are almost constant, except for a boundary layer, which corresponds to a constant wave speed. Note this was not seen in the case where frequency gradients produced uniform phase lags [10]. Kopell and Ermentrout also showed mathematically that the chain of oscillators must have uniform intrinsic frequencies and coupling strengths to achieve uniform phase lags [39]. They also conjectured that long-distance coupling may be responsible for adjusting phase lags along with input from sensory feedback [39]. These results are shown analytically, with unspecified coupling functions  $H$ , which are assumed to have certain properties but do not have a closed form. Both analytically and numerically, that there is a large class of coupling functions that will produce solutions with stable, nonzero phase coupling between the oscillators. In summary, the results of Kopell and Ermentrout show that a chain of coupled oscillators with uniform intrinsic frequencies and long distance, asymmetrical coupling produces a traveling wave of activity with uniform phase lags. Guan et al. [25] estimated the total intersegmental coupling strengths from experiments where the spinal cord was bent at one end. To determine the ascending and descending coupling strengths, a stochastic two oscillator model was fit to the burst frequencies of the rostral and caudal parts of the spinal cord [36]. In all preparations, ascending coupling (towards the head) was stronger than descending coupling [25]. This evidence, along with the phase model analysis of Kopell and Ermentrout [17, 38, 39, 41] support the use of coupling asymmetry in lamprey CPG models.

As more was discovered about the neurons within the lamprey CPG, more detailed biological models were developed to capture the known properties of the CPG output

signal. Experimentally several classes of neurons in the lamprey CPG have been identified that make up the CPG circuit (see [64] for a review of the neuronal components of the lamprey CPG). Models based on cellular properties (Hodgkin-Huxley type models) have been used to simulate the oscillatory potentials recorded from lamprey CPG neurons. Wallen et al. [69] simulated a neural network where individual neurons were modeled with various physiological properties. Neurons were modeled to include the specific membrane and synaptic connection properties [69]. Buchanan and Grillner [9] proposed a model for the CPG based on the synaptic connection of three, then newly discovered, interneurons in the lamprey spinal cord. Each unit oscillator consisted of excitatory neurons, crossed inhibitory neurons, and lateral inhibitory neurons. Buchanan [8] investigated different intersegmental coupling schemes by connecting different pairs of cells in two coupled oscillators with the neural structure from [9]. All combinations could produce a phase-locked solution between the two oscillators for a certain range of synaptic connection strengths. Similarly, Williams [72] studied several connectionist neural models where each segmental oscillator consisted of two sets of interconnected neurons. Each unit oscillator consisted of two sets of E, L and C neurons connected as in [9, 8]. She hypothesized that intrasegmental connections between cells are repeated between adjacent segments but with reduced strength. With asymmetrical coupling (differences in rostral and caudal connection strengths) traveling waves of neural activity are produced. This hypothesis is supported by experimental recordings where lesions are applied to various locations along the spinal cord. Varkonyi et al. [67] used phase reduction and averaging to compute intersegmental coupling functions for a network-based and a cell-based model of the lamprey CPG. The coupling functions they derive are qualitatively similar to sinusoidal coupling functions but differ in behavior as swimming frequency varies. Additionally, in the network-based

model ascending and descending coupling strengths can be tuned to achieve approximately constant phase lags between segments over a range of frequencies while the phase lags in the cell-based model are less robust [67]. The addition of long distance coupling increases the stability of the phase lags. Thus, when investigating the addition of sensory feedback we use the network-based model first proposed by Buchanan [8] and Williams [72] with long distance coupling as a starting point.

### 1.3 Sensory Feedback and Entrainment

Entrainment is the ability of the CPG to adjust the frequency of its output to match the frequency of a bending stimulus when the bending frequency is close to the natural frequency of the CPG output [19]. Previously entrainment results showed a different phase relationship between the bending signal and CPG activity for entrainment during rostral versus caudal bending [65]. Bending experiments have shown entrainment via mechanosensory feedback occurs locally at the point of bending and intersegmental coupling is responsible for the entrainment of the rest of the spinal cord [48]. The fact that the spinal cord can be entrained by both rostral and caudal bending provides evidence for the existence of ascending and descending connections [48]. To further examine the phase relationship between bending and CPG output, Tytell and Cohen [66] experimentally measured entrainment ranges as a function of bending position. In addition to bending the rostral and caudal ends of the spinal cord, they bent the spinal cord at various segments between the two ends. Tytell and Cohen [66] found that entrainment ranges are largest when bending is applied near the middle of the spinal cord. They gave two hypotheses for the differences in entrainment for rostral and caudal bending: 1) the ascending and descending connections are asymmetric, either as a result of dissection or

biological structure or 2) some aspect of the CPG or edge cells varies along the length of the spinal cord. In the first case, any excised piece of spinal cord should show a gradient in entrainment range for any length section of spinal cord because segments at the rostral end will receive more ascending input and segments at the caudal end will receive more descending inputs. In the second case, different sections of spinal cord (rostral or caudal) should entrain to different phases of bending no matter what length of segment is dissected. To distinguish between these two mechanisms, Tytell and Cohen [66] studied progressively shorter segments of the spinal cord and compared the resulting burst phases of the CPG relative to the bending signal. This data revealed that shorter sections of spinal cord entrained with the same burst phases, supporting the second hypothesis that the rostral and caudal ends of the spinal cord differ intrinsically. Entrainment ranges as a function of bending location revealed that the middle of the segment is easier to entrain than either end [66]. These results indicate an asymmetry between the rostral and caudal ends of the spinal cord but do not indicate what that difference is. Thus, mathematical modeling is needed to further test possible coupling asymmetries along the spinal cord.

The CPG can produce rhythmic output without sensory feedback or descending control from the brain, however sensory information, especially proprioception influences the signal. It is known that sensory feedback and entrainment are important for responding to perturbations during swimming [51]. Guan et al. [25] also showed the importance of sensory feedback in maintaining the correct phase relationship between muscle activation and the body kinematics during swimming. To study the effects of feedback, Guan et al. [25] performed bending experiments on two lamprey spinal cord preparations, one with muscles intact and one without muscles. Electrophysiological recordings during fictive swimming showed that preparations with muscle had higher frequency CPG output and

shorter phase lags between neural activity in different segments. Additionally, preparations with two staggered hemisections were used to measure differences in coupling strengths. During fictive swimming, the spinal cord with two hemisections showed that ascending coupling was stronger than descending [25]. Coupling strengths were also larger when muscle was left intact, indicating that movement and movement related feedback affects the coupling between segments. Again bending experiments show a difference in ascending and descending coupling in the lamprey CPG, but still do not measure the exact connection lengths and strengths between anatomical segments.

#### 1.4 Forced Chains of Coupled Oscillators

Forcing or bending the spinal cord experimentally activates sensory feedback which is known to help adjust the frequency and phase relationships within the CPG output. As described earlier, bending experiments have been performed and entrainment ranges computed for excised spinal cord sections. Forced chains of coupled oscillators are used to model these bending experiments. We assume that forcing occurs at only one oscillator in the chain and that forcing is sinusoidal with some forcing frequency  $\omega_f$ . An advantage of studying a mathematical model of the CPG is that we can compare the entrainment results for different choices of intersegmental coupling. We now review how modeling these experiments can inform how segments of the lamprey CPG are connected along the length of the spinal cord.

To force a chain of coupled oscillators, we introduce an additional variable to represent the phase of forcing, namely  $\theta_f$ . The forcing signal represents the bending of the spinal cord in the experimental set-up. Typically,  $\theta_f$  is defined to be the solution of  $\dot{\theta}_f = \omega_f$  where  $\omega_f$  denotes the angular frequency of the forcing signal. Williams [73] predicted from

lesion experiments that ascending coupling is more important than descending for setting the phase difference between oscillators and descending coupling plays a role in changing the frequency of the oscillators. She tested this hypothesis on a phase model with generic coupling functions  $H^+$  (ascending) and  $H^-$  (descending) and applied forcing to both the rostral and caudal ends of the chain. Both model analysis and experimental data showed that there are a range of frequencies that can entrain the CPG [73]. However, at one end the frequencies in the entrainment range are above and below rest but at the other end they will only be above. Mathematical analysis of the model indicates that ascending connections control the phase lag and descending connections adjust the frequency of oscillations. It also suggests that there are differences in ascending and descending coupling other than strength [73]. Thus, phase models can inform us of the importance of coupling strength and coupling asymmetry but do not provide insight into the biology of the connection types within the CPG. Kopell and Ermentrout suggested that since forcing the chain of oscillators from the rostral and caudal ends has different effects on phase lags [48], there is an asymmetry in ascending and descending coupling. Kopell et al. [40] expanded on the forcing simulations in [73] and showed entrainment ranges depended on how the oscillators are coupled, the length of the chain, and which end receives the forcing. When ascending coupling was stronger than descending and forcing at the rostral end, entrainment only occurred for frequencies above the unforced frequency of the chain [40].

To further test the possible coupling schematics for chains of coupled phase oscillators, Previte et al. investigated the qualitative properties of entrainment ranges [57]. Motivated by experimental entrainment ranges of Tytell and Cohen [66], they considered several types of coupling and computed the resulting entrainment range for each model.

The basic model is described by

$$\dot{\theta}_i = \omega_0 + \sum_{j=1}^n \alpha_{i-j} \sin(\theta_j - \theta_i - \psi_{i-j}) \quad i \neq m \quad (1.1)$$

$$\dot{\theta}_m = \omega_0 + \sum_{j=1}^n \alpha_{m-j} \sin(\theta_j - \theta_m - \psi_{m-j}) + \alpha_f \sin(\theta_f - \theta_m) \quad (1.2)$$

$$\dot{\theta}_f = \omega_f \quad (1.3)$$

where  $\theta_i$  represents the absolute phase mod  $2\pi$  of the  $i$ th segment in the chain. Each segment, uncoupled, has a periodic orbit with frequency  $\omega_0$ . However, each segment in the chain is connected to other segments, which alters the frequency of each oscillator. Previtte et al. considered two types of coupling within the chain: nearest neighbor and all to all. For nearest neighbor coupling, each segment is only connected to adjacent segments. In all to all coupling, each segment is connected to every other segment within the chain. The summation term in (1.1) represents the intersegmental connections in the chain. Oscillators are coupled through sine functions which depend on phase differences between oscillators. To create the oscillatory rhythm produced by the CPG for swimming, there must be a phase lag between segments. This has been measured experimentally as approximately 1% of the cycle per segment [19, 70]. This lag is prescribed in (1.1) by  $\psi_{i-j}$  and is set to  $(i - j)2\pi(0.01)$ . The strength of the connection between oscillator  $i$  and  $j$  is denoted by  $\alpha_{i-j}$  and only depends on the relative distance between the two oscillators. That is, the strength of the connections depends on  $k = i - j$  where positive values of  $k$  denote ascending connections (connections from the tail/caudal end towards the head/rostral end) and negative values of  $k$  denote descending connections (connections from the head/rostral end towards the tail/caudal end). If the connection strengths  $\alpha_{i-j}$  are chosen correctly, we can assume without loss of generality that the preferred phase  $\psi_{i-j} = 0$  for all oscillators and still maintain the desired phase lag.

To model the bending experiments of Tytell and Cohen, Previte et al.[57] add a forcing connection to the phase model which represents the affects of bending at a single point along the spinal cord. Bending is assumed to activate mechanoreceptors on only one segment in the chain, which is denoted by  $m$ . This input is represented in (1.2) by the term  $\alpha_f \sin(\theta_f - \theta_m)$  where  $\alpha_f$  denotes the strength of the forcing and  $\theta_f$  represents the phase of the forcer. The forcer obeys the differential equation  $\dot{\theta}_f = \omega_f$  where  $\omega_f$  is the forcing frequency, representative of the bending frequency in the bending experiments. Experimental evidence supports the hypothesis that coupling in the lamprey CPG is asymmetric. Thus, Previte et al. [57] compare two types of coupling asymmetry: uniform and nonuniform. Uniform coupling asymmetry means that  $\alpha_k > \alpha_{-k}$  for all connection lengths  $k$ . Thus, ascending coupling is stronger than descending coupling for all connection lengths. Nonuniform coupling asymmetry means that for some connection lengths ascending strengths are greater than descending strengths but for other connection lengths the opposite is true. Entrainment ranges as a function of forcing position were computed for all-to-all coupling with both types of coupling asymmetry. For uniform coupling asymmetry, entrainment ranges monotonically increased as the forcing position moved towards the end of the chain of oscillators [57]. For nonuniform coupling asymmetry, entrainment ranges were non-monotonic as a function of forcing position and the largest entrainment range occurred for forcing near the middle of chain [57]. This supports the experimental evidence for coupling asymmetry because experimental entrainment ranges are non-monotonic [66].

## 1.5 Edge Cells

It has been shown experimentally that sensory feedback is essential to entrainment. Mechanosensory intraspinal neurons were discovered in the lateral tracts of the lamprey spinal cord [21]. These neurons are commonly referred to as edge cells. Through bending experiments with an inactive CPG, it was shown that these mechanosensory neurons respond to stretch and rate of stretch of the spinal cord [23, 58]. Further, it was shown that edge cells can affect the CPG through excitatory and inhibitory connections [58]. These effects represent two classes of edge cells: edge cells with contralateral projections and edge cells with ipsilateral projections. Edge cells with contralateral projections inhibit groups of CPG neurons on the opposite side of the body. Edge cells with ipsilateral projections excite groups of CPG neurons on the same side of the body [58]. It is not known the exact direction or length of these projections or exactly how edge cells affect the CPG rhythm but bending experiments similar to CPG bending experiments have been used to characterize the response of the stretch receptive neurons.

It has been shown that entrainment ranges vary based on the location of bending along the spinal cord [48, 73, 66]. Hsu et al. [33] hypothesized that since sensory information aid in entrainment the differences in entrainment ranges imply sensory response should also differ along the spinal cord. To investigate the response properties of lamprey stretch receptive neurons they performed bending experiments where the excised lamprey spinal cord was bent in the horizontal plane (yaw) and in the sagittal plane (pitch). Their bending signals consisted of bending and holding to one side of the body then bending towards the opposite side and holding. For the intact spinal cord, recordings from the right lateral tract showed responses to both bending to the left and right in the

horizontal plane. This implies that responses from both ipsi- and contralaterally projecting edge cells were recorded. However, the majority of stretch receptive neurons responded to ventral and contralateral bending [33]. They were able to record responses up to 15 segments away from the bending site, which gives an approximate length for edge cell axons. Along with calcium free recordings of stretch receptive neurons, Hsu et al. [33] also recorded motor neuron activity from the dorsal and ventral branches of the ventral roots and characterized how the response depended on the location and direction of bending. A larger proportion of motor neurons responded to bending in the yaw direction than in the pitch direction while the opposite is true for sensory neurons [33]. They hypothesize that ventral bending activates both classes of edge cells which then inhibit one another through crossed inhibitory connections, which is supported by experiments with split spinal cords [33]. For yaw bending, sensory neurons are activated in anti-phase so there is a larger affect on motorneuron activity.

## 1.6 Outline of Work

Our goal is to understand and model the role of sensory feedback for entrainment in the lamprey CPG. We first expanded upon the work of Previte et al. [57] and modeled the open loop bending experiments of Tytell and Cohen [66] with two models: the neural model with sensory feedback and the derived phase model. The neural model we used is an extension of the model studied by Buchanan [8] and Williams [72] and we included connections from edge cells to represent the effects of bending. The derived phase model is a linearization of the neural model around a periodic orbit. We assume the neural model has weak intersegmental coupling and exploit the theory of weakly coupled oscillators [55, 67] to reduce the neural model to a phase model. To compare these models to the

experimental results of Tytell and Cohen [66], we computed entrainment ranges using continuation methods. We varied intersegmental coupling strengths and compare the resulting entrainment ranges. This is an instance where modeling can inform the biology since it is difficult to measure connection strengths within the lamprey spinal cord.

To further understand how the lamprey CPG responds to sensory information, namely mechanosensory information from edge cells, we added a noisy signal to the usual sinusoidal forcing signal. The additive noise can represent perturbations that might occur during swimming like currents, rocks, or other lamprey swimming nearby. We perform noisy bending both experimentally and in our derived phase model. To characterize noisy entrainment we quantified the variability in each oscillator and if the signal is mostly phase-locked with the underlying sinusoidal bending frequency we call the CPG entrained. We compare the entrainment results from noisy bending to the entrainment results from deterministic sinusoidal bending. This is a first step in understanding how the CPG responds to perturbations and interprets variable input from sensory neurons. In the experiments we see that the CPG still entrains to the bending frequency for large levels of noise. The variability in the sensory feedback is greatly reduced in the sense that the CPG bursts still burst at approximately the same phases. The derived phase model responds similarly to the addition of noise and the variability filters out in the adjacent oscillators.

We also investigated the encoding properties of edge cells. It is known that the edge cells respond to stretch and rate of stretch [22, 33], but it is not known how this information is encoded and sent to the CPG. We performed extracellular recordings from the lateral axon tracts in the excised lamprey spinal cord and analyze the edge cell response to various bending stimuli. First we bent the spinal cord with varying bending angles and bending velocities to determine the relationship between edge cell firing rate and

bending. For most units, we found a significant linear relationship between spike rate and bending angle or spike rate and bending velocity. We also found several units that fired constantly in response to bending, that is the spike rate remained constant as bending velocity increased. Next, we applied sinusoidal bending to the spinal cord and saw that edge cells fire consistently during one phase of bending. The phase of firing depends on the amplitude and frequency of the bending signal. To completely characterize the edge cell response across a range of frequencies, we added band-limited Gaussian white noise to the sinusoidal bending signal. The additive noise allows us to use frequency domain techniques to predict the response of the system to perturbations [34]. The map from input to output in the frequency domain is called a harmonic transfer function (HTF), which is the periodic extension of a frequency response function (FRF). The time domain analogue of the HTF is called a phase-dependent impulse response function (IRF). The phase-dependent IRF tells us how the system responds to brief pulse perturbation at a given phase. These tools give us a non-parametric map from bending to edge cell output. We then matched the response characteristics of the IRF to model IRFs to determine an appropriate model of edge cell response. This model can then be added to closed-loop swimming models as feedback from edge cells to the CPG.

## Chapter 2: CPG Models and Entrainment

### 2.1 Overview

Previous work focused on modeling experimental entrainment of the lamprey CPG in a phase model. Experimental entrainment provides evidence of intersegmental coupling between segments in the spinal cord because the influence of bending at one end of the spinal cord is transmitted throughout the cord. Intersegmental strengths are hard to measure directly and hence entrainment provides a means to indirectly study intersegmental connections. Motivated by the experimental entrainment ranges of Tytell and Cohen [66] and the analytic entrainment results of Previte et al [57], we compute entrainment ranges for two CPG models. We first add sensory feedback to the neural model developed by Buchanan [8] and Williams [72]. Next we derive a phase model by linearizing the neural model around a periodic orbit using methods described by Varkonyi et al [67]. In the limit of weak coupling, the derived phase model provides a good approximation of the neural model. For both models, we compute entrainment ranges as a function of forcing strength and forcing position for two types of intersegmental coupling. Non-uniform coupling asymmetry (coupling where some connection strengths are stronger in the ascending direction and other coupling strengths are stronger in the descending direction) yields non-monotonic entrainment ranges as a function of forcing position, which more qualitatively mimics the experimental results of Tytell and Cohen [66]. Furthermore, the derived

phase model captures the way entrainment is lost in the neural model. This is something that cannot be seen in the sinusoidal phase model analyzed by Previtte et al. [57]. This supports the use of the derived phase model to extend the analysis of [57] and examine a wider range of coupling and forcing functions. Entrainment ranges of both the neural and derived phase models support the hypothesis that nonuniform coupling asymmetry exists in the lamprey CPG.

## 2.2 Neural Model

Biologists have discovered several classes of neurons within the lamprey CPG and these neurons together produce the rhythmic neural activity for swimming (see [64] for a review of the neuronal components of the lamprey CPG). CPG models based on several of these classes of neurons have been studied by Buchanan [8] and Williams [72]. In their model, each segment is represented with a number of variables proportional to the number of classes of neurons. Buchanan [8] and Williams [72] consider three classes of neurons: excitatory interneurons (E), crossed inhibitory interneurons (C), and lateral inhibitory interneurons (L). These neurons are connected to one another within a segment and Figure 2.1 depicts these intrasegmental connections. Note that in each segment the connections exhibit left-right symmetry, that is, the connections on one side of the segment are repeated on the other. This yields a total of 12 connections, two sets of 6, within a single segment. Along with the three classes of interneurons within a spinal cord segment, there are two edge cells (left and right) located in the lateral tract of the spinal cord. These interneurons are mechanoreceptors that detect bending of the body during swimming. Edge cells have been recorded and found to respond to stretch and rate of stretch of the body [23, 58]. A fluorescent stain is used to identify the morphology of these edge cells and an

example of one such image is shown in Figure 2.2. Edge cells, activated by stretch caused by the bending of the spinal cord, act as sensory feedback for the CPG. We incorporate this sensory information into the existing neural models [7, 72]. It is known that two classes of edge cells exists: edge cells that excite ipsilaterally and edge cells that inhibit contralaterally. In our model we include a single edge cell on either side of the segment with two ipsilateral connections and two contralateral connections. These connections are illustrated in Figure 2.1. The resulting neural model is given by

$$\dot{v}_{ij} = -G_R v_{ij} + G_T^j (1 - v_{ij}) + \sum_{k=1}^n \sum_{l=1}^6 \alpha_{i-k}^{lj} G_0^{lj} \bar{h}(v_{kl}) (V_{\text{syn}}^l - v_{ij}) \quad (2.1a)$$

$$+ \delta_{im} \alpha_f \sum_{s=1}^2 G_f^{sj} \bar{h}(v_{\text{ec}}^s(\theta_f)) (V_{\text{syn,ec}}^{sj} - v_{ij}) \quad \text{for } i = 1, \dots, n; j = 1, \dots, 6,$$

$$\dot{\theta}_f = \omega_f \quad (2.1b)$$

where

$$\bar{h}(x) = \sigma \log \left( 1 + e^{\frac{x}{\sigma}} \right) \quad (2.1c)$$

is a smooth threshold function and

$$v_{\text{ec}}^s(\theta_f) = (-1)^s \sin(2\pi\theta_f) \quad (2.1d)$$

is edge cell voltage with  $s$  denoting the left or the right side as illustrated in Figure 2.1. Unlike phase models in which each segment corresponds to one variable, the phase, each segment is now represented by 6 variables which represent the three classes of neurons on either side of the segment. Our state variables  $v_{ij}$  denote the “voltage” of cell  $j$  in segment  $i$ . Note that voltage is scaled to be unitless and lie between -1 and 1. When  $v_{ij} < 0$  the cell does not fire action potentials and  $v_{ij}$  represents the membrane voltage of the cell body. When  $v_{ij} > 0$  the cell fires action potentials and  $v_{ij}$  can be thought of as the normalized firing rate. Note  $j$  ranges from 1 to 6 and the cell indices are labeled

in Figure 2.1. The constants  $G_R$  and  $G_T$  denote the resting and tonic drives that drive the voltage towards 0 and 1 respectively. The double summation from in (2.1) denotes the intrasegmental and intersegmental connections between neurons where  $\alpha_{i-k}^{lj}$  is the connection strength between cell  $j$  in segment  $i$  and cell  $l$  in segment  $k$ . The maximal synaptic conductance,  $G_0^{lj}$ , represents the flow of current between the two cells. Thus, the value of  $\alpha_{i-k}^{lj}$  represents the fraction of conductance between cells  $j$  and  $l$  for connections of length  $i - k$ . When  $i = k$ , we have the intrasegmental connections depicted in Figure 2.1. These same 6 connections are repeated along the chain from one segment to all other segments. For example, within each segment, the left L cell is connected to the left C cell. The left L cell is also connected to the left C cell in every other segment in the chain. The maximal synaptic conductance,  $G_0^{lj}$ , represents the flow of current between the two cells. The function  $\bar{h}$  represents the effect of the presynaptic cell on the postsynaptic cell. Note in the neural model studied by Buchanan [8] and Williams [72] the threshold function  $\bar{h}$  is a piecewise-linear function where below a certain threshold  $\bar{h} = 0$ . This represents the threshold for depolarization needed to activate the neurons. We choose a smooth version of this threshold function to facilitate our bifurcation analysis in Section 2.4. Finally,  $V_{\text{syn}}^l$  represents the reversal potential of cell  $l$  and the difference between the current voltage of cell  $i$  and the reversal potential is what drives the oscillations of the system. Note for excitatory connections  $V_{\text{syn}}^l = 1$  and for inhibitory connections  $V_{\text{syn}}^l = -1$ . The final summation term represents the input from edge cells during bending. We assume that bending activates the edge cells only at the segment where bending occurs, designated by  $m$ . We assume that all four of the edge cell connections have connection strength  $\alpha_f$ . Table 2.1 summarizes the parameters of (2.1) and their values. Note that although the model is connectionist, its form is similar to conductance-based models as the Hodgkin-Huxley

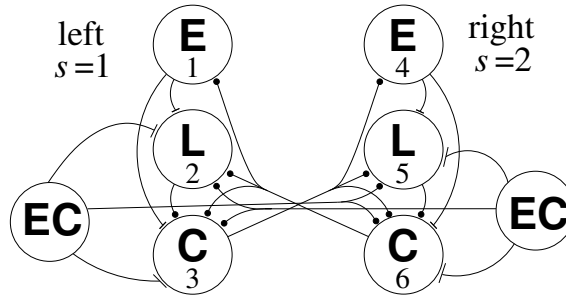


Figure 2.1: Connectivity of one segmental oscillator. Cell classes are excitatory interneurons (E), lateral inhibitory interneurons (L), crossed inhibitory interneurons (C), and edge cells (EC). Bars and circles indicate excitatory and inhibitory connections, respectively. We assume edge cells are only active in the segment at which bending occurs.

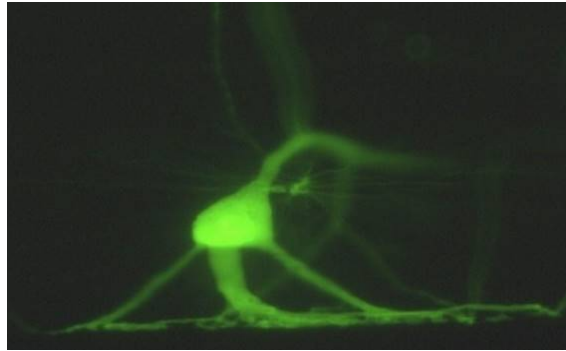


Figure 2.2: Stain of an edge cell showing the dendrites synapsing onto the side of the spinal cord and the axon extending down the lateral tract. Image courtesy of Tytell and Buchanan (2015).

model [31] with the time derivative of voltage proportional to the sum of “current”, each with its own reversal potential. The reversal potentials are in the range from -1 to 1, so that voltage remains in this same range.

### 2.3 Derived Phase Model

To test the hypothesis of how coupling asymmetry (differences between ascending and descending coupling strengths) affects the shape of entrainment ranges as a function of forcing position, we study another phase model which is derived from the neural model

Table 2.1: Neural model parameters used for simulations and to compute the derived phase model.

Parameter	Description	Value	Restrictions
$n$	number of segmental oscillators	10	
$m$	index of forced oscillator	varies	$1 \leq m \leq n$
$G_R$	resting conductance	$3.5 \text{ s}^{-1}$	
$G_T^j$	tonic excitatory conductance	$0.875 \text{ s}^{-1}$	E cells
		$0.350 \text{ s}^{-1}$	L cells
		$3.500 \text{ s}^{-1}$	C cells
$G_0^{kl}$	maximal synaptic conductance of intersegmental connection	$15 \text{ s}^{-1}$	L to C connection
		$35 \text{ s}^{-1}$	all other connections
$V_{\text{syn}}^l$	synaptic reversal potential for intersegmental connection	1	excitatory connections
		-1	inhibitory connections
$\sigma$	smoothing parameter of threshold function	0.05	
$\alpha_r^{lj}$	intersegmental connection strength	see Fig. 2.6	
$A_d$	amplitude of descending coupling	varies	
$A_a$	amplitude of ascending coupling	varies	
$\lambda_d$	length constant of descending coupling	varies	
$\lambda_a$	length constant of ascending coupling	varies	
$\alpha_f$	forcing strength	varies	
$\omega_f$	forcing frequency	varies	
$V_{\text{syn,ec}}^{sj}$	synaptic reversal potential for EC connection	1	excitatory connections
		-1	inhibitory connections
$G_f^{sj}$	maximal synaptic conductance of EC connections	1	

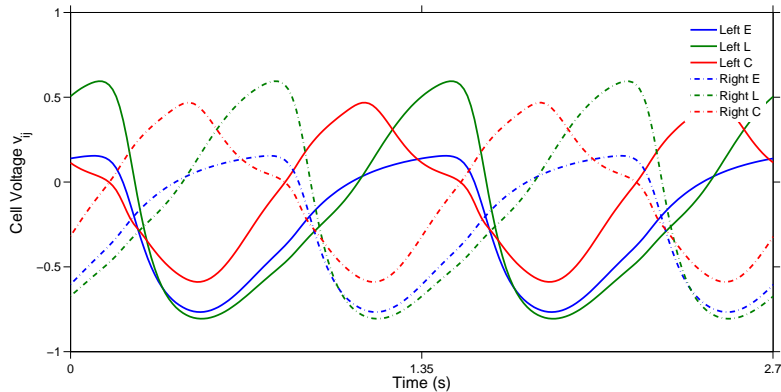


Figure 2.3: Steady state solution of the cell voltages in the first segment of a chain of coupled oscillators defined by (2.1) for two cycles without forcing. For this simulation weak intersegmental coupling, defined by  $A_a = 0.0004$ ,  $A_d = 0.0002$ , and  $\lambda_a = \lambda_d = 4$ , was used to connect oscillators. Since weak coupling was used, the simulation provides a good approximation of the voltages within a single segment of an uncoupled oscillator. Note the spatiotemporal symmetry between left and right cells. The voltage of the left cells is the same as the voltage of the right cells except for a phase shift of half a period.

given by (2.1). A phase model is a linearization around the limit cycle of the neural model and represents each anatomical segment of the CPG with a single variable. Previte et al. [57] studied a phase model with sinusoidal coupling functions. However, instead of using sine functions to couple the oscillators, we use the neuron-to-neuron connections in the neural model to compute intersegmental connections between oscillators. We exploit the theory of weakly coupled oscillators [10, 55, 54] to approximate the neural model given by (2.1) by a phase model of the form:

$$\dot{\theta}_i = \omega_0 + \sum_{\substack{k=1 \\ k \neq i}}^n \sum_{j=1}^6 \sum_{l=1}^6 \alpha_{i-k}^{lj} H^{lj}(\theta_k - \theta_i) + \delta_{im} \alpha_f \sum_{s=1}^2 \sum_{j=1}^6 H_f^{sj}(\theta_f - \theta_i), \quad \text{for } i = 1, \dots, n, \quad (2.2a)$$

$$\dot{\theta}_f = \omega_f \quad (2.2b)$$

under the assumptions that intersegmental connection strengths  $\alpha_{i-k}^{lj}$  ( $i - k \neq 0$ ) and forcing strength  $\alpha_f$  are small and  $\omega_f$  is close to  $\omega$ . The function  $H^{lj}$  describes the coupling

provided by a single intersegmental connection of unit strength from cell  $l$  in one segment to cell  $j$  in another segment. The double summation term represents input from the edge cells and is multiplied by  $\delta_{im}$  which denotes the Kronecker-delta function, defined by

$$\delta_{im} = \begin{cases} 1 & \text{if } i = m \\ 0 & \text{otherwise,} \end{cases} \quad (2.3)$$

so that edge cells only contribute to cell voltages in the segment where forcing is applied. The  $H_f^{sj}$  function describes the coupling provided by a connection of unit strength from the edge cell on side  $s$  of segment  $m$  to cell  $j$  in the same segment. Note we no longer consider intrasegmental coupling since each segment is represented by a single variable.

Recall that intersegmental connections have the same connectivity as the intrasegmental connections shown in Figure 2.1. For example, given coupling length  $r = i - k$ , there are 12 nonzero  $\alpha_r^{lj}$  corresponding to the left and right connections for each of 6 connection types: E to C, E to L, L to C, C to E, C to L, and C to C. Note a negative connection length ( $k > i$ ) represents an ascending connection, towards the head, and a positive connection length ( $i < k$ ) represents a descending connection, towards the tail. Due to the right-left symmetry of the neural model and the left-right spatiotemporal symmetry of the segmental oscillator's limit cycle, two connections of the same type have the same connection strength and same coupling function. Note these symmetries can be seen in Figure 2.3 which depicts the steady state of a single oscillator in the neural model simulated with no forcing. The left and right cells have the same voltage with a phase shift of half a period. Therefore, we can write

$$\sum_{j=1}^6 \sum_{l=1}^6 \alpha_r^{lj} H^{lj} = \sum_{c \in \mathcal{C}} \alpha_{rc} H_c, \quad \text{where } \mathcal{C} = \{\text{EL, EC, LC, CE, CL, CC}\} \quad (2.4)$$

and where, for example,  $\alpha_{r,EL} = \alpha_r^{12} = \alpha_r^{45}$  and  $H_{EL} = H_r^{12} + H_r^{45} = 2H_r^{12}$ . Let  $\alpha_r$  be the

mean of  $\alpha_{rc}$  for  $c \in \mathcal{C}$ . We define  $H_r$ , the coupling function of length  $r = i - k$ , as

$$H_r = \frac{1}{\alpha_r} \sum_{j=1}^6 \sum_{l=1}^6 \alpha_r^{lj} H^{lj} = \sum_{c \in \mathcal{C}} \frac{\alpha_{rc}}{\alpha_r} H_c. \quad (2.5)$$

Similarly, the 8 edge cell connections of Figure 2.1 consist of two connections for each of the four connection types: EC to Li, EC to Ci, EC to Lc, and EC to Cc, where ‘i’ and ‘c’ indicate ipsilateral and contralateral connections, respectively. Therefore, we can define the forcing coupling function  $H_f$  as

$$H_f = \sum_{s=1}^2 \sum_{j=1}^6 H_f^{sj} = H_{f,\text{Li}} + H_{f,\text{Ci}} + H_{f,\text{Lc}} + H_{f,\text{Cc}}, \quad (2.6)$$

where, for example,  $H_{f,\text{Li}} = H_f^{11} + H_f^{25} = 2H_f^{11}$ . Now, using (2.5) and (2.6), we can write the phase model (2.2) as

$$\dot{\theta}_i = \omega_0 + \sum_{\substack{k=1 \\ k \neq i}}^n \alpha_{i-k} H_{i-k}(\theta_k - \theta_i) + \delta_{im} \alpha_f H_f(\theta_f - \theta_i), \quad \text{for } i = 1, \dots, n, \quad (2.7a)$$

$$\dot{\theta}_f = \omega_f. \quad (2.7b)$$

Model (2.7) has the standard form of a chain of coupled phase oscillators forced at one location. To specify this model, two choices remain. First, for each connection length  $r$  we must specify the connection strength ratios  $\alpha_{rc}/\alpha_r$  in (2.5) that determine the coupling function  $H_r$ . We defer this specification until we have computed the coupling function  $H_c$  for each connection type  $c$  (see Figure 2.5 below). Second, we must specify how coupling strength  $\alpha_r$  depends on  $r$ . Experimental evidence does not provide the exact form of this dependence but does indicate an asymmetry in ascending and descending coupling strengths [73, 37, 49]. Among the possible modeling choices in the literature (e.g. [53, 16]), we will follow Varkonyi et al. [67] and assume that coupling strength decays exponentially with coupling length:

$$\alpha_r = \begin{cases} A_d e^{-|r|/\lambda_d} & \text{for } r > 0 \text{ (descending connections),} \\ A_a e^{-|r|/\lambda_a} & \text{for } r < 0 \text{ (ascending connections),} \\ 1 & \text{for } r = 0 \text{ (intra-segmental connections),} \end{cases} \quad (2.8)$$

where  $A_d, \lambda_d$  and  $A_a, \lambda_a$  are the amplitudes and length constants for descending and ascending coupling, respectively. Representative parameter values can be found in the caption of Figure 2.9.

### 2.3.1 Coupling Functions

To define the functions  $H_r$  and  $H_f$  in (2.7) we use the methods of phase reduction and averaging (see [26, 42, 32]) as applied to weakly coupled oscillators [67]. Under the assumption of weak coupling in (2.1), we can describe the intra-segmental connections in the neural model as a phase dependent coupling function for each connection type,  $H_c$ . The coupling functions  $H_c$  are computed as in [67]. The first step of this process is to compute phase response curves (PRCs) for the six intra-segmental connection types in the neural model. A PRC describes the effect of a perturbation applied to a single cell inside the oscillator on the resulting phase of the oscillator after several periods. To numerically compute the PRC for a cell in the neural model, we first simulate a single segment with no forcing until steady state voltages are reached. At steady state all cell voltages have the same period although they do not have the same trajectories. Note these are the voltages shown in Figure 2.3. To define a cycle, we define the starting point to be the positive going zero crossing for the left E cell. This zero crossing now represents phase 0 for all the cells. We can normalize the period so that the phases go from 0 to 1 where phase 0 corresponds to the first zero crossing and phase 1 represents the return to this point. We then divide the cycle into 100 equally spaced phases. To determine the PRC for the left E cell, we add a perturbation to the cell voltage at a given phase, say  $\theta_k$ . We then

simulate for several more cycles and measuring the resulting phase shift in the left E cell. This phase shift is the value of the PRC for the left E cell at phase  $\theta_k$ . We repeat this process for all 100 phases and store the resulting phase shifts. This vector of phase shifts describes how the left E cell responds to perturbations at each phase in the cycle. Figure 2.4 illustrates the PRCs for the left E, L, and C cells in the neural model (2.1). Note the PRCs for the right cells would be the same as their left side counterparts except for a phase shift of 0.5.

Here we review the theory of weakly coupled oscillators and how to apply phase reduction and averaging to reduce the chain of oscillators to a phase model. For a complete description of phase reduction applied to weakly coupled oscillators see, for example, [26].

Consider a system of  $n$  weakly coupled oscillators of the form

$$\dot{x}_i = f(x_i) + \epsilon g(x_i, x_j, \dots) \quad (2.9)$$

where  $x_i \in \mathbb{R}^n$  and each  $x_i$  has a periodic limit cycle  $\Gamma_i$  with period  $T_0 = 2\pi/\omega_0$ . The function  $g$  represents the coupling between oscillators and the assumption of weak coupling means that  $\epsilon$  is sufficiently small. Then, we can write (2.9) as an ordinary differential equation for the phase of the oscillator:

$$\dot{\phi}_i = \omega_0 + \epsilon z(\phi_i) \cdot g(x_i(\phi_i), x_i(\phi_j), \dots)|_{\Gamma_0(\phi_i)} \quad (2.10)$$

where each component of  $z(\phi_i)$  is a PRC. To further simplify the system and apply the averaging technique, we substitute the slow phase  $\psi_i = \phi_i - \omega_0 t$  into (2.10) to get

$$\dot{\psi}_i = \epsilon h_i(\psi_i - \psi_j), \quad (2.11)$$

where  $h_i$  is a function of phase differences. The functions  $h_i$  are computed by averaging:

$$h_i(\psi_i - \psi_j) = \frac{1}{T_0} \int_0^{T_0} z(\phi_i) \cdot g(x_i(\phi_i), x_i(\phi_j), \dots) dt. \quad (2.12)$$

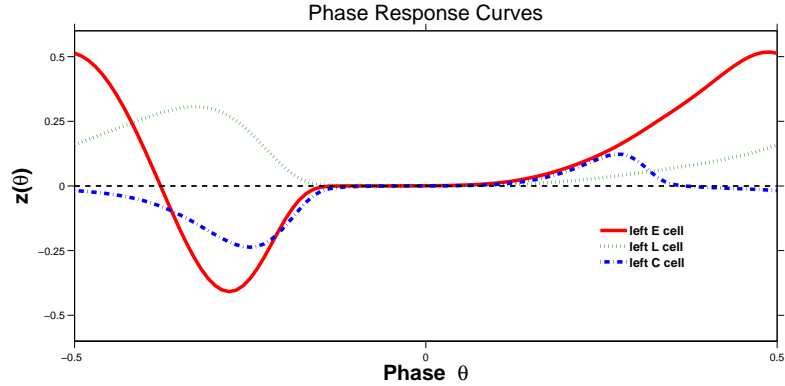


Figure 2.4: The PRCs are plotted for the left E, L, and C cells. Each PRC describes the resulting phase shift that occurs when that cell's voltage is perturbed by  $10^{-6}$ , at various initial phases. PRCs for right E, L and C cells are the same except for a phase shift of 0.5 due to the right-left symmetry within each oscillator.

It has been shown ([10, 55, 54]) that for a system of the form (2.9) with weak coupling, we can reduce the system to phase equations that depend only on relative phases of oscillators and not individual cell voltages.

Recall, intersegmental coupling functions defined by (2.5) are computed from a linear combination of the 6 neuron-to-neuron connections  $H_c$ , computed using (2.12). In (2.5),  $\alpha_{rc}$  determines how much each neuron-to-neuron connection of length  $r$  contributes to the intersegmental connection for oscillators  $i$  and  $k$  where  $r = i - k$ . The choice of  $\alpha_{rc}$  determines the phase lag between oscillators. Experimentally, a phase lag of approximately 1% of the cycle per segment has been observed [11, 74]. This means that as neural activity travels down the CPG, the phase difference between consecutive segments is 0.01. We use the tuning methods in [37] to determine the appropriate  $\{\alpha_{rc}\}$ . Tuning is a method which moves the zeros of the coupling functions and the zeros in our case correspond to the phase lag in the chain of oscillators. To tune the intersegmental connections we vary  $\alpha_{EC}$  and  $\alpha_{LC}$  until  $H_r$  has a zero at  $0.01r$ . After tuning, for a chain of ten oscillators, we have 18 intersegmental connection functions  $H_r$  for  $r = -9, \dots, -1, 1, \dots, 9$  representing both

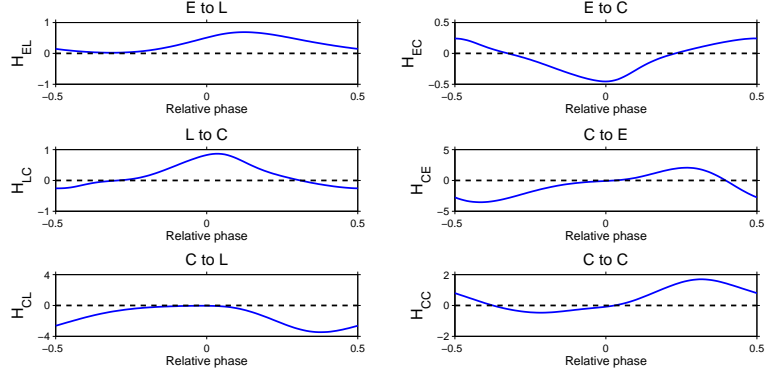


Figure 2.5: For each type of neural connection between E, L, and C cells, an  $H_c$  function is computed to represent the effects of neurons on the voltage of the neuron within the oscillator. The six  $H_c$  functions are computed for connections from L to E cells, C to E cells, C to L cells, E to C cells, L to C cells, and C to C cells. These six connections represent only half of the neuron-to-neuron connections in Figure 2.1 since the other six connections can be determined from the left-right symmetry within each oscillator.

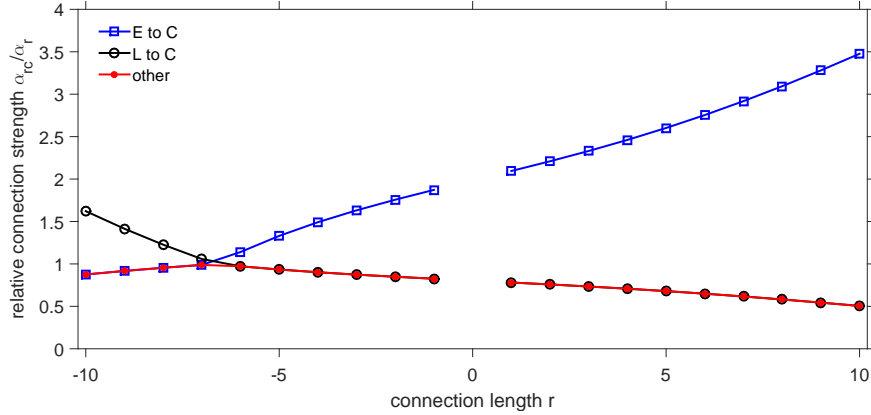


Figure 2.6: Relative strengths  $\alpha_{rc}/\alpha_r$  of different connection types as a function of connection length  $r$  and connection type  $c$ .

ascending and descending connections. Each  $H_r$  is then multiplied by  $\alpha_r$ , the average of the intrasegmental connection strengths of length  $r$ . The fraction of connection strength  $\alpha_{rc}/\alpha_r$  is depicted in Figure 2.6 for the different cell-to-cell connections.

This involves varying  $\alpha_{rc}$  and computing the resulting zeros of  $H_r$ . Increasing or decreasing the  $\alpha_{rc}$  values will shift the zeros of  $H_r$  to the right or left. The zeros of the intersegmental connection functions determine the phase lag. Thus, we want the zero of  $H_r$  to occur at  $0.01r$  to model the 1% per segment phase lag seen in the experiments.

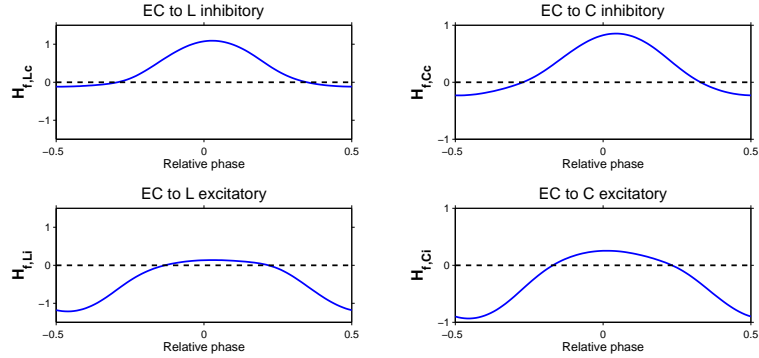


Figure 2.7: For each type of neural connection from edge cells, an  $H_{f,c}$  function is computed that describes the strength of that connection as a function of relative phase between the edge cell and the oscillator where forcing is applied.

### 2.3.2 Forcing Connections

A method similar to the method used to compute intersegmental coupling functions  $H_r$  is used to compute  $H_f$ , where cell  $i$  is replaced by an edge cell. Hence,  $\theta_i$  will represent the phase of the forcer, which has period  $T_f = 1/\omega_f$ . Again, we compute PRCs for these connections where  $G_{1i}^{1j}$  is replaced by  $G_f^{1js}$  and  $V_{syn}^i$  is replaced by  $V_{syn,ec}^{is}$  for forcing connections. There are left and right edge cells in each oscillator and each edge cell is connected to right and left L and C cells. Edge cells excite neurons on the same side and inhibit neurons on the opposite side. Since the oscillator is symmetric, we compute the four  $H_{f,c}$  connection functions for a single edge cell where  $c$  denotes a right or left L or C cell. These connections are repeated for the edge cell on the other side of the oscillator, so we end up with two of each type of connection. The four functions representing the neural model's edge cell connections are computed using (2.10) where the coupling function  $g$  is replaced by the appropriate edge cell connection from the neural model. These edge cell connection functions are depicted in Figure 2.7 for the left edge cell. As described by (2.6), the forcing function  $H_f$  in (2.7) is defined as the sum of all of the edge cell connections. Here we assume that each edge cell connection contributes equally to the overall forcing

connection (each function has coefficient 1).

At this point, we have computed all components of the phase model: intersegmental connections,  $H_r$ , and forcing connection,  $H_f$ . However, rather than use the phase model directly, we instead consider the relative phase model by looking at the phase difference between each oscillator and the phase of the forcer. This is characterized by the change of variable  $\phi_i = \theta_f - \theta_i$  which transforms (2.7) to

$$\dot{\phi}_i = \delta - \sum_{\substack{k=1 \\ k \neq i}}^n \alpha_{i-k} H_{i-k}(\phi_i - \phi_k) - \delta_{im} \alpha_f H_f(\phi_i), \quad \text{for } i = 1, \dots, n, \quad (2.13)$$

where  $\delta = \omega_f - \omega_0$ . In the phase model, entrainment corresponds to stable periodic orbits, whereas in the relative phase model, entrainment corresponds to stable fixed points of (2.13). When the CPG is entrained to the forcing frequency, the phase difference between a given oscillator in the chain and the forcing oscillator remains constant. Using the relative phase model allows us to use continuation and fixed point stability analysis, which we can exploit to find entrainment ranges.

## 2.4 Entrainment Ranges

In this section, entrainment ranges are computed as a function of forcing position and forcing strength with several different choices of intersegmental coupling. For the neural model (2.1) a periodic solution entrained to a given forcing frequency corresponds to a fixed point of the Poincaré map. For the relative phase model, the CPG is entrained when the relative phases, that is the difference in phase between an oscillator in the chain and the forcing oscillator,  $\theta_f - \theta_i$ , are constant. This implies that all of the oscillators in the chain have the same frequency as the forcer, namely  $\omega_f$ . Constant relative phases correspond to stable fixed points of (2.13). In either case, entrainment ranges can be

computed by identifying stable fixed points.

Standard parameter continuation methods (see for example, [1]) are used to track fixed points in dynamical systems. For robustness of computation, we use a sequence of one parameter continuations along ellipses instead of straight lines. We used a series of one-parameter continuations instead of two-parameter continuation, because two-parameter continuation can become inaccurate near degenerate bifurcations [44]. Instead of looking at vertical slices of parameter space, we move through parameter space along ellipses. The larger dotted ellipses represent the path of the continuation steps in the parameter space. These ellipses indicate how the parameters  $\delta = \omega_f - \omega$  and  $\alpha_f$  are updated at each continuation step. We choose the size of these ellipses that is large enough to cover a relatively large area in parameter space and also small enough to capture sharp corners of the entrainment range. The small red circles indicate the center of continuation ellipses. To choose the next center, we take a step in the same direction as the previous entrainment point. The points on the entrainment range are indicated by blue plus signs. To better explain this process, consider entrainment points 2 and 3 in Figure 2.8. We start with entrainment point 2, which is a known point on the entrainment range. To get the next center, indicated by the small red circle between points 2 and 3, we step in the same direction as the vector from point 1 to point 2. We then move around the large ellipse, plotted in magenta, and find new fixed points with slightly different values of  $\alpha_f$  and  $\delta$ . To determine points on the boundary of the entrainment range, we look at the stability of the fixed points in each model. Stability is assessed by computing the eigenvalues of the Jacobian evaluated at the fixed point. Entrainment is lost when we reach an unstable fixed point, and we record the values  $\alpha_f$  and  $\delta$  values correspond to the loss of stability and hence, the boundary of the entrainment range.

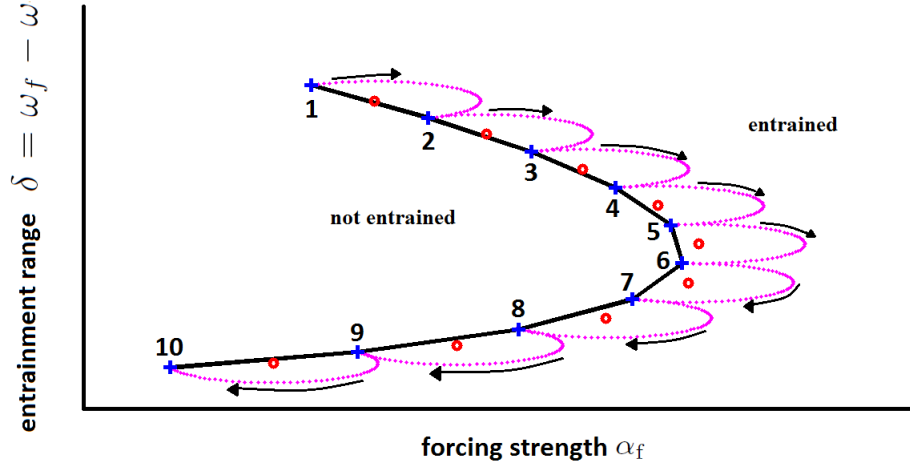


Figure 2.8: Illustration of our elliptical two-parameter continuation method used to find entrainment ranges as a function of forcing strength. The dotted circles denote how the values of  $\delta = \omega_f - \omega_0$  and  $\alpha_f$  are updated at each continuation step. The plus signs denote points on the entrainment range that are detected by the continuation circles. This allows us to detect sharp corners that may be missed with standard one-parameter continuation.

#### 2.4.1 Entrainment Ranges as a Function of Forcing Strength

Using our continuation algorithm, entrainment ranges are computed for both the neural model and the derived phase model as a function of forcing strength. Figure 2.9 illustrates 1:1 entrainment ranges for a chain of ten oscillators forced at the last oscillator as a function of forcing strength  $\alpha_f$ . The entrainment range, as a function of forcing strength, is plotted relative to the unforced, average frequency of the chain that is, the vertical axis represents the difference between the forcing frequency,  $\omega_f$  and the natural chain frequency  $\omega$ . Figure 2.9A, illustrates entrainment ranges for both the neural model (indicated by the blue line) and the derived phase model (indicated by the red line) for weak intersegmental coupling strength corresponding to  $A_d = 0.0004$ ,  $A_a = 0.0002$ , and  $\lambda_d = \lambda_a = 4$  in equation (2.8). Figure 2.9B illustrates entrainment ranges with intersegmental coupling strength 100 times stronger than in Figure 2.9A ( $A_d = 0.04$ ,  $A_a = 0.02$ ). Together Figures 2.9A and 2.9B illustrate the approximate scaling of entrainment ranges

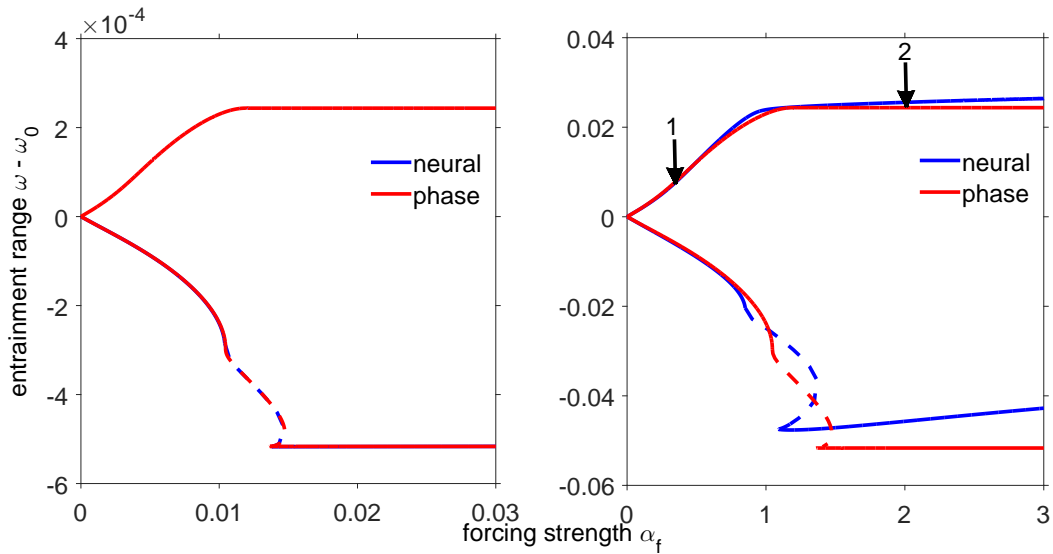


Figure 2.9: Entrainment ranges for the neural and derived phase models as a function of forcing strength. Figure 2.9A on the left illustrates entrainment ranges as a function of forcing strength for weak intersegmental coupling corresponding to  $A_a = 0.0004$ ,  $A_d = 0.0002$ , and  $\lambda_a = \lambda_d = 4$ . Figure 2.9B on the right illustrates entrainment ranges for 100 times stronger intersegmental coupling with  $A_a = 0.04$  and  $A_d = 0.02$ . Note that the size of the entrainment range scales with the coupling strength, that is, the entrainment ranges in B are 100 times larger than the entrainment ranges shown in A. For weak coupling the entrainment ranges for the neural and derived phase models match closely while for strong coupling the entrainment ranges start to differ as forcing strength increases. The dashed line on both plots represents Hopf bifurcations that occur when entrainment is lost. Smooth lines denote saddle-node bifurcations. The arrows in Figure 2.9B correspond to the forcing strength values  $\alpha_f$  where loss of entrainment is depicted in Figures 2.12.

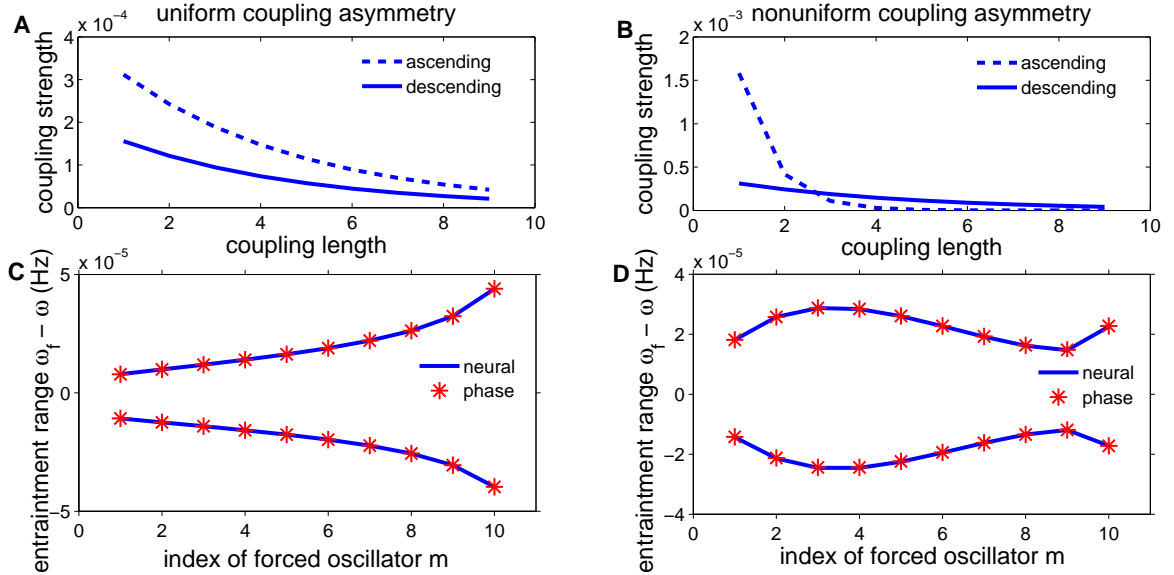


Figure 2.10: Entrainment ranges as a function of forcing position for varying intersegmental connections. Uniform coupling asymmetry is illustrated in A with  $A_a = 0.0004$ ,  $A_d = 0.0002$ , and  $\lambda_a = \lambda_d = 4$ . All of the ascending coupling strengths are stronger than descending for all connection lengths. This coupling scheme is used to produce monotonic entrainment ranges as a function of forcing position, seen in C. Nonuniform coupling asymmetry is depicted in B with  $A_a = 0.006$ ,  $A_d = 0.0004$ ,  $\lambda_a = 0.75$ , and  $\lambda_d = 4$ . For our choice of parameters, ascending connections become stronger at connections of length 3. Nonuniform coupling is used to compute the entrainment range in D, where see non-monotonic entrainment ranges.

with intersegmental coupling strength. For stronger coupling, the derived phase model captures the general properties of the neural entrainment range but not the details as seen in Figure 2.9B. In the limit of weak coupling, as in Figure 2.9A, both the neural model and the derived phase model agree almost exactly, including the type of bifurcation that occurs when entrainment is lost. The smooth lines correspond to saddle-node bifurcations and the dashed lines represent Hopf bifurcations. For strong coupling, the phase model is not as good of a quantitative approximation of the neural model, but does capture the same qualitative features of the entrainment range of the neural model, including bifurcation type.

### 2.4.2 Entrainment Ranges as a Function of Forcing Position

Figure 2.10 illustrates the effect of different types of intersegmental coupling on entrainment ranges plotted as a function of forcing position. Figure 2.10A shows the strength of connections plotted as a function of connection length for both ascending and descending coupling and corresponds to equation (2.8) with parameters  $A_a = 0.0004$ ,  $A_d = 0.0002$ , and  $\lambda_a = \lambda_d = 4$ . Strength of the ascending connections are uniformly stronger than descending connection strengths, hence we refer to this intersegmental coupling scheme as uniform coupling asymmetry. Similarly, Figure 2.10B shows connection strengths, again as a function of connection length, for both ascending and descending connections where  $A_a = 0.006$ ,  $A_d = 0.0004$ ,  $\lambda_a = 0.75$ , and  $\lambda_d = 4$ . Note in this case, for connections of length 1 and 2, ascending strengths are stronger than descending strengths, but the curves cross transversely (at approximately coupling length 3), and descending strengths are now stronger than ascending. We refer to this coupling scheme as nonuniform coupling asymmetry.

We consider entrainment ranges as a function of forcing position to test the hypothesis that nonuniform coupling asymmetry produces larger entrainment ranges when forcing the middle of the chain of oscillators than when forcing at either end. We compute entrainment ranges as a function of forcing position  $m$  for the examples of uniform and nonuniform asymmetric coupling illustrated in Figure 2.10C and D. For each pair of coupling strength functions, entrainment range is plotted as a function of forcing position  $m$ . Figure 2.10C and 2.10D depict entrainment ranges for both the neural (blue line) and derived phase (stars) models. When the chain has uniform intersegmental coupling asymmetry (Figure 2.10A), entrainment range is a monotonically increasing function of forcing

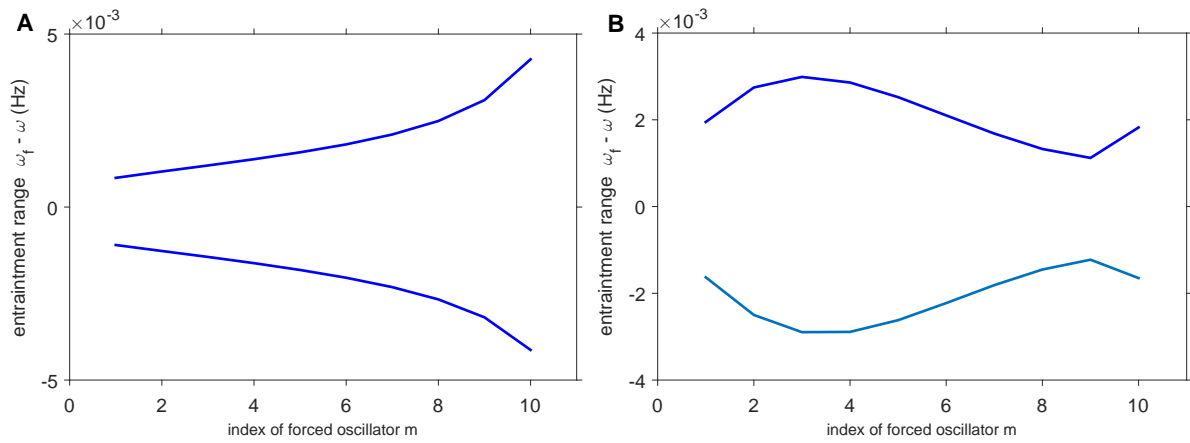


Figure 2.11: Entrainment ranges as a function of forcing position for varying intersegmental connections in the neural model. Figure 2.11a shows the entrainment range for strong uniform coupling asymmetry with  $A_a = 0.04$ ,  $A_d = 0.02$ , and  $\lambda_a = \lambda_d = 4$ . Figure 2.11b shows the entrainment range for strong nonuniform coupling asymmetry with  $A_a = 0.6$ ,  $A_d = 0.04$ ,  $\lambda_a = 0.75$ , and  $\lambda_d = 4$ . Note that even with strong intersegmental coupling the neural model requires nonuniform coupling asymmetry to produce non-monotonic entrainment ranges.

position, as seen in Figure 2.10C for both the neural and derived phase model. When the chain has non-uniform intersegmental coupling asymmetry (Figure 2.10B), entrainment range is a non-monotonic function of forcing position, since the largest entrainment range occurs at  $m = 3$ , as seen in Figure 2.10D. Nonuniform coupling asymmetry produces qualitatively the same entrainment ranges as a function of forcing position as the experimental data and supports the hypothesis of Previte et al. [57] that monotonic entrainment ranges as a function of forcing position are not a generic property of coupled oscillators but rather depends on intersegmental coupling properties. Further, note that since coupling strength is relatively weak, the phase model acts as a very good approximation of the neural model. To test the effect of intersegmental coupling strengths, we also compute entrainment ranges as a function of forcing position for strong intersegmental coupling. These entrainment ranges are shown in Figure 2.11. Note we only plot the entrainment ranges for the neural model because the phase model closely approximates the neural model only in the limit of weak intersegmental coupling. For stronger intersegmental connections we see the same qualitative entrainment ranges as in Figure 2.10. Thus, the strength of the connections does not affect the shape of the entrainment range and this further supports the hypothesis that the nonuniform coupling asymmetry is responsible for non-monotonic entrainment ranges.

## 2.5 Loss of Entrainment

Previous analytic results only considered internal loss of entrainment in a phase model [40]. Previte et al. [57] characterized loss of entrainment for the sinusoidal phase model, as either internal or external. Internal loss of entrainment occurs when part of the chain follows  $\omega_i^* = \omega_f$  but for the rest of the chain  $\omega_i^* \neq \omega_f$ . This split can occur

above or below the oscillator where forcing is applied, corresponding to rostral or caudal internal loss of entrainment. External loss of entrainment occurs when  $\omega_i^*$  are equal for all oscillators in the chain but are not equal to the forcing frequency  $\omega_f$ . Previte et al. [57] also showed that internal loss of entrainment is more likely when forcing strength  $\alpha_f$  is strong relative to coupling strengths  $\alpha_r$ . Our simulations of loss of entrainment in Figure 2.12 support this conclusion. For relatively weak forcing strength,  $\alpha_f = 0.5$ , entrainment is lost externally for both the neural and derived phase models. Alternatively, for stronger forcing strength,  $\alpha_f = 2$ , entrainment is lost internally where oscillator 9 has a different frequency than oscillator 10. These results support the claim that experimental entrainment needs to be re-examined to determine how entrainment is lost at the middle and ends of the chain [57]. Experimental procedures make it difficult to classify exactly how entrainment is lost. Moreover, experimental entrainment ranges plot the average frequency of the oscillators in the chain, which obscures more subtle differences [57].

To compare with the analytic loss of entrainment results described in [57], we characterize how entrainment is lost outside of the entrainment ranges for the neural and derived phase model. In the sinusoidal phase model, entrainment is lost solely through saddle-node bifurcations. However, in both the neural and derived phase models, entrainment is lost either via a saddle-node bifurcation or a Hopf bifurcation (also known as a Neimark-Sacker bifurcation) of the Poincaré map [27]. Lines of saddle-node and Hopf bifurcations meet at a codimension-two Bogdanov-Takens bifurcation of the Poincaré map [6]. The type of bifurcation varies along the lower branches of the entrainment ranges as seen in Figure 2.9. Unlike the entrainment ranges of the sinusoidal phase model of Previte et al. [57], the entrainment ranges of the derived phase model capture the types of bifurcations seen in the entrainment ranges of the neural model.

Following the definitions of loss of entrainment in [57], we investigate internal versus external loss of entrainment in the CPG models. Figures 2.12A-D illustrate loss of entrainment for the neural model and Figures 2.12E-H illustrate loss of entrainment for the derived phase model for two values of forcing strength as indicated by the arrows in Figure 2.9B. For small values of the forcing strength  $\alpha_f$ , the size of the entrainment range increases approximately linearly with  $\alpha_f$  as illustrated in Figure 2.9 and entrainment at both the lower and upper limits of the entrainment range is lost via saddle-node bifurcations. For forcing strength sufficiently large, the entrainment range is approximately constant as seen in Figure 2.9.

Figure 2.12A corresponds to simulating the model described by (2.1) with  $\omega_f$  chosen so that  $\omega_f - \omega$  is just above (+0.0002) the entrainment range illustrated in Figure 2.9B for  $\alpha_f = 0.5$ . Figure 2.12A illustrates that segmental oscillators 9 and 10 are losing one cycle with the forcer. Figure 2.12B shows a corresponding spike in the cycle period at each step in the relative phase. Simulating with  $\alpha_f = 0.5$  just below the entrainment range would produce a similar result to Figure 2.12A, except the segmental oscillator will gain one cycle with the forcer. The loss of entrainment illustrated in Figure 2.12A and B corresponds to external loss of entrainment because segments nine and ten (representative of the entire chain) are oscillating together and losing a cycle with the forcer at each step.

Figure 2.12C also demonstrates loss of entrainment but in this case  $\alpha_f = 2$  and  $\omega_f$  chosen so that  $\omega_f - \omega$  is just above (+0.0002) the entrainment range illustrated in Figure 2.9B. Forcing is still on the tenth oscillator, but instead of both oscillators nine and ten losing or gaining a cycle with the forcer at the same time, Figure 2.12C shows that oscillator nine is losing a cycle with the forcer, whereas oscillator ten is still oscillating with the forcer. Figure 2.12D shows a spike in the cycle period as was seen in Figure 2.12C

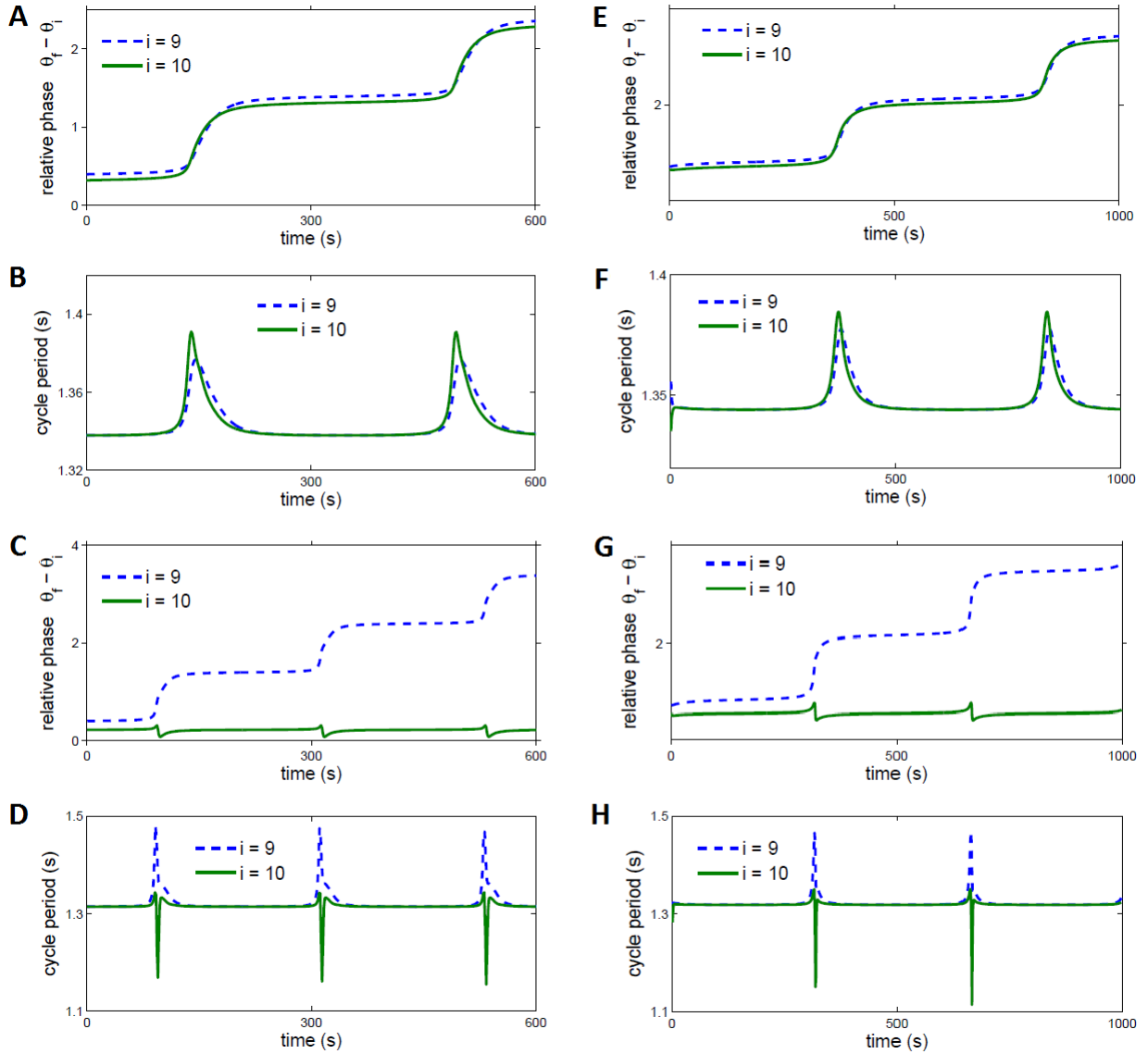


Figure 2.12: Comparison of loss of entrainment for the neural (A-D) and derived phase (E-H) models. Figures 2.12A and E show phase relative to the forcer for external loss of entrainment with  $\alpha_f = 0.5$  and  $\omega_f - \omega$  is  $+0.0002$  above the entrainment range as indicated by arrow 1 in Figure 2.9B, where A is a simulation of the neural model and E is a simulation of the derived phase model. Figures 2.12C and F show relative phase for internal loss of entrainment with  $\alpha_f = 2$  and  $\omega_f - \omega$  is  $+0.0002$  above the entrainment range indicated by arrow 2 in 2.9B. Figures 2.12B and F and 2.12D and H show cycle period for external and internal loss of entrainment respectively.

at each step in relative phase. This loss of entrainment corresponds to internal loss of entrainment because part of the chain is oscillating at the same frequency with the forcer and another part is not. Internal loss of entrainment can be characterized further as rostral or caudal. Rostral loss of entrainment means that segmental oscillators above the forced oscillator have a different average frequency than the forcer, but the oscillators below the forced oscillator have the same average frequency as the forcer. On the other hand, caudal loss of entrainment means that the loss of entrainment takes place for oscillators below the forced oscillator. Since we consider the case where forcing is applied to the last oscillator in the chain, we can only see rostral loss of entrainment where oscillators 1 through 9 have a different frequency  $\omega_i^*$ . The neural model described by (2.1) exhibits both external loss of entrainment for the entrainment ranges that grow linearly as a function of  $\alpha_f$ , and internal loss of entrainment where the entrainment ranges are a relatively constant function of  $\alpha_f$  (see Figure 2.9). The loss of entrainment near the Hopf bifurcation in Figure 2.9 is more complex and does not clearly fall into either of these two categories.

Both internal and external loss of entrainment is also seen in the derived phase model. In Figure 2.12E, entrainment is lost externally for forcing frequency above the entrainment range for  $\alpha_f = 0.5$ . Figure 2.12G shows internal loss of entrainment for  $\alpha_f = 2$ . As in the neural model, Figures 2.12E and F illustrate how the the oscillators gain a cycle with the forcer. In Figure 2.12E, all 10 oscillators have the same frequency  $\omega_i^* \neq \omega_f$  while in Figure 2.12F,  $\omega_{10}^* = \omega_f$  but oscillators 1 through 9 have a different frequency. Figures 2.12G and H illustrate the jump in cycle period where the relative phases gain a cycle with relation to the forcing frequency.

For the upper bound on the entrainment range, entrainment is lost externally for small values of  $\alpha_f$  when the entrainment range is growing linearly as a function of  $\alpha_f$ ,

whereas entrainment is lost internally in the range of  $\alpha_f$  where the entrainment range is relatively constant as a function of  $\alpha_f$ . In both these ranges, entrainment is lost through a saddle-node bifurcation of the return map in the Poincaré section. Hence, the type of loss of entrainment does not necessarily correspond to the type of bifurcation. Loss of entrainment just below the entrainment range exhibits more complicated behavior which, for some  $\alpha_f$  values, cannot be easily classified as internal or external. Finally, the derived phase model agrees with the neural model on how entrainment is lost at different locations along the entrainment range. This further illustrates that the derived phase model preserves entrainment information about the more biologically detailed neural model.

## 2.6 Discussion

Motivated by the experimental results of Tytell and Cohen [66] and the modeling results of Previtte et al. [57], we investigated the entrainment properties of both a neural and derived phase model. As expected based on the theory of phase reduction for weakly coupled oscillators, we saw the entrainment characteristics of the neural model were closely approximated by the derived phase model in the limit of weak coupling. This included entrainment ranges as a function of forcing strength, entrainment ranges as a function of position, and also loss of entrainment. Additionally, we computed entrainment ranges as a function of forcing position with different coupling schemes. For both the neural and derived phase model we saw monotonic and non-monotonic entrainment ranges as a function of forcing position for uniform and nonuniform coupling asymmetry respectively. Entrainment is also lost in the same way in both models as illustrated by Figure 2.12. Comparing the entrainment results for the neural and derived phase models indicates that the derived phase model is able to capture all of the essential entrainment properties we

analyzed. Thus, with sufficiently weak coupling, entrainment can be studied in the simpler derived phase model. We can compare the coupling functions in the derived phase model to the coupling functions of other phase models (see [10, 57] for example). The simplicity of the phase model allows for future analysis, similar to the analysis done for the sinusoidal phase model [57].

Although both chains of coupled oscillators, the neural and derived phase models contain different levels of biological detail in comparison to the simpler sinusoidal phase model. Despite these differences, entrainment results are qualitatively similar across all three models. Entrainment ranges as a function of forcing position are plotted in Figure 2.10 for both the neural and derived phase models. We see similarly shaped entrainment ranges as a function of forcing position in our two models as well as the sinusoidal phase model studied by Previtte et al [57]. This supports the hypothesis that non-monotonic entrainment ranges are not an intrinsic property of chains of coupled oscillators but rather a characteristic of a specific type of intersegmental coupling. Specifically, nonuniform coupling asymmetry, in each model, produces entrainment ranges that do not increase monotonically as forcing position increases. Additionally, computational and experimental results have indicated coupling asymmetry exists in the lamprey CPG, but the strength and direction of connections is still unknown [37, 28]. More recently, experiments have been conducted that examine the distribution and connections of commissural interneurons. These experiments show differences in the rostrocaudal distribution of commissural interneurons [46] and differences in the synaptic organization of ipsi- and contralaterally projecting interneurons [4]. Ayali et al. experimentally showed differences in CPG output between blocking short ascending and descending connections, which further supports the idea of coupling asymmetry in the lamprey CPG [2]. From these results and our

simulations, we hypothesize that intersegmental connections in the lamprey CPG exhibit nonuniform coupling asymmetry. This is an important insight into the CPG since individual intersegmental connection strengths are extremely difficult to measure experimentally.

While the sinusoidal phase model agrees with the neural model for entrainment ranges as a function of forcing position for both uniform and nonuniform coupling asymmetry, it does not capture all of the properties of entrainment ranges as a function of forcing strength. In the sinusoidal phase model, entrainment ranges as a function of forcing strength,  $\alpha_f$ , are linear with slope depending on forcing position  $m$  and  $\alpha_k/\alpha_{-k}$  [57]. As seen in Figure 2.9, the derived phase model, even for stronger coupling, exhibits a nonlinear relationship between entrainment and forcing strength. This is especially evident along the lower bound of the entrainment range in Figure 2.9A. Although the sinusoidal phase model captures the qualitative entrainment information, it does not capture the types of bifurcations seen in the neural model. In the derived phase model, we see saddle-node bifurcations and Hopf bifurcations in the middle of the lower bound, which is consistent with the entrainment ranges for the neural model. The sinusoidal phase model only loses entrainment through saddle-node bifurcations [57]. Thus, our work justifies using the coupling functions in the derived phase model to approximate the neural model in further entrainment studies, particularly the effects of perturbations.

In both the neural and derived phase models, we chose parameter sets based on previous work [67, 57]. However, the entrainment results of both models approximately scale with the order of magnitude of coupling parameters. This is evident in Figure 2.9. The two panels compare entrainment ranges as a function of forcing position for two parameter sets which differ by a scale of 100. For the derived phase model, plotted in blue, the entrainment range on the right is exactly 100 times the entrainment range on

the left. For the neural model, the entrainment ranges differ slightly in shape but the same change in magnitude is evident. This scaling also occurs in entrainment ranges as a function of forcing position for both models. Thus, our results could be generalized to other models and parameter choices depending on the locomotion system being modeled.

## Chapter 3: **Stochastic Entrainment**

### 3.1 Overview

Proprioception provides information about the position of the body to the CPG, which can then adjust its signal to maintain steady swimming. To better understand the feedback loop for lamprey swimming, we investigate how sensory perturbations affect the entrainment of the CPG. Since sensory feedback is part of a closed-loop system, it is difficult to see causal relationships between edge cell activity and CPG output. In practice, we perform open-loop experiments where a smaller part of the system is isolated and we can control the input and measure the resulting output. To study the effects of sensory perturbations we perform noisy bending experiments where we control the bending of the spinal cord (activating the edge cells) and record the output from the CPG. Perturbations are added to the bending signal, in the form of Gaussian white noise. Thus, through noisy bending we examine how perturbations to sensory feedback affect the entrainment of the lamprey CPG.

Experimental entrainment ranges for deterministic bending signals have been computed while varying the location of the forcing position [66]. Using the same experimental conditions, described in Section 1.1, we compute entrainment ranges while applying noisy sinusoidal bending signals to the excised lamprey spinal cord. The noisy bending signal serves as a perturbation to the edge cells, which then send signals to the CPG. We record

the output from CPG and determine if the CPG is entrained or not. We develop a new measure of entrainment since the noisy bending signal introduces more variability to the system and we can no longer expect to have constant frequency for the CPG. Experimental entrainment ranges are computed for caudal bending at the end of the spinal cord for various levels of noise.

We then model these experiments using the derived phase model defined in Section 2.3, which in the limit of weak coupling captures the same entrainment information as the neural model for deterministic bending. We now add stochastic bending to the derived phase model and compute the entrainment range for forcing at the end of the chain. We quantify the effects of the noisy bending on entrainment by calculating the variability in the phase relationships between oscillators and also in the frequency of oscillations.

### 3.2 Noisy Bending Experiments

To determine how the CPG responds to perturbations we perform noisy bending experiments and record the CPG output. As in the deterministic entrainment experiments, described in Section 1.1, the spinal cord is removed from the lamprey and placed in a bath of excitatory neurotransmitter, D-glutamate, to activate the CPG. The spinal cord is pinned down, with only a few caudal segments free to bend. The most caudal segment is attached to a plastic arm which is controlled by a motor. Glass suction electrodes are placed along the side of the spinal cord and record the output from the ventral root. This is the electrical signal produced by the CPG which would then innervate the muscles for swimming if the lamprey was intact. Figure 3.1A illustrates this experimental set-up where the large arrows indicate the placement of electrodes. Figure 3.1B shows the recordings from the three electrodes shown in Figure 3.1A for a stationary spinal cord

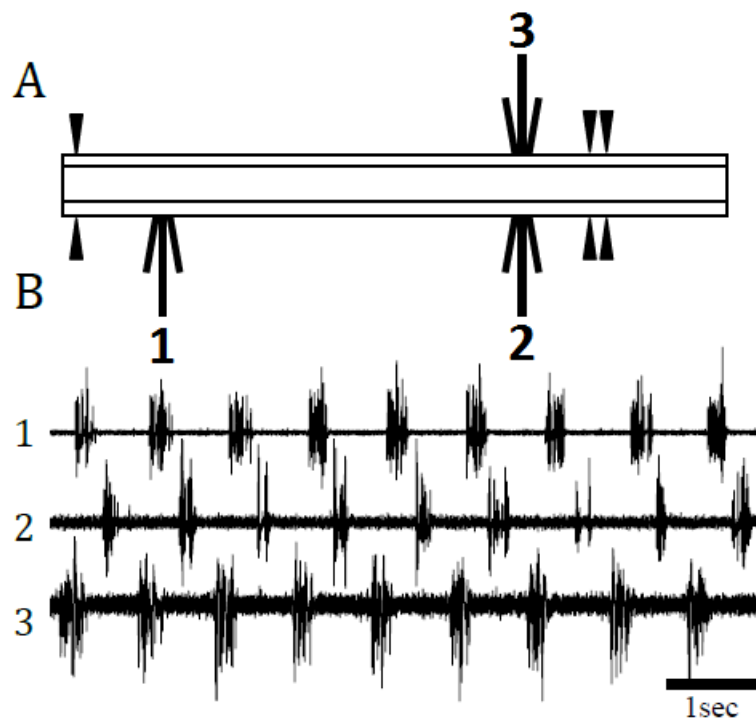


Figure 3.1: Experimental recordings from ventral roots along the excised lamprey spinal cord in a bath of neurotransmitter. Figure A shows the experimental recording configuration. Glass suction electrodes are used to record from ventral roots along the notochord while bending the spinal cord back and forth. The three large arrows indicate three suction electrodes placed at different locations along the spinal cord. The smaller triangles indicate where the spinal cord was pinned down in the bath. The double set of pins to the right of arrows 2 and 3 denote the point of bending. Figure B shows a sample recording of the ventral root signals from segments along the spinal cord at positions indicated by the arrows in A for a stationary spinal cord without bending.

without bending. Thus, the recordings show the intrinsic firing frequency of the CPG. To compute the firing frequency, we determine the time between the center of two bursts, which is the period of signal. We denote this period by  $T_0$  and the intrinsic frequency of the CPG by  $\omega_0 = 1/T_0$ . Note there is a phase lag between the bursts in recordings one and two which corresponds to the traveling wave of electrical activity along the spinal cord. Additionally, the bursts in recordings 2 and 3, electrodes on opposite sides of the spinal cord, occur in antiphase, illustrating the alternation of activation on the left and right sides.

Using sinusoidal bending signals with various frequencies we compute a deterministic entrainment range, the range of frequencies for which the CPG is entrained. In Figure 3.4B the black line illustrates the deterministic entrainment range for sinusoidal bending (no noise) with amplitude 20 degrees and various frequencies close to the CPG's intrinsic frequency,  $f_0$  Hz. Entrainment is determined by the burst frequency, corresponding to action potentials in the recordings. When the CPG is entrained, these bursts occur with the same frequency as the sinusoidal bending signal. An example of this deterministic bending data is shown in Figures 3.2A-C. The deterministic bending signal is shown in Figure 3.2A and is overlaid with the raw recording from electrode 3. Figure 3.2B plots the burst frequency for each recording as a function of bending cycle number. The frequency of each burst is close to the frequency of the sinusoidal bending signal, indicating that the CPG is entrained. Another way to visualize entrainment is to look at the phase of the bending signal where spikes (action potentials) in the recording occur. This is computed by multiplying the frequency of the bending signal by the spike times. If the CPG is entrained, then spike times should be clustered around a single phase. This indicates that the CPG is firing at an approximately constant phase relative to the bending signal.

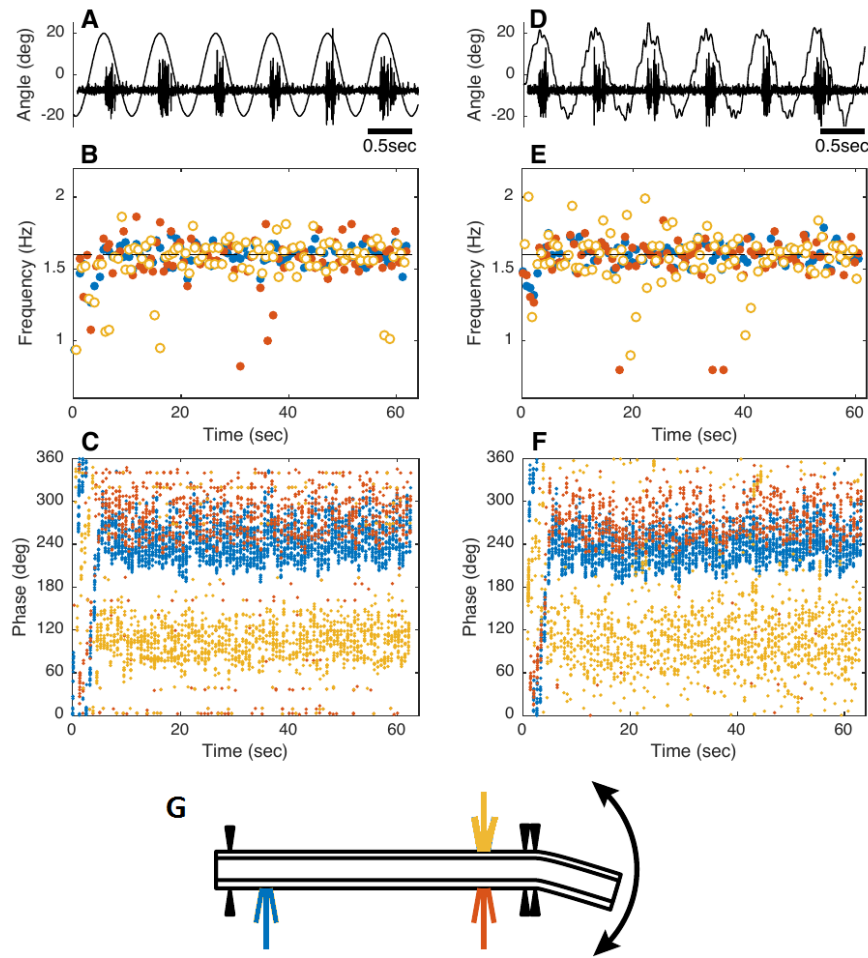


Figure 3.2: Comparison of experimental data from one section of the spinal cord with a deterministic sinusoidal forcing signal (A-C) and noisy sinusoidal forcing (D-F) applied to the last segment. Figures A, D show the relationship of the sinusoidal bending to the ventral root recording. Figures B, E show that the oscillators have entrained to the 1.6 Hz forcing frequency. Figures C, F show the phase of the spikes relative to the forcing frequency. The noisy bending produces figures very similar to deterministic bending, indicating the lamprey CPG is robust to noise.

Thus, the CPG and the bending signal have the same frequency, which is entrainment. Figure 3.2C shows the spike phases for the three different ventral root recordings where each color denotes a different electrode. Spikes recorded in electrode 1 occur around  $240^\circ$  and spikes recorded by electrodes 2 and 3 occur around  $120^\circ$  and  $300^\circ$  respectively where the degrees measure the phase in the sinusoidal bending signal. Note that even when the CPG is entrained to the sinusoidal bending frequency there is still variability in the spike phases. This is due to intrinsic variability in neuron firing and also likely due to noise from the extracellular recording.

We now have a baseline entrainment measure for deterministic sinusoidal bending. However, smooth sinusoidal bending is not realistic sensory input to the lamprey CPG. Lampreys experience perturbations during swimming which can be internal: variability in neuron firing; or external: changes in the environment such as wakes, obstacles or other lamprey. Proprioception plays a large role in the lampreys' ability to adjust its behavior in response to these perturbations. To test how the CPG responds to perturbations, we add Gaussian low-pass filtered white noise to a sinusoidal bending signal, which would typically entrain the CPG. To quantify the level of noise added to the sinusoidal signal, we compute the signal to noise ratio (SNR). SNR is equal to the amplitude of the sinusoidal bending signal divided by the amplitude or standard deviation of the noise signal. For example, for a bending signal consisting of a sinusoid with amplitude 20 degrees and filtered Gaussian white noise with standard deviation 4 degrees the resulting SNR is  $20/4 = 5$ . An example of one such noisy bending signal is shown in Figure 3.2D along with a single electrode recording from the CPG. Figures 3.2D-F summarize the CPG output for noisy sinusoidal bending with the same frequency of bending as in Figures 3.2A-C. Note that the burst frequencies shown in Figure 3.2E are still clustered around the underlying bending

frequency of 1.6 Hz. This implies that the CPG is still bursting at the same frequency as the bending signal which means the CPG is still entrained in the presence of noise. In Figure 3.2F we see the relative phases of spike times in each recording. Note that the spike phases for electrodes 2 (red) and 3 (yellow) are more loosely distributed than the spike phases for electrode 1 (blue). This is likely because electrodes 2 and 3 are located closer to the point of bending than electrode 1, as seen in Figure 3.1A. Thus, the effects of bending are seen more strongly in segments closer to the point of bending. This implies that the short ascending connections are stronger than the long ascending connections. Despite the increased variability in the spike phases the average spike phase still agrees with the average spike phase for deterministic bending show in Figure 3.2C. Thus, the phase relationship between segments is maintained and the CPG is entrained with noisy bending. This suggests that small perturbations to the sensory feedback received by the CPG during swimming do not disrupt the neural activity for steady swimming.

### 3.3 Modeling Noisy Bending Experiments

To investigate the experimental entrainment ranges for deterministic sinusoidal bending [66], several CPG models have been analyzed [57, 47]. These models, with certain types of coupling, were able to capture the qualitative properties of entrainment seen in the experimental lamprey data. We now model the noisy bending experiments with the derived phase model presented in Section 2.3. To model the noisy sinusoidal bending, we add filtered Gaussian white noise to the forcing connection in (2.7). The equation of the forced oscillator,  $\theta_m$ , becomes

$$\dot{\theta}_m = 2\pi f_0 + \sum_{\substack{k=1 \\ k \neq m}}^n \sum_{j=1}^6 \sum_{l=1}^6 \alpha_{m-k}^{lj} H^{lj}(\theta_k - \theta_m) + \alpha_f \sum_{s=1}^2 \sum_{j=1}^6 H_f^{sj}(\theta_f - \theta_m) + \sigma \xi \quad (3.1)$$

where  $\xi$  is the filtered Gaussian noise and  $\sigma$  denotes the standard deviation of the noise. For simplicity, we refer to  $\sigma$  as the level or amplitude of noise in the SNR calculation. For a complete description of the derived phase model and its parameters see Section 2.3. For the simulations in this chapter we use strong nonuniform coupling asymmetry for inter-segmental connections. Recall that these parameters yielded non-monotonic entrainment ranges a function of forcing position, which more closely matched experimental entrainment ranges. The specific parameters we use here are  $A_a = 0.6$ ,  $A_d = 0.04$ ,  $\lambda_a = 0.75$ , and  $\lambda_d = 4$ , which define coupling strength based on length in (2.8).

To model the noisy bending experiments, a chain of coupled phase oscillators was simulated under the same conditions as the biological experiments. Mathematically, the relative phase of the oscillators is computed by  $\theta_f - \theta_i$ . With smooth sinusoidal forcing, constant relative phases indicate the CPG is entrained. That is, the oscillators in the chain all have the same frequency as the forcer  $\theta_f$ . For sinusoidal forcing with low-pass filtered Gaussian white noise, represented in our model by the last term in (3.1), the relative phases will not be constant because of the noise added to the forcing. Figure 3.3 compares the simulations with deterministic and stochastic sinusoidal bending. Figure 3.3A illustrates the deterministic sinusoidal forcing signal. For a set range of frequencies, this signal will entrain the computational CPG with  $\alpha_f = 3$ . Figures 3.3B and 3.3C illustrate the entrainment of the CPG. In Figure 3.3B, the frequency is plotted for the entire length of the simulation for oscillators 9 and 10. Since the CPG is entrained, the frequency of both oscillators is the same as the forcing frequency (and is the same for all oscillators in the chain). When all the oscillators have the same frequency, the phases of the oscillators relative to the forcing signal will be constant as seen in Figure 3.3C.

We use the same types of plots for the stochastic sinusoidal forcing to determine the

effects of perturbations on entrainment. Figure 3.3E shows the noisy sinusoidal bending signal for our simulation, Figure 3.3G plots the frequency of oscillators 9 and 10, and Figure 3.3F shows the relative phase of oscillators 4, 8, 9 and 10 in the chain as a function of time. The computational CPG still appears entrained to the forcing frequency  $f$  despite the addition of noise. Figure 3.3G shows that the cycle frequency for oscillator 9 matches almost exactly with the forcer while the frequency of oscillator 10 varies around  $f$ . Thus, the noisy forcing signal has a noticeable impact on the tenth oscillator where the forcing is applied but not on the rest of the chain. Figure 3.3F shows the relative phases appear mostly constant with small oscillations around the relative phase that would have been seen without noisy forcing, depicted in Figure 3.3B. The relative phases also illustrate that the phase lag between segments is maintained throughout the simulation. More importantly, the simulations show that the noisy forcing on the tenth oscillator is reflected in the plot of its relative phase, but the noise drastically decreases in even the ninth oscillator. This is also seen in Figure 3.3H where forcing is applied to the 5th oscillator. Note the relative phases for oscillators above 5 ( $i < 5$ ) appear more variable than oscillators below 5 ( $i > 5$ ). Despite the addition of noise, the relative phases still approach the same average relative phase seen in Figure 3.3D. Thus, the perturbations added to the model have added variability to the CPG output but not disrupted the signal enough to prevent entrainment.

### 3.4 Stochastic Entrainment Ranges

So far we have described experimental results for noisy sinusoidal bending in Section 3.2 and computational modeling of noisy sinusoidal bending in Section 3.3. However, these are only two illustrative examples of the CPG remaining entrained to the underlying sinusoidal bending signal in the presence of noise. To summarize the effects of noise across

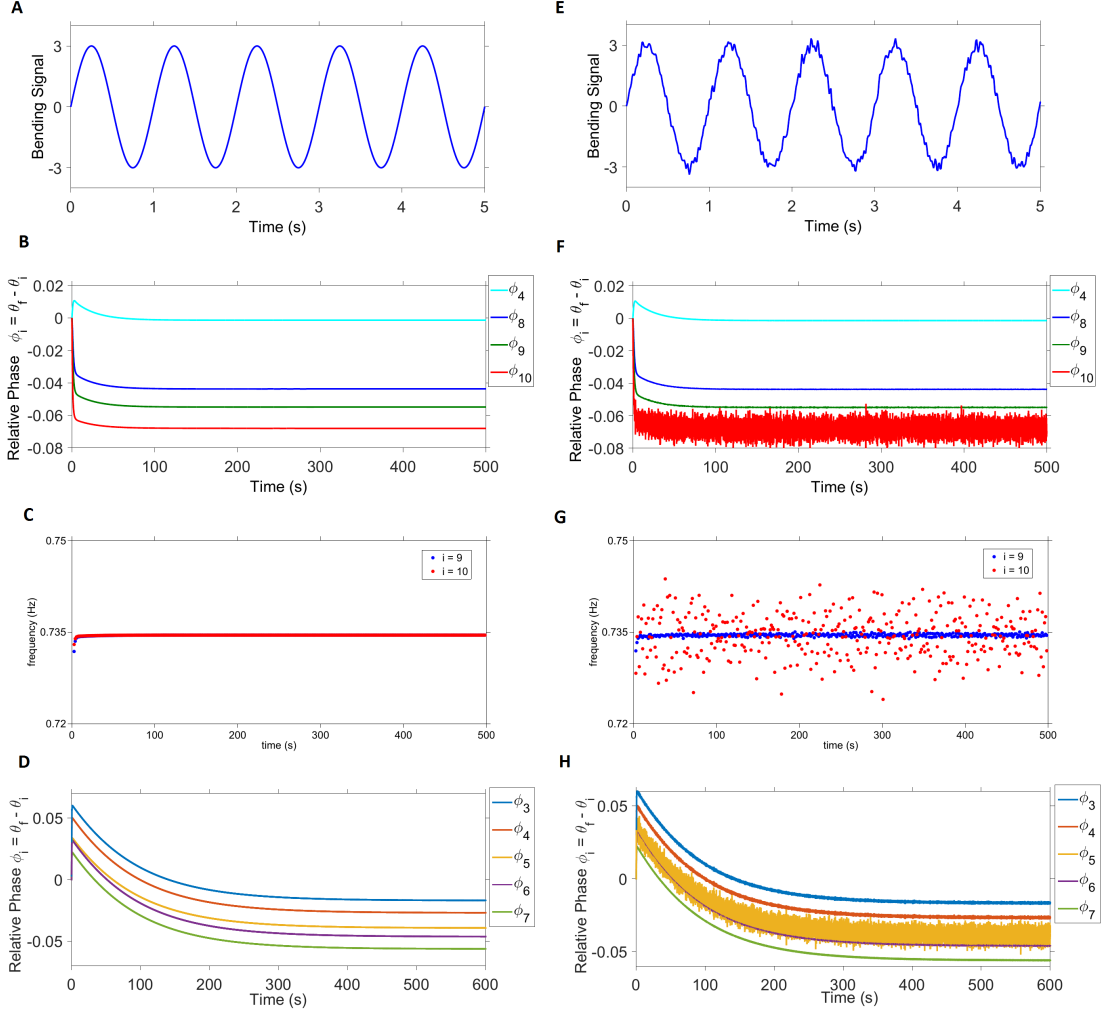


Figure 3.3: Simulation of the derived phase model with sinusoidal (A-D) and noisy sinusoidal (E-H) forcing. Figure A shows the sinusoidal forcing signal applied to the tenth oscillator. Figure B shows the relative phases of several oscillators with sinusoidal forcing for  $m = 10$  where  $f - f_0 = 0.0005$  and Figure D shows the relative phases for oscillators 3 through 7 when  $m = 5$ . Figure C plots the frequency for oscillators 9 and 10 during the entire bending signal. Figure E illustrates the noisy sinusoidal forcing signal applied to the  $m$ th oscillator. Figure F shows the relative phases of oscillators 4, 8, 9, and 10 with  $f - f_0 = 0.0005$ , forcing strength  $\alpha_f = 3$  and noise level  $\sigma = 0.15$ . Figure G plots the frequency for oscillators 9 and 10 throughout the entire bending signal for  $m = 10$ . Note that the noise is clearly visible in oscillator 10, where forcing is applied, but the amplitude of the noise is dramatically decreased in oscillator 9. Figure H plots the relative phases of oscillators 3 through 7 when  $m = 5$ .

a range of bending frequencies, we compute entrainment ranges for both the experimental bending data and the computational CPG model. For deterministic sinusoidal bending, entrainment corresponds to constant relative phases. For the stochastically forced CPG, both the experimental and computational CPG signal will be more variable due to the noisy signal. Thus, to characterize entrainment for noisy sinusoidal bending, we calculate the mean and variance for the spike phase. Since our data is periodic and variable, we need to use circular statistics [18]. For spike phases,  $x_i$ , the circular mean is computed by the following

$$\bar{x} = \frac{1}{n} \sum_{i=1}^n \begin{pmatrix} \sin(2\pi x_i) \\ \cos(2\pi x_i) \end{pmatrix} \quad (3.2)$$

$$\bar{\theta} = \arctan(\bar{x}) \quad (3.3)$$

where  $\bar{x}$  is the resultant vector and  $\bar{\theta}$  denotes the average phase of the data. To measure the variability we take

$$R = \|\bar{x}\| \quad (3.4)$$

$$S = 1 - R \quad (3.5)$$

where  $S$  denotes the circular variance of the data. An  $R$  value closer to 1 means that there is a tight distribution of spike phases ( $S$  close to 0) and indicates that the spinal cord is entrained. A smaller value of  $R$  indicates there is more variability in the phases when the spikes occur, which implies the CPG is not entrained.

Figure 3.4 shows the R-statistic plotted as a function of the entrainment range  $f - f_0$  for different values of the signal to noise ratio (SNR). SNR is calculated by dividing the amplitude of the sinusoidal bending signal by the standard deviation of the Gaussian band-limited white noise which is added to the signal. Figure 3.4A plots a sample recording

with noisy sinusoidal bending with SNR 10. Figure 3.4B shows values of the R-statistic as a function of forcing frequency obtained experimentally. Figure 3.4C shows the same plot using simulation of the derived phase model of the CPG with noisy sinusoidal forcing. In Figure 3.4B, the R values are close to 1 for several SNRs when the forcing frequency is close to CPG's base frequency. However, as  $|f - f_0|$  gets larger, the noise has more affect on the CPG signal and the R value decreases. For the computational model, the R-statistic is high for all levels of noise when  $f - f_0$  lies in the deterministic entrainment range, but outside of this range the R-statistic decreases. This is illustrated in Figure 3.4C. Thus, when the computational CPG is entrained, it is highly robust to noise added to the forcing signal. Figure 3.4 illustrates that the lamprey CPG is highly resistant to noise, with no effect observed until the signal to noise ratio is close to 1. The effects of noise are more subtle in the computational model in the sense that the noise is mostly seen in the oscillator where the noisy bending occurs, seen in Figure 3.3F in oscillator 10. Also, the entrainment range for the derived phase model is much smaller (an order of magnitude less) than the experimental entrainment range. This is due to the assumptions of our model and our choice of coupling strength. In the derived phase model, entrainment ranges scale with the coupling strength. For example, if the intersegmental coupling was ten times stronger, the entrainment range would be ten times larger. Thus, the derived phase model closely agrees with the entrainment results of noisy bending experiments and can then be used to explore other properties of sensory feedback.

### 3.5 Discussion

In our deterministic bending simulations for lamprey CPG models, entrainment is measured by comparing the frequency of each oscillator in the chain,  $\omega_i^*$ , to the angular

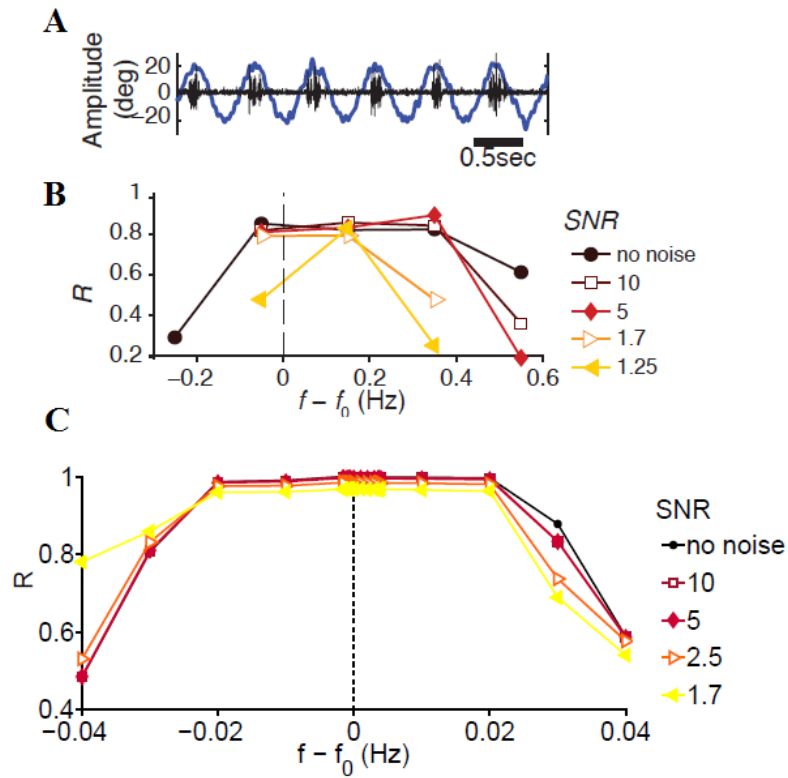


Figure 3.4: Experimental and computational results indicate that the CPG is highly robust to noise. Figure A shows a sample recording showing entrainment of the CPG activity (black) to a noisy bending signal (blue) with SNR of 10. Figures B and C show the experimental (B) and computational (C) entrainment results for signals with a range of SNR values.  $R$  is the resultant vector length;  $R > 0.8$  indicates entrainment.

forcing frequency  $\omega_f = 2\pi f$  where  $f$  is the frequency in Hz. If the frequency of each oscillator is the same as  $\omega_f$  then we say the chain is entrained. However, for stochastic bending simulations, we are introducing noise to the system. Thus, we do not expect the oscillators to maintain a constant frequency but rather a variable frequency close to  $\omega_f$ . This then implies the relative phase of each oscillator,  $\theta_f - \theta_i$  will not longer be constant but instead will vary around the constant phase seen for deterministic bending. To visualize the effect of the added noise on the entrainment of the CPG we plotted burst frequencies and relative spike phases. Figures 3.2 and 3.3 compare the burst frequency and relative phases for experimental data and model simulations. From these comparisons, it appears the CPG is robust to noise during entrainment. In both the computational model and the experimental data, the burst frequency remains close to the forcing frequency  $f$ . To further quantify these results, we computed entrainment ranges as the signal to noise ratio increased. We define entrainment for noisy sinusoidal bending with the R-statistic, where values above 0.8 indicate entrainment. Entrainment ranges for both experimental data and the derived phase model show that entrainment is mostly unaffected across a range of SNRs when the forcing frequency is in the deterministic entrainment range. The R-statistic only begins to drop below 0.8 when the forcing frequency is much different than the base frequency (ie.  $|f - f_0|$  is large) and the SNR gets close to 1. Both our experimental data and our computational model indicate the CPG is highly robust to noisy sinusoidal bending in terms of maintaining entrainment.

For this model, we chose a specific type of intersegmental coupling, namely nonuniform coupling asymmetry. This means that we choose ascending and descending coupling strengths so that for some connection lengths, ascending connections are stronger than descending ones, but for other lengths, ascending connections are weaker than descending.

Previously, we [47] computed deterministic entrainment ranges for both the neural model (2.1) and the derived phase model (2.7). The models best captured the qualitative properties of entrainment from experimental data when nonuniform coupling asymmetry was used [47]. The derived phase model, with relatively strong nonuniform coupling asymmetry, also captures the stochastic bending results presented here. This further validates our model and supports our claim that the lamprey CPG exhibits nonuniform coupling asymmetry for intersegmental connection strengths. One limitation of our model is that we assume edge cell inputs only affect a single segment. Anatomically, we know that edge cell axons may extend over multiple segments, with their axons going primarily rostrally (towards the head) [62]. Functionally, however, we do not know how strong or the exact length of these long connections are. We further examine the role of edge cells in Chapter 4.

The differences between the deterministic and stochastic output illuminate how the edge cells affect the CPG signal and how entrainment is achieved. For forcing at the end of the chain, we saw our model closely resembled the experimental entrainment results for stochastic bending (Figure 3.4). In the derived phase model, we can easily vary where the forcing is applied in the chain. An interesting result from the noisy bending simulations arose from forcing the chain at the middle oscillator  $\theta_5$ . We saw the noise from the forcing signal had a larger effect on oscillators above  $\theta_5$  and a smaller effect on the oscillators below. This result is especially interesting because we choose nonuniform coupling strengths, defined in (2.8), which means that short ascending connections are stronger than short descending connections but for longer connections the descending strengths are larger. Thus, the short connections may determine how much influence the sensory information from the edge cells has on the other oscillators in the chain. This

result is supported by the relative phases from the experimental recordings plotted in Figures 3.2C and 3.2F where the relative spike phases are compared for deterministic and noisy bending. Electrode 1 is farther away from the point of bending than electrodes 2 and 3 and the distribution of spikes in Figure 3.2F for electrode 1 appear less variable. Note all of the recordings are above the point of bending so we cannot compare the effects of noisy bending on oscillators above and below the segment where forcing is applied. Thus, our model gives insight into how differences could arise based on differences intersegmental connection strengths. These modeling results are important because it is difficult to measure individual connection strengths experimentally. We also see that when noisy bending is applied to the 10th oscillator in the chain, the noise is greatly reduced in the rest of the oscillators as seen in the relative phase of oscillator 9 in Figure 3.3F. These results illustrate how noisy input into the CPG is filtered before it propagates to other segments in the spinal cord.

Our stochastic entrainment analysis characterizes the effects of noisy sinusoidal bending on the phase and frequency of CPG output but does not describe how sensory perturbations change the CPG output. An alternative approach uses a harmonic transfer function (HTF), which fully characterizes the effects of small perturbations of a stable periodic system in the frequency domain. In our case, the periodic system corresponds to sinusoidal bending that entrains the CPG's rhythm and the perturbations are the noise added to bending. An HTF is an extension of the frequency response function (FRF), which fully characterizes small perturbations around a stable fixed point in the frequency domain. The FRF describes how sinusoidal input at any frequency  $f$  produces sinusoidal output at the same frequency, specifically it describes how gain (the ratio of output amplitude divided by input amplitude) and phase (the phase shift of the output relative to

the input) vary across frequency. We compute FRFs and HTFs for noisy bending and edge cell output in Chapter 5.

## Chapter 4: **Role of Edge Cells During Entrainment**

### 4.1 Overview

Edge cells are mechanosensory neurons located in the margin of the spinal cord that respond to the stretch of the spinal cord [23, 58, 33]. As lamprey swim, an S-shaped wave propagates down the body resulting in propulsion of the animal through the water. Edge cells facilitate this wave by detecting stretch and rate of stretch and sending electrical signals to the CPG. Thus, edge cells are studied as one of the primary forms of sensory feedback in the lamprey. Sensory feedback plays a large role in adjusting the phase lag between segments and thus contributes to the entrainment of the CPG. We wish to identify the role of edge cells during entrainment and describe the input-output relationship between edge cell activation and CPG output. To model this relationship we investigate what type of information is encoded in edge cell firing. We compute firing rates for periods of static and dynamic stretch through bending experiments similar to the CPG bending experiments described in Section 1.1. From these bending experiments we identify different types of edge cells which tend to respond to different bending stimuli and show how firing rate relates to different bending characteristics like amplitude and velocity.

## 4.2 Mechanosensory Neurons

Edge cells are mechanosensory interneurons in the lateral tract of the lamprey spinal cord which are known to detect stretch during swimming [23]. A fluorescent stain can be used to image edge cells in the spinal cord, illustrated in Figure 2.2. Image was taken in Jim Buchanan's lab by Eric Tytell. In the bottom of the figure, the edge cell dendrites synapse on to the edge of the spinal cord. These synapses are activated when the body bends and the spinal cord is stretched. This means that edge cells along the left side of the spinal cord will respond when the body is bent to the right (with respect to the animal) because the left side of the body will be stretched while the right side is compressed. Information about how the body is bent is sent through the edge cell body, down the edge cell axon, and finally to the CPG. Edge cell axons project along the lateral tract of the spinal cord but the exact lengths of the projections is not known. It is known that some edge cell axons run ipsilaterally, while some project contralaterally. These two classes of edge cells act differently on certain classes of neurons in the CPG. Edge cells with ipsilateral projections excite CPG neurons while edge cells with contralateral projections inhibit CPG neurons [58]. Thus, edge cells act as proprioceptors for lamprey and contribute to adjusting the frequency of CPG output in response to perturbations. These perturbations could come from the environment in the form of rocks, currents, or other fish, or internally from the variability of neural firing or muscle force. Sensory feedback allows the CPG to adjust its rhythm and maintain the desired periodic neural activation of muscles used for swimming.

Previous studies have shown that edge cells respond to lateral stretch [23, 58, 33] and dorsal stretch [33]. Hsu et al. [33] also showed that the distribution of edge cells that respond to each bending direction, contralateral or ipsilateral in the yaw plane and dorsal

or ventral in the pitch plane, varies along the length of the spinal cord. Most neurons responded to ventral bending and about 40% responded to contralateral bending. The proportion of edge cells with responses to different bending directions was about the same for the rostral (segments 10 to 30) and middle (segments 35 to 50) regions of the spinal cord. However, there were twice as many neurons that responded to ipsilateral bending in the middle region of the spinal cord. This difference could contribute to the non-monotonic entrainment range seen by Tytell and Cohen [66] where entrainment ranges were largest for bending applied to the middle segments of the spinal cord.

Edge cells are part of a complex, closed-loop locomotion system which involves interactions between many different biological systems. The CPG produces the neural activity which innervates muscles for swimming, which then bends the body and activates edge cells and provide feedback to the CPG. In an effort to understand how edge cells respond during swimming, we perform open-loop experiments where a mechanical stimuli bends the excised spinal cord and activates edge cells. This allows us to provide a known (controlled) input to the edge cells and record the resulting output. Using different bend and hold bending signals, we identify several types of edge cell response which differ based on the amplitude and velocity of bending.

### 4.3 Experimental Methods

Previous experiments have focused on the CPG response to mechanical bending and recordings were from the ventral roots on the notochord. These are the signals that would be sent to activate muscles to produce a swimming motion. To record edge cell responses the initial preparation is very similar to the standard CPG preparation. The spinal cord is excised using the same methods and again pinned in a bath. For edge cell recordings, we

do not want any neurons of the spinal cord to be activated by neurotransmitters because we are looking for responses to mechanical stimuli. Thus, the spinal cord is placed in a bath of calcium-free saline which leaves the neurons in the CPG inactive and also blocks synaptic transmission. For a single experiment, we use a section of spinal cord between 15 and 25 segments long. See Section 1.1 for a complete description of the experimental preparation for the CPG bending experiments. As in the CPG bending experiments, the spinal cord is pinned down and the caudal end is attached to an arm controlled by a motor. We prescribe different types of bending signals which bend the end of the spinal cord and as a result the edge cells are activated. To record the response to bending, as many as three glass suction electrodes are placed in the lateral tract of the spinal cord. Figure 1.1 illustrates the different tracts in the spinal cord. Note these recordings differ from the CPG recordings because the electrodes are placed in the spinal cord as opposed to along the side of the spinal cord where the motor output is recorded. In these experiments, the electrodes record extracellularly in the lateral tract where the edge cell axons run along the length of the spinal cord. Figure 4.1 shows a sample of such recordings in blue. Specifically, the electrodes record changes in membrane potential (mV). Large changes in voltage, positive or negative, can be thought of as action potentials. These action potentials, moving down the edge cell axons, carry information about bending back to the CPG.

#### 4.4 Spike Sorting

Extracellular recordings detect all responses in the immediate area surrounding the tip of the electrode. This implies that we could record several different edge cell axons within a single electrode. Identifying individual axons or responses, known as units, is

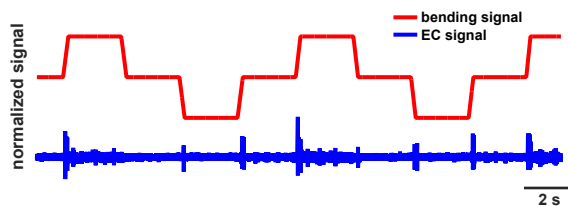


Figure 4.1: Normalized ramp bending and raw edge cell recording. Note there are different units that respond during different portions of bending. Large spikes occur during active periods of bending and smaller spikes occur during hold times with positive bending angle.

difficult in some cases. However, from visual observation of the data, it is clear that there are different sized spikes that respond consistently during different portions of the bending signal. An example of this can be seen in Figure 4.1 where larger spikes occur during active periods of bending to the left or the right and smaller spikes occur during times of static stretch with positive bending angle. While in this example we can see the differences between the two types of spikes, we cannot see the difference between the spikes that occur during positive bending velocity or negative bending velocity. We know that edge cells can either respond to contralateral stretch or ipsilateral stretch but not both. Thus, we need a method to determine the different units within these responses to bending velocity. The standard spike sorting procedure uses principal component analysis (PCA) to determine key features of spike shapes and group similar spikes (see [43] for a review of spike sorting and PCA). To perform this sorting we use software called DataView developed by W. J. Heitler [30]. After identifying spike times based on a selected threshold, spikes are clustered together based on features such as spike width, spike height, spike maximum, and spike minimum. These features are each represented in orthogonal basis vectors and the components of interest are those with the most variability. The variability in spike features can then be used to group spikes into units with similar features. Contrarily, if a

feature has small variability among the data then it can be omitted from the description of the data set without a loss of information. The three components with the most variability (ie. the most information about the spike shapes) then can be used to sort the spike shapes. An example of these clusters plotted in the three principal component basis from DataView is shown in Figure 4.4. In Figure 4.4A all of the spike waveforms that were sorted into the same category and the red line denotes the average waveform of all of the spikes. The dashed line indicates where the spikes were aligned at the peak of their waveform. The two blue vertical lines denote the start and stop time for the waveform. The duration of the spike is typically between 1 and 2 ms. Figure 4.4B illustrates the clusters of different units found in a single recording based on PCA. Each color represents a possible unit. The three dimensions in the plot represent the first three principal components that were used to sort spikes. Note the blue, red, and cyan clusters are tightly distributed which means spikes in those categories had very similar waveform features and belong to the same unit. However, the green and pink clusters are not tightly grouped and could be due to noise in the recordings or overlapping spikes that were misidentified.

#### 4.5 Response to Bending Angle and Bending Velocity

Once spikes are sorted into units with different waveform features, we quantify each unit's response to bending by computing firing rates for different portions of the bending signal. To compare responses to bending angle and bending velocity on each side of the body we split the bending signal into six different phases, illustrated in Figure 4.4. We use the convention that bending to the right has positive bending angle since this will cause an increase of stretch on the left side of the body where the recording site is. Thus, bending with positive bending angle and positive velocity should excite edge cells with

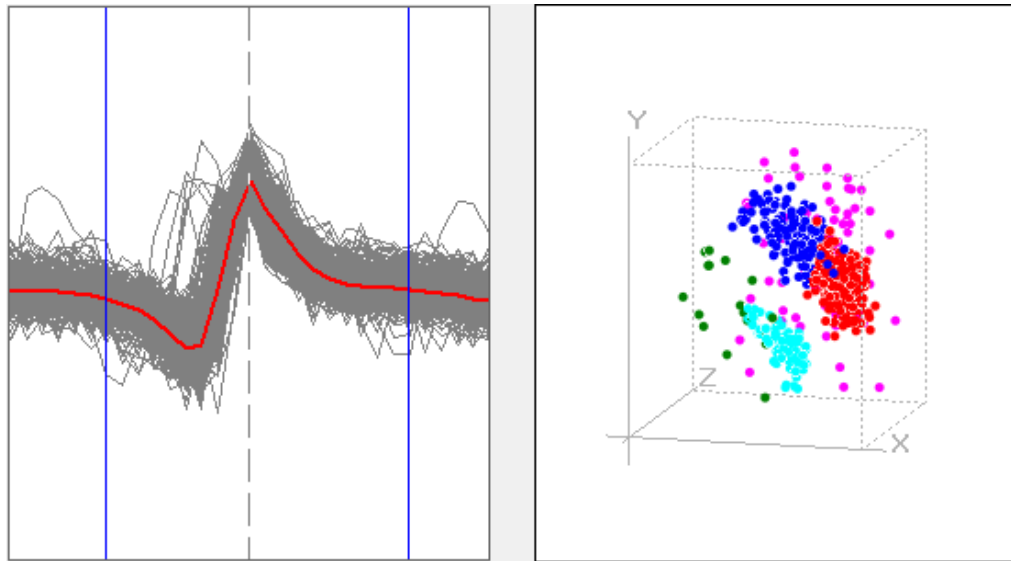


Figure 4.2: Example of DataView spike sorting. A) All spike waveforms for a single unit are shown in gray. The red line denotes the average waveform over all the spikes classified into that unit. B) Clusters used to identify separate units within the recording. Different colors represent different types of units with similar spike shapes. The three dimensions of the plot represent three of the principal components used to determine different types of spikes based on features of their waveform.

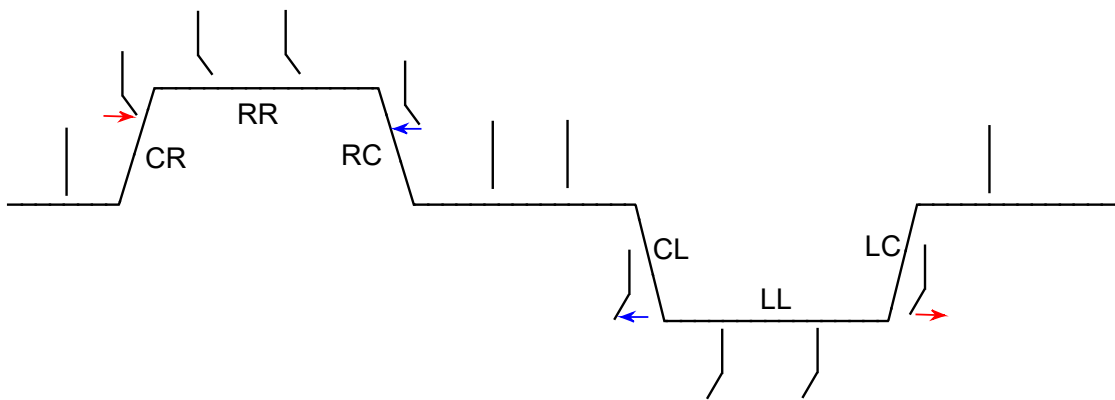


Figure 4.3: For preliminary analysis, the ramps were broken up into six phases where spike rate was computed. This figure illustrates the three different phases: the swing outwards, the hold, and the return swing. Note that ramps can be applied to both sides of the body so in total there are 6 distinct phases to compare.

ipsilateral projections (ie. axons on the same side as the recording site). The ramp phases are named for the beginning and ending position of the spinal cord during that particular phase of bending. In Figure 4.4 the spinal cord starts at center and bends to the right so we name the first phase CR which represents bending with positive velocity and increasing bending angle. The spinal cord then remains bend out to the right for the second phase, named RR. The spinal cord then returns to center, bending with negative velocity, and we name this phase RC. These three phases are then repeated for bending to the left side of the body, towards the recording site. Bending from center to the left represents negative bending velocity and we name this phase CL. The spinal cord is then held to the left for phase LL. Finally, the spinal cord returns to center, now bending with positive velocity, for phase LC. These six phases represent the different combinations of signed bending angle and bending velocity.

To quantify the response of each unit we compute the spike rate for each ramp phase. Spike rates are computed by dividing the number of spikes by the amount of time between the beginning of the ramp phase and the time of the last spike in that phase. This allows us to compare spike rates for ramp phases with different durations. Once we have computed spike rates for each ramp in the recordings we plot spike rate as a function of bending angle for phases LL and RR and as a function of bending velocity for phases CL, LC, CR, and RC. Linear regression is used to fit the spike rates for each ramp phase. Figure 4.4 illustrates spike rates computed for six units, one for each phase of bending. From these plots we see there is variability in spike rate for each bending angle and bending velocity. This is because we repeat different combinations of angles and velocities for each preparation. However, for these responses we see a clear linear increase in spike rate as the ramps get larger in amplitude, Figure 4.4(a), or faster in velocity, Figures 4.4(b) and

(c). Note that spike rates are typically larger in response to bending velocity, Figures 4.4(b) and (c), than bending angle, Figure 4.4(a). This indicates that edge cells fire more in response to changes in position as opposed to measuring the amount of bending that occurs. In addition to units that respond linearly to bending angle and velocity, we also found units that simply detect bending velocity. That is, the unit fires the same number of spikes regardless of the ramp angle or bending velocity. An example of such a unit can be seen in Figure 4.4(b) for phase CR. The majority of the spike rates for this unit range from 0 to 50 spikes/sec for the entire range of bending velocities. Thus, velocity detector units signal to the CPG that bending has occurred but does not convey any information about how much or how fast the body has bent.

In addition to computing spike rates for each ramp repetition, we also compute the average spike rate for each phase. To determine if the unit has a significant average spike rate, we use permutation testing to randomly compute average spike rates for all of the data for that particular unit. If the true average spike rate is greater than the random averages, we say the unit has a significant average response for that particular phase. This means that the unit fires more in response to a particular phase of bending than the others. We perform similar tests to determine if the slope of the linear regression trend line is significant. A summary of all the significant responses for each unit is shown in Figure 4.5. Gray blocks indicate that the unit did not have a significant firing rate, or did not fire significantly more during that particular phase than at any other time. Black blocks indicate that the unit had a significant average spike rate for the phase of bending. Blue blocks indicate that in addition to a significant average spike rate, there was also a significant linear increase in the spike rate during that phase of bending. Units that responded with significant average firing rate but did not have a significant linear

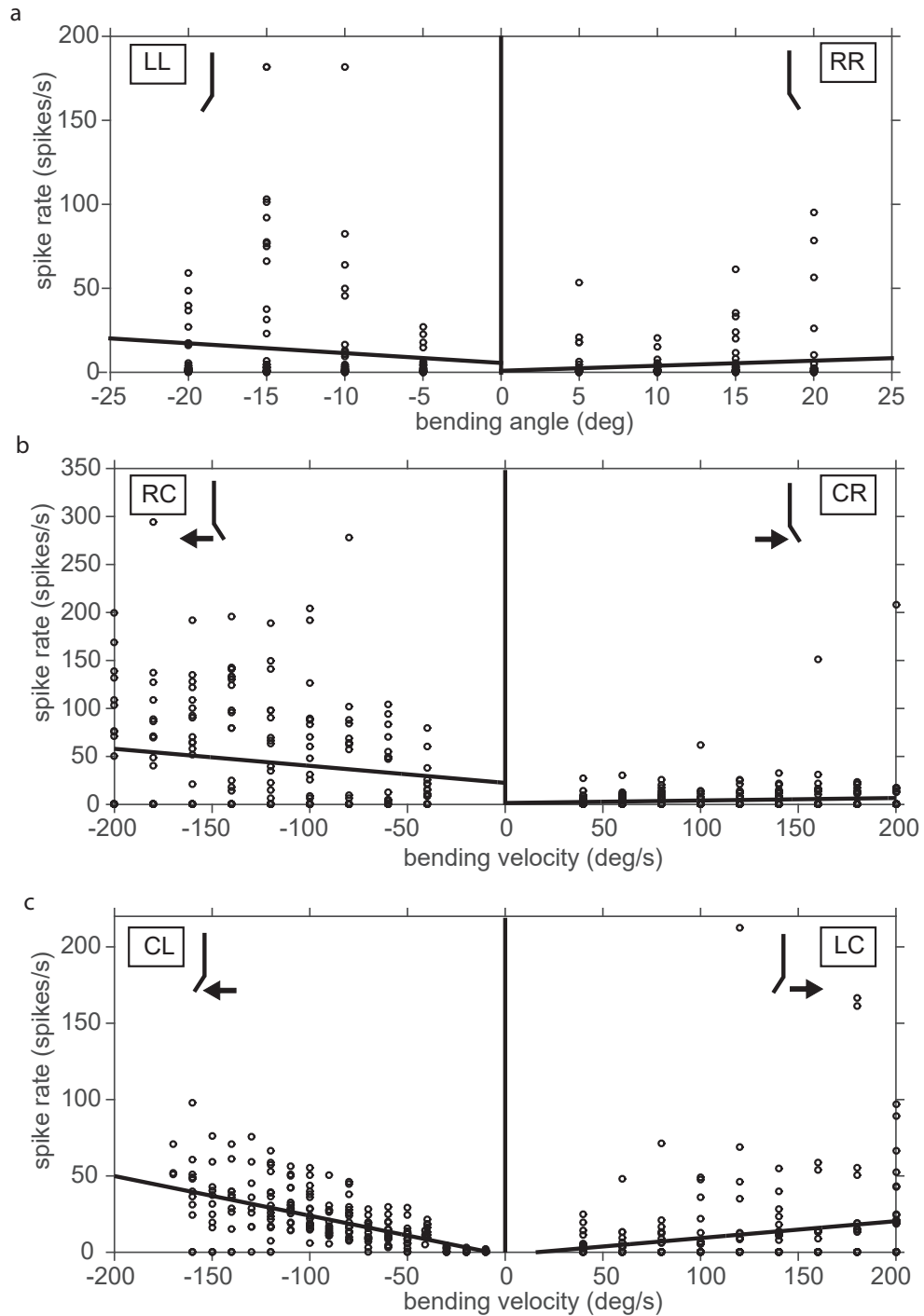


Figure 4.4: Examples of units with significant spike rates for the six phases of ramp bending. Each data point represents a spike rate for a single ramp. The trend line was found using linear regression. Figure 4.4(a) shows spike rate as a function of bending angle for spikes that occurred while the spinal cord was held to one side. Figures 4.4(b) and (c) show spike rate as a function of bending velocity for ramps to the right and left side of the body respectively.

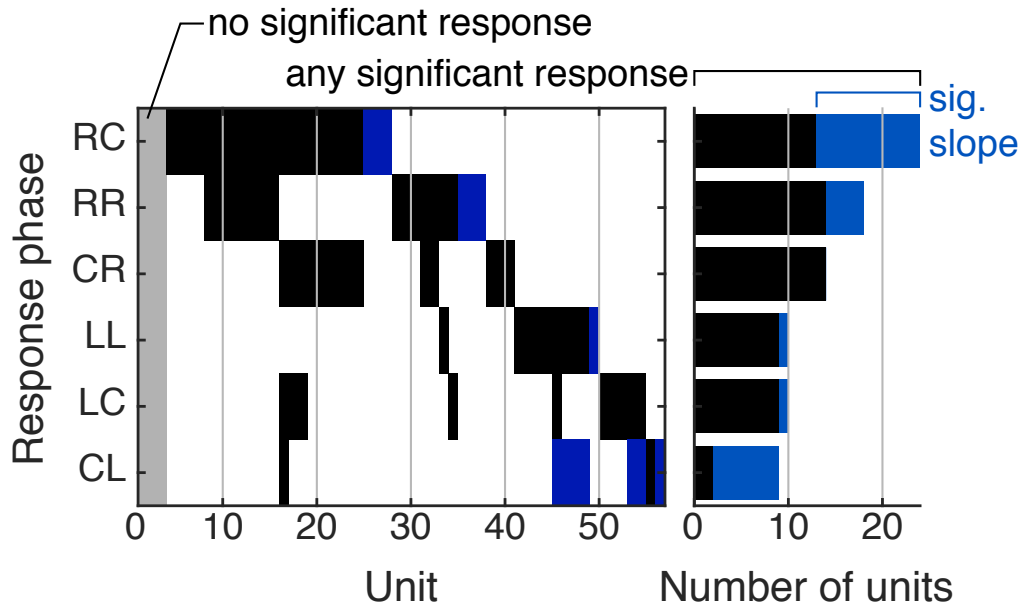


Figure 4.5: Significant responses for each unit. Gray blocks indicate the units that had no significant responses to bending. Black blocks indicate the unit has a significant average spike rate for that particular phase. Blue blocks indicate that the unit had a significant average spike rate and a trend line with significant slope. A count of both types of significant responses for each ramp phase is shown in the histogram on the right.

relationship (black blocks) for phases CR, RC, CL or LC represent velocity detector units. Note these units tended to respond to bending with positive bending velocity (phases CR and LC). From Figure 4.5 we see that most units respond to ipsilateral stretch (bending to the right), which is consistent with previous findings [33].

From Figure 4.5 we see four different types of units: units that respond to bending angle, units that respond to bending velocity, units that respond to both, and units that detect velocity. From visual observation of recordings we also see differences in adaptation. Adaptation refers to a decrease in response during a continually applied stimulus. Thus, for edge cell recordings, we consider adaptation during ramp phases RR and LL where the spinal cord is held to one side. Adaptation is typically classified as fast or slow. Fast adaptation refers to neurons that fire during the beginning of the stimulus but then fire

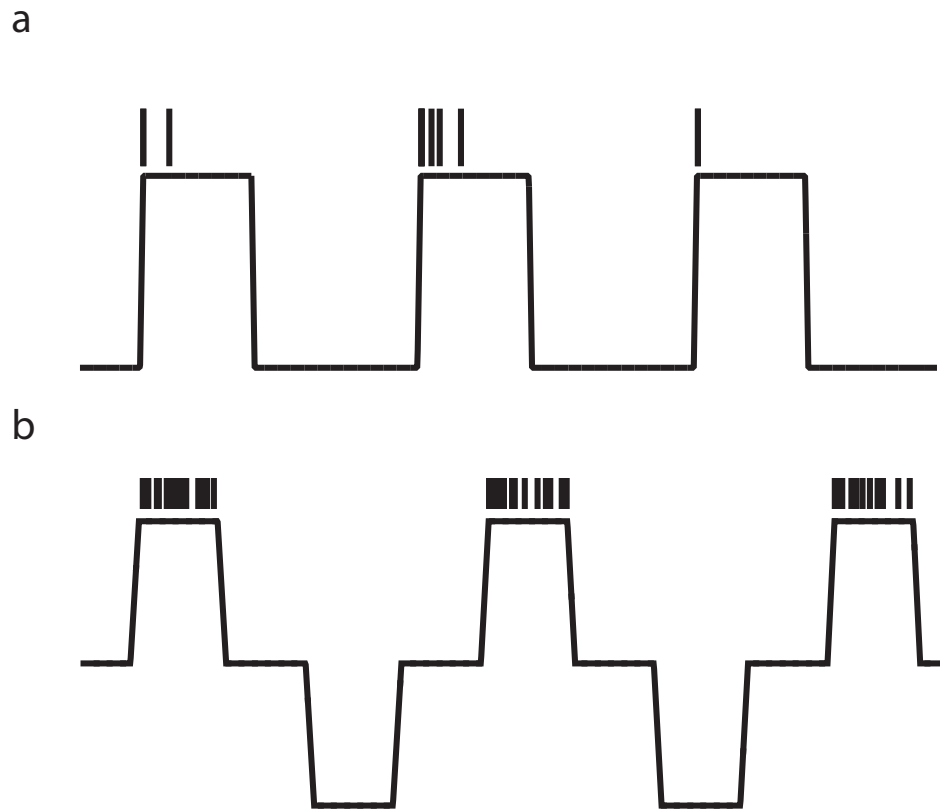


Figure 4.6: Rate of adaptation. Figure 4.6(a) shows the ramp bending signal and a raster of spike times for a fast adapting unit. Spikes only occur at the beginning of the phase. Figure 4.6(b) shows the ramp bending signal and a raster of spike times for a slowly adapting unit. Spikes occur at approximately the same rate for the entire phase.

more slowly or stop firing for the remaining duration of the stimulus. An example of a fast adapting unit is shown in Figure 4.6(a). The unit fires only a few times at the very beginning of the RR phase for each of three ramps to the right. Slow adaptation refers to neurons that fire continually during the entire length of the stimulus at approximately the same rate. An example of a slowly adapting unit is shown in Figure 4.6(b). The unit fires almost regularly during the entire RR phase for each of the three ramps to the right.

To investigate the adaptation properties of the various units found by spike sorting, we approximate firing rates during the RR and LL ramp phases by computing the recipi-

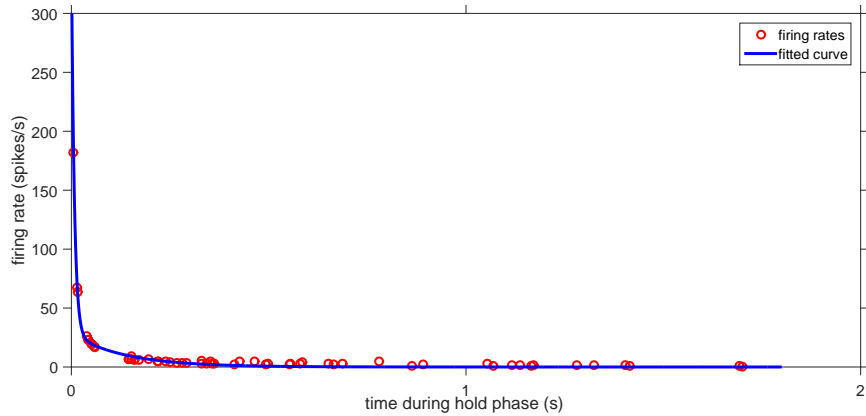
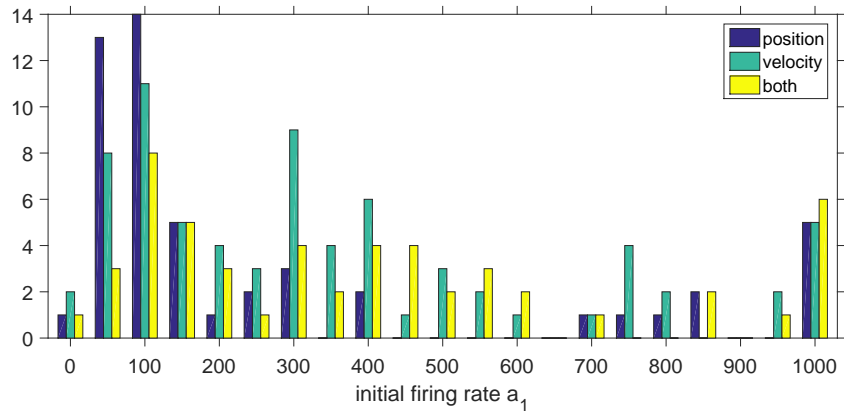
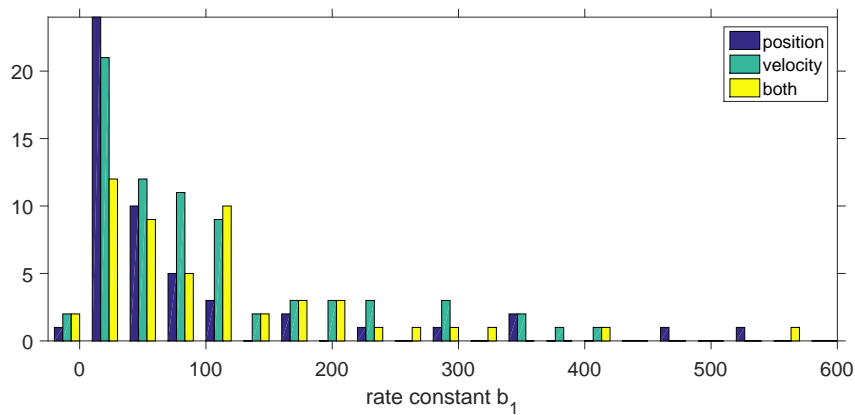


Figure 4.7: Example of a single fit of firing rate as a function of duration of static bending. Firing rates for a unit with significant bending angle response plotted by red circles. Firing rate fit to an exponential curve of the form  $a_1 e^{-b_1 t}$  with  $a_1 = 327.6$ , and  $b_1 = 136.4$ .

cal of interspike times between spikes that occur during the phase and take the reciprocal. This gives us an approximation to the instantaneous firing rate at different times during the ramp phase. We combine the firing rates for all ramps with the same bending angle and fit an exponential curve,  $a_1 e^{-b_1 t}$ , where  $a_1$  represents the initial firing rate and  $b_1$  represents the adaptation rate constant. An example of fitted adaptation is shown in Figure 4.7 for a single unit for a single bending angle. Firing frequencies are plotted by red circle and the fit is plotted in blue. To describe the fast and slow adapting units we summarize all of the fits for each unit in histograms. Figure 4.8 shows the distribution of each of the four fitted parameters. Note the units were separated into three categories based on their significant response phases. Dark blue denotes units that had significant responses to only bending angle (RR or LL), teal denotes units that had significant responses to bending velocity (CR, RC, CL or LC), and yellow denotes units that significant responses to some combination of bending angle and bending velocity. We expect that units that respond to bending velocity will adapt more quickly than those units that respond to position. In Figure 4.8B we see that position responders tend to have smaller adaptation



(a) Initial firing rate.



(b) Adaptation rate constant.

Figure 4.8: Distribution of fitted parameters for 3 types of units with significant position response, significant velocity response, or significant response to both. Firing rate as a function of duration of static bending is fit to  $a_1 e^{-b_1 t}$ . Only significant fits ( $R^2 > 0.5$ ) were included. On average position responders have the slowest adaptation and units that respond to both position and velocity have the fastest adaptation.

rate constants than units that respond to bending velocity. The average rate constants for position, velocity, and combined responders are  $81.9s^{-1}$ ,  $99.5s^{-1}$ , and  $110.1s^{-1}$  respectively. Thus, units that respond to bending position have the smallest rate constant and adapt more slowly while units that respond to both the position and velocity of bending have the largest rate constant and adapt the most quickly.

While ramp bending signals help us determine the encoding properties of bending angle and velocity, it is not the kind of bending stimulus seen by edge cells during swimming. A more realistic activation of edge cells is to apply a sinusoidal bending signal. We have seen that the lamprey CPG can be entrained to bending stimuli at frequencies close to its intrinsic frequency. Entrainment is facilitated by edge cells. By applying sinusoidal bending signals we can determine how edge cells fire during periodic bending of the body as seen in swimming and determine what information is sent to the CPG.

## Chapter 5: **Frequency Domain Analysis**

### 5.1 Overview

It is known that sensory feedback facilitates the entrainment of the lamprey CPG and provides local information about bending (stretch) in the spinal cord during swimming [21, 58, 50]. This feedback is part of the closed-loop locomotion system. Since sensory feedback is part of a closed-loop system it is difficult to determine the causal relationship between sensory feedback and CPG output. One approach is to study components of the closed-loop system with open-loop experimental conditions [61]. Concepts from control theory, system identification and parametric and non-parametric modeling can then be used to relate the open-loop response to the behavior in the closed-loop system [61, 13]. These techniques have been used to study vision and motor control in blowflies [15] and electric fish [14, 45].

To better understand the information encoded by edge cells we perform open-loop bending experiments where we input the bending signal and record the edge cell activity. In Chapter 4 we used ramp bending signals to determine how properties of bending are encoded by edge cell firing. This technique allowed us to determine different types of edge cell responses but does not describe how edge cells respond to perturbation during swimming. Perturbations can move the body which activates mechanosensitive neurons. These neurons, namely edge cells, then synapse onto the CPG and cause a change in

the neural signal which drives locomotion. Thus, after a perturbation is detected the information is processed through several systems before the body movement changes. To completely characterize the edge cell response to bending across a range of frequencies we use a recently developed technique that uses white noise perturbations [34]. This technique gives us a mapping called a phase dependent impulse response function (IRF) which describes how perturbations at each phase affect the output of the system. For edge cell bending experiments, we compute the phase-dependent IRF from bending to edge cell activity. This mapping will help inform the functional form of the feedback from edge cells to the CPG and close the loop in the model for lamprey swimming.

## 5.2 Frequency Response Functions

Since CPG output and edge cell output are part of a closed-loop system, it is difficult to determine how one part of the system affects another. For this reason, perturbations are used to determine how the various parts of the system react to changes to their typical input. Responses to perturbations can then be used to characterize the properties of the input-output map for each stage. For lamprey locomotion, we are interested in how bending affects edge cell output. Edge cells provide mechanosensory input to the CPG as they are activated by the stretching of the spinal cord. Experimentally, we can activate the edge cells with mechanical bending and record the edge cell output. Similarly we can bend the spinal cord and record the CPG output from the ventral roots. On the other hand, it is difficult to measure the effects of the edge cells on the CPG. However, if we can describe the mapping between bending and edge cell output and the mapping between bending and CPG output, then we can separate out the map from edge cell output to the CPG signal. This calculation can be performed in the frequency domain using frequency

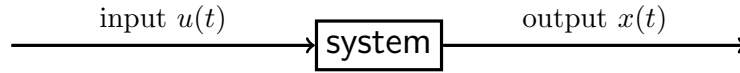


Figure 5.1: Schematic of LTI system with input  $u(t)$  and output  $x(t)$ .

response functions (FRFs) and harmonic transfer functions (HTFs). We now review these maps in the frequency domain and their time domain analogues, and in order to calculate the mappings between bending and edge cell output.

First we consider the input-output relationship for linear time-invariant (LTI) systems. A schematic of the system is illustrated in Figure 5.1. Time invariant means that the output in response to an input at time  $t$  or time  $t+T$  will be the same except for a delay of  $T$  seconds. That is, if the output due to an input  $u(t)$  is  $x(t)$  then the output in response to input  $u(t+T)$  is  $x(t+T)$ . Thus, the response to an input does not depend on when the the input signal is given. An example of an LTI system would be  $\dot{x}(t) = -ax(t) + cu(t)$  where  $a$  and  $c$  are constant. Another important property of LTI systems is the input  $u(t) = \sin(2\pi ft)$  with frequency  $f$  in Hz only gives output  $x(t) = A \sin(2\pi ft + \theta)$  with possible changes to amplitude,  $A$ , and phase shift  $\theta$ . These effects can differ depending on the input frequency  $f$ . Thus, to completely characterize the responses to each input we need to compute a map that describes the amplitude and phase effects for a range of frequencies. This frequency domain map is known as a frequency response function (FRF).

Consider an LTI system with input signal  $u(t)$  and output signal  $x(t)$  as shown in Figure 5.1 with an analytic mapping  $x(t) = u(t)*h(t)$ . To compute the FRF of the analytic system, we first compute the Fourier transform of both the input and output signals, which we denote by  $U(f)$  and  $X(f)$  respectively. Then the output in the frequency domain can be computed by  $X(f) = H(f)U(f)$  where  $H(f)$  is the FRF of the system. Rearranging we

get  $H(f) = X(f)/U(f)$  where the FRF is the component-wise ratio of the output signal and the input signal in the frequency domain. Note  $H(f)$  is a complex-valued function of frequency. To describe the amplitude and phase effects of our system, we compute the gain and phase of the FRF  $H(f)$ . The gain is computed by  $|H(f)| = |X(f)|/|U(f)|$  where the gain measures the ratio of the amplitude of the output and the amplitude of the input. Thus, the gain of  $H$  tells us the resulting change in the output amplitude relative to a given input. We are also interested in phase effects, which we compute by taking the argument of  $H(f)$  so that  $\arg(H(f)) = \arg(X(f)) - \arg(U(f))$ . Thus, the argument of  $H(f)$  tells us the phase difference between the output and input signals in the frequency domain. A positive phase indicates the output is phase advanced relative to the input and a negative phase indicates the output is delayed or phase lagged relative to the input. The plot of the gain and phase of  $H(f)$  as a function of frequency is called a Bode plot. Note typically gain is plotted in decibels (dB) in a Bode plot but we simply plot the magnitude. From this plot we can predict the change in output from a perturbation at frequency  $f$ .

To illustrate the concepts of gain and phase we compute the FRF for the LTI system  $\dot{x}(t) = -x(t) + u(t)$ . First we take the Laplace transform of the differential equation which gives us  $sX(s) = -X(s) + U(s)$  where  $U(s)$  and  $X(s)$  denote the Laplace transforms of the input and output signals respectively. Then we can rearrange the equation to solve for  $X(s)$  which yields

$$X(s) = \frac{1}{s+1}U(s)$$

and we call  $H(s) = 1/(s+1)$  the transfer function of the system. Note if we make the substitution  $s = 2\pi if$  where  $f$  is frequency in Hz then  $H(f)$  is the FRF of the system. The gain and phase of  $H(f)$  are shown in Figure 5.2. Note the gain is largest at 0 Hz and then decreases as frequency increases. This means that the output will have smaller

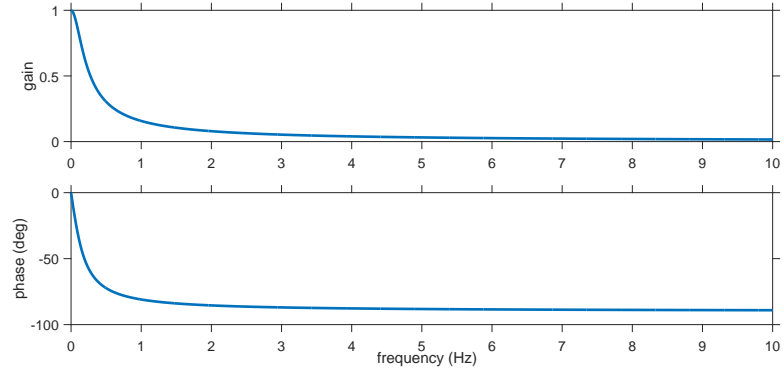


Figure 5.2: Bode plot for the LTI system given by  $\dot{x}(t) = -x(t) + u(t)$ . The gain of the FRF shows that the output will have a smaller amplitude than the input for all frequencies and for large frequencies the output will be almost negligible. The phase of the FRF shows that as the input frequency increases the phase difference between the input and the output approaches  $90^\circ$ .

amplitude than the input signal, with the difference in amplitude increasing for faster input signals. The phase also decreases as frequency increases, indicating that the output signal is behind the input signal and this phase difference limits to a phase lag of  $90^\circ$ . An example of these effects is shown in Figure 5.3 for input frequency 1 Hz. In Figure 5.2 at 1 Hz we see the gain is around 0.15 and the phase is approximately  $-80^\circ$ . In Figure 5.3, after the transient behavior, we see the output  $x(t)$  has amplitude 0.15 and the peak of each cycle occurs approximately  $80^\circ$  after the peak in the input signal  $u(t)$ .

Figures 5.2 and 5.3 illustrate the FRF properties for a simple analytic example. To approximate the FRF for two experimental (or random) signals, we compute the ratio of the power spectral density (PSD), denoted by  $p_{uu}$ , and the cross spectral density (CSD), denoted by  $p_{ux}$ , between the two signals. The two-sided PSD is defined as

$$p_{uu}(f) = \lim_{T \rightarrow \infty} \frac{1}{T} E [ |U_T(f)|^2 ] \quad (5.1)$$

where  $E$  stands for the expected value of the signal (the true mean) and

$$U_T(f) = \frac{1}{T} \int_0^T x(t) \exp(-2\pi i f t) dt$$

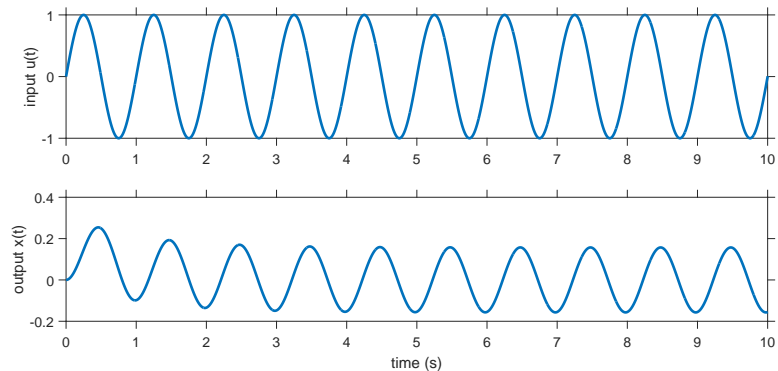


Figure 5.3: Example of the input and output for the LTI system given by  $\dot{x}(t) = -x(t) + u(t)$  for input  $u(t) = \sin(2\pi t)$ . Note the output has the same frequency as the input. The output  $y(t)$  has amplitude around 0.15 and is ahead of the input signal by approximately  $80^\circ$  which is what is predicted by the Bode plot in Figure 5.2.

is the Fourier transform of the signal at frequency  $f$ . Note the frequency step size is determined by  $\Delta f = 1/T$  where  $T$  is the duration of the signal. Since the two-sided PSD is symmetric across negative and positive frequencies, to get the one-sided PSD we multiply (5.1) by 2 and only consider frequencies greater than or equal to 0. We can also compute the cross spectral density (CSD) between two random signals. The two-sided CSD between two signals  $u(t)$  and  $x(t)$  is defined as

$$p_{ux}(f) = \lim_{T \rightarrow \infty} \frac{1}{T} E [\bar{U}_T(f) X_T(f)]. \quad (5.2)$$

The CSD is the Fourier transform of the cross-correlation of the signals  $u(t)$  and  $x(t)$  and we can use the CSD to describe the phase relationship between the two signals as a function of frequency  $f$ . In signal processing, it is typical to subtract the mean of the signal before computing the power spectrum. Then, the PSD can be thought of as the distribution of variance in the signal across a range of frequencies. The range of frequencies is determined by the sampling rate (or time step) of the signal. The power spectrum is computed up to the Nyquist frequency, which is half of the sampling rate. Thus, if we sample the signal at 100 Hz, then the Nyquist frequency is 50 Hz and the two-sided PSD is computed for

frequencies ranging from -50 to 50 Hz. In practice, one should sample the signal at a high enough frequency so that all the power in the signal occurs below the Nyquist frequency to ensure no information is lost. For two random signals  $u(t)$ , input signal, and  $x(t)$ , output signal, the frequency response of the map between them at frequency  $f$  is computed by

$$H(f) = \frac{p_{ux}(f)}{p_{uu}(f)}. \quad (5.3)$$

Thus, if we consider the range of frequencies from 0 Hz to the Nyquist frequency, then we have  $H(f)$  as a function of frequency which maps the input  $U(f)$  to the output  $X(f)$  in the frequency domain.

Since we only have finite length recordings of each signal, the spectral densities are approximated without taking the limit in (5.1) and (5.2). However, since our Fourier transform depends on the signal length  $T$  this estimate can lead to significant errors at larger frequencies. In practice, we split long signals into multiple shorter signals called “windows.” We then compute the spectral density for each window and take the average. This procedure reduces the variability of the estimates. However, the choice of these windows is important. To illustrate this we consider another example with an analytic transfer function. Consider the random signal,  $x(t)$ , whose transfer function from white noise input to output is given by  $H(s) = \omega_0 / (s^2 + 0.5\omega_0 s + \omega_0^2)$  and has duration  $T = 100$  s, sampled at 100 Hz. Since the transfer function has a closed form we can compute the theoretical PSD of the random signal  $x(t)$  which is plotted by the black dashed line in Figure 5.6. Now consider the case where we split the 100 s signal into 10 windows of length 10 s each. Since we consider each point in the window equally we call this a rectangular window whose weights are shown in Figure 5.4a. Using 10 second long rectangular windows we estimate the PSD of the random signal  $x(t)$ , shown in blue in Figure 5.6. Note the

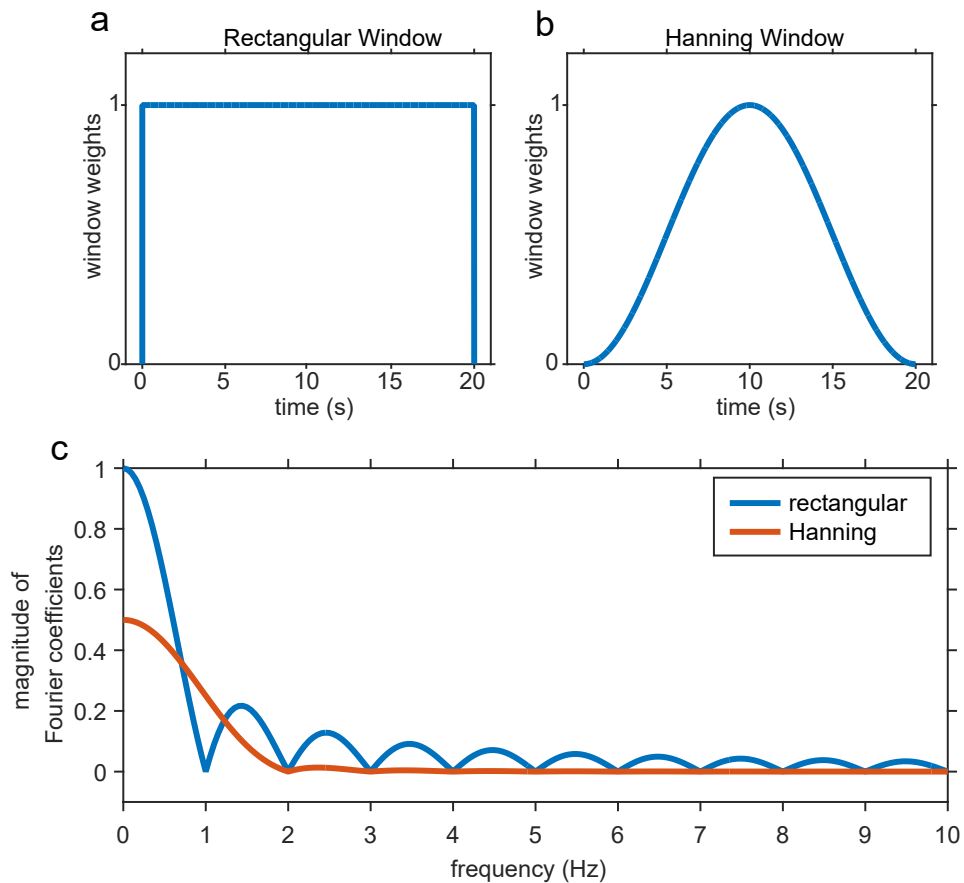


Figure 5.4: Comparison of window weights. a) Rectangular window weights used for computing the power spectral density. All points are weighted evenly. b) Hanning window weights used for computing the power spectral density. Points towards the middle of the window are weighted more than points on either end. c) Fourier transform of window weights for a 20 second long signal sampled at 100 Hz with spectral window length 1 second. The Fourier transform of the rectangular window is plotted in blue and the coefficients are nontrivial for larger frequencies. These are called side-lobes. The Fourier transform of the Hanning window is plotted in red and the coefficients approach zero much faster. Thus, the Hanning windows give a more accurate approximation of the power in the signal.

estimated PSD matches the theoretical PSD well for small frequencies but overestimates the PSD as frequency increases. This is because of the sharp transition in the rectangular window weights. When we “window” the data we are weighting the data points in the time domain, ie.  $x_1(t) = w_1(t)x(t)$  for  $t = 0$  to 10 seconds is the first rectangular window of data. Multiplication in the time domain corresponds to convolution in the frequency domain. Thus, when we take the Fourier transform of the weighted signal it is the same as convolving the Fourier transform of the window weights with the Fourier transform of the unweighted signal. That is  $\mathcal{F}[x_1(t)] = \mathcal{F}[w_1(t)] * \mathcal{F}[x(t)]$ . Thus, the Fourier transform of the window weights will alter our computation of the PSD. The Fourier transform of the rectangular window weights is shown in Figure 5.4c in blue. Note the magnitude of the Fourier coefficients remain large as frequency increases. These bumps are known as “side lobes” and contribute to the overestimate of the PSD for higher frequencies. To reduce the effects of “side lobes” we choose different window weights and split the signal into overlapping Hanning windows. The window weights for Hanning windows are defined by

$$w(t) = \frac{1}{2} \left( 1 - \cos \left( \frac{2\pi t}{T} \right) \right) \quad (5.4)$$

where  $T$  is the length of the window in seconds. Figure 5.4b shows the window weights for a 20 second wide Hanning window. Figure 5.5 illustrates a signal split into 3 Hanning windows of length 20 seconds with 10 seconds overlap between windows. The advantage of using Hanning windows can be seen in Figure 5.4c where the Fourier transform of both rectangular and Hanning windows are shown. For Hanning windows the power dies out much more rapidly as frequency increases. Thus, Hanning windows give a more accurate approximation of the PSD for random signals because there is less power at larger frequencies. Figure 5.6 shows the PSD approximation for 10 second long Hanning windows with 50% overlap plotted in red. The Hanning windows give a much better approximation

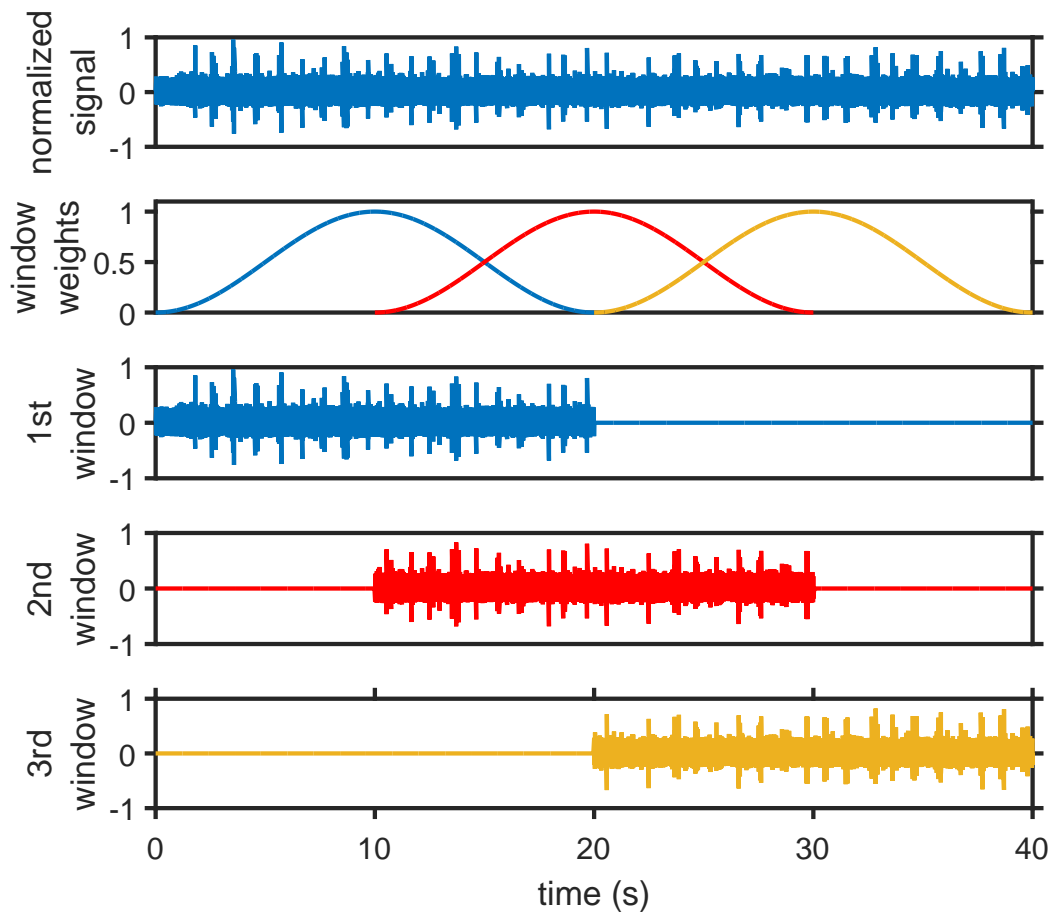


Figure 5.5: Example of a random signal split into three Hanning windows of length 20 seconds with 50% (10 seconds) overlap between windows.

to the true PSD for higher frequencies while the rectangular window estimate is too high for larger frequencies. The same windowing strategies are used to compute the CSD of two random signals. Once we have computed the PSD of the input signal  $p_{uu}$  and the CSD of the input and output signals  $p_{ux}$  we divide the two and compute the FRF as shown in equation (5.3).

We have now shown how to compute the FRF for two random signals. The gain and phase of the FRF describes the change in output for a perturbation to the input signal at

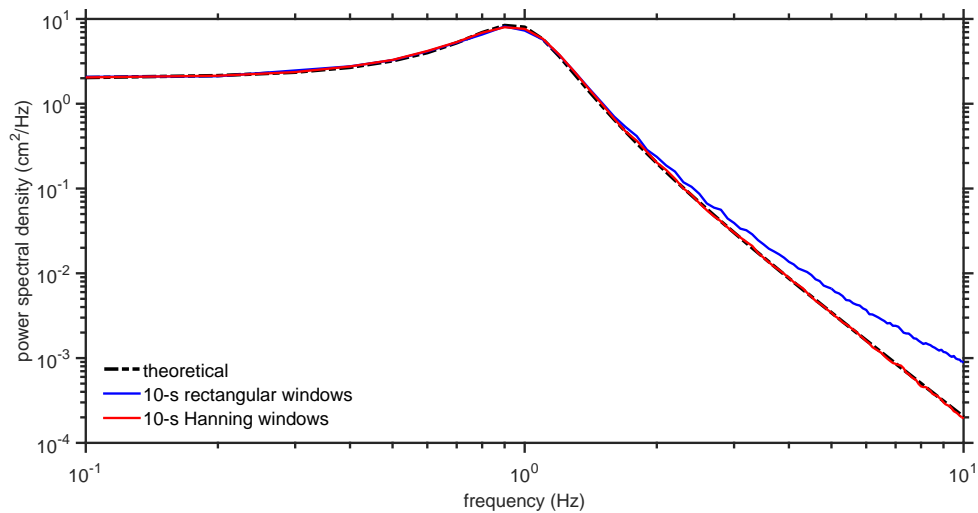


Figure 5.6: Approximation of PSD of known analytic FRF given by  $H(s) = 2\pi/(s^2 + \pi s + 4\pi^2)$ . The true PSD is shown in the black dashed line. PSD for rectangular windows with no overlap is plotted in blue. PSD for Hanning windows with 50% overlap plotted in red. Splitting the signal into Hanning windows with 50% overlap gives a better approximation to the true PSD than rectangular windows with no overlap.

a particular frequency. However, interpreting the gain and phase is not always intuitive in the frequency domain. To more easily interpret the change in output, we convert the FRF to its time domain analogue, the impulse-response function (IRF), via the inverse-Fourier transform. If  $H(f)$  is the FRF for the system and  $h(t)$  is the IRF of the system then we have  $h(t) = \mathcal{F}^{-1}[H(f)]$ . The IRF predicts the change in output from a short pulse perturbation. This can be written as  $x(t) = \int_0^\infty h(\tau)u(t - \tau)d\tau$  where  $h(t)$  defines the IRF. Thus, the output  $x(t)$  is the weighted integral of the input  $u(t)$  at all previous times. Note the output will be affected by a perturbation in the same way no matter what time the perturbation is applied since the system is LTI.

### 5.3 FRF and IRF for Edge Cell Activity

To compute the FRF for the edge cell bending experiments we let  $u(t)$  be the band-limited Gaussian white noise bending signal with frequency band 0 to 10 Hz. This bending signal is plotted in Figure 5.7. We wish to compute the FRF from noisy bending to edge cell activity, but we do not use the raw recording as the output signal. Since we are recording extracellularly, we are recording changes in membrane potential of the region nearby the electrode tip. Thus, we record from potentially multiple neurons and the magnitude of the voltage change depends on the proximity of the neuron to the electrode. Also, the sign of the voltage change could be positive or negative since we are not recording from the cell membrane of an individual neuron. Thus, we choose a threshold above the inherent noise in the recording and find the times where the recording exceeds this threshold. Voltage changes above the chosen threshold represent action potentials. Since the amplitude of the recording does not provide meaningful information about the edge cell response we construct an output signal based only on the timing of the spikes in the recording. This signal is computed as follows. First, we choose a threshold above the inherent noise in the signal and identify spike times where the signal crosses the selected threshold. To eliminate the significance of the amplitude of the recordings, we create a new output signal consisting of Delta functions, placed at the spike times, convolved with a Gaussian. We choose the width of the Gaussian based on the range of frequencies we wish to examine. That is, convolution with a Gaussian of width  $s_w$  defined by  $g_s(t) = \exp(-t^2/(2s_w^2))/(\sqrt{2\pi s_w^2})$  is an acausal filter which can be used to remove some power above a cutoff frequency  $f_c$ , which is defined as the frequency where the gain drops to  $1/\sqrt{e}$ . Note this is not the standard definition of cutoff frequency which uses the drop off value of  $1/\sqrt{2}$ . The FRF of this

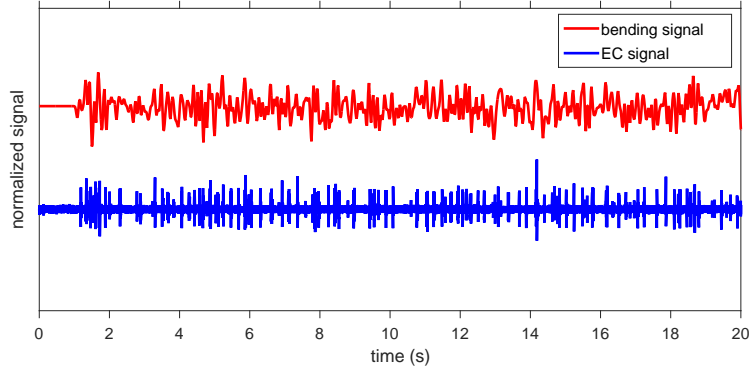


Figure 5.7: Normalized noisy bending signal (red) and experimental edge cell recording (blue).

low-pass filter has phase 0 and gain  $\exp(-f^2/(2f_c^2))$  where the cutoff frequency is given by  $f_c = 1/(2\pi s_w)$ . We now have an input signal  $u(t)$  which describes the bending applied to the spinal cord and an output signal  $x(t)$  which contains information about spike times in response to bending. Using 10 second long Hanning windows with 50% overlap we compute the FRF for the edge cell data. An example of one such FRF is shown in Figure 5.8 in blue. Note the gain is largest for small frequencies and then drops significantly before slowly rising as frequency increases. The phase of the edge cell FRF shows a phase advance that gradually decreases as frequency increases. Note the gradual rise in the gain of the FRF indicates that we did not include a wide enough range of frequencies in our white noise bending signal. If we had completely characterized the edge cell response we should see the gain start to decrease at some frequency where there is no longer a response. More data needs to be collected to fully characterize the edge cell response across a wider range of frequencies. However, we proceed with our analysis in order to approximate the edge cell response and find a model that captures these response properties.

## 5.4 Fitting Frequency Response Function

We know that edge cells respond to both stretch and rate of stretch, but we do not know exactly how this information is relayed from the edge cells back into the CPG. In preliminary simulations we use a linear feedback model of the form  $a_0\kappa + a_1\dot{\kappa}$  where  $\kappa$  denotes the curvature of the segment in the CPG. However, from the frequency response function computed from edge cell recordings, we can get more insight into the important response properties of the edge cells and moreover determine the structure of a model for sensory feedback. The FRF describes the mapping from bending (degrees) to edge cell output (V) in the frequency domain. This means that we can describe the effects, in term of gain and phase, of a perturbation at a given frequency. If we take the inverse Fourier transform of the FRF  $H(s)$ , we get an impulse response function which describes the effects of perturbations in the time domain. This equation will be a non-homogeneous delayed differential equation. This equation can be used in a closed-loop swimming model and will connect the edge cell output to the CPG model.

Using the optimization toolbox in Matlab, we fit an analytic FRF,  $H_a$ , to the FRF of the edge cell data,  $H_{ec}$  using a least squares minimization routine. Thus, our goal is to minimize the following objective function

$$e = \sum_s |H_a(s) - H_{ec}(s)|^2$$

where  $s = 2\pi f$  is the Laplace variable and  $f$  is a vector of input frequencies in Hz. Since we are assuming the mapping is linear time periodic (LTI) the input and output frequencies are the same. That is, a perturbation at frequency  $f$  has affect only on the output at frequency  $f$ . Figure 5.8 illustrates the Bode plot for the fitted transfer function

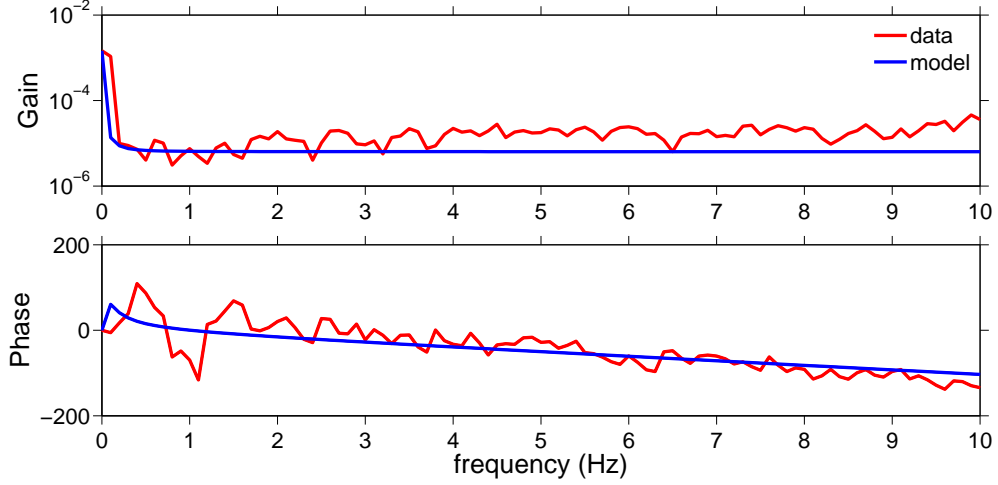


Figure 5.8: Bode plot for edge cell response data and best fit with model transfer function  $H_a(s) = (a_1s + a_0)/(b_2s^2 + b_1s + 1)e^{-\tau s}$ . Analytic transfer function fit to experimental FRF for edge cell response. Parameter values are  $a_1 = -0.0012\text{Vs/deg}$ ,  $a_0 = 0.0015\text{V/deg}$ ,  $b_2 = 2.7 \times 10^{-7}\text{s}^2$ ,  $b_1 = -193.8\text{s}$ , and  $\tau = 0.029\text{s}$ .

$H_a$  defined by

$$H_a(s) = \frac{a_1s + a_0}{b_2s^2 + b_1s + 1}e^{-\tau s} \quad (5.5)$$

and the FRF for the edge cell response. In (5.5) the numerator corresponds to the velocity and position dependence of the output. The denominator represents the the Laplace transform of the ODE which is satisfied by the output signal. The exponential term represents the time delay between the input and output signals where  $\tau$  is the length of the delay in seconds. Note in the time domain  $H_a(s)$  corresponds to the differential equation

$$b_2\ddot{x}(t) + b_1\dot{x}(t) + x(t) = (a_1\dot{u}(t - \tau) + a_0u(t - \tau)) \quad (5.6)$$

where  $u(t)$  is the input signal and  $x(t)$  is the output signal. Thus, from the fitted parameters we now have a non-homogeneous ODE that describes how the edge cell output  $x(t)$  depends on the input bending signal  $u(t)$ . However, we can see in Figure 5.8 that the gain of  $H_a$  does not capture the gain of the edge cell response for larger frequencies.

We could use higher order terms in  $H_a$  to improve this fit but then the corresponding ODE contains higher order derivatives and is more computationally expensive to solve. Additionally, the experimental gain does not decrease as frequency increases to 10 Hz. This indicates that in order to completely characterize the edge cell response we need to use a larger frequency band. That is, we should increase the upper bound of frequencies in our white noise bending signal until the gain of the experimental FRF begins to decrease. However, there are limitations on the bandwidth of the experimental bending signal and more experiments are necessary to determine how large the bandwidth should be.

We have performed noisy bending experiments and recorded edge cell activity where the spinal cord is bent around the center position. However, we were not able to completely characterize the edge cell response for bandwidth 0 to 10 Hz. Additionally, only some units seem to respond linearly to stretch in the spinal cord. Instead of computing the FRF for edge cell activity, we can assume the system is linear time periodic (LTP). This assumption is reasonable since we know both the CPG output and body kinematics during lamprey swimming are periodic. We now consider noisy sinusoidal bending experiments and compute harmonic transfer functions (HTFs) from bending to edge cell activity.

## 5.5 Harmonic Transfer Functions

In the previous section we describe the computation of FRFs, which define a map from an input signal to an output signal in an LTI system. These ideas can be extended to linear time-periodic (LTP) systems where the unperturbed system has a periodic orbit with period  $T_0$  (frequency  $1/T_0 = f_0$ ). Recall that for LTI systems, an input with frequency  $f$  has output only at frequency  $f$ . In LTP systems, the same input can have output at any frequency  $f + kf_0$  where  $k$  is any integer. Thus, we can no longer compute a FRF to

characterize the map from input to output in the frequency domain. Instead of having a single map for each input frequency, we will have an infinite number of maps which describe the output at each frequency. For the LTP case the mapping from input to output in the frequency domain is defined by  $X(f) = \sum_{k=-\infty}^{\infty} H_k(i2\pi f - ik2\pi f_0)U(i2\pi f - ik2\pi f_0)$  where  $H_k$  is called the  $k$ th mode of the HTF. We now need a map that describes each different output frequency  $f + kf_0$ . These modes grouped together can be thought of as a complex-valued matrix where rows represent input frequencies and columns represent output frequencies. The 0th mode of the HTF corresponds to the FRF where the output has the same frequency as the input.

To compute the HTF of an LTP system we use techniques similar to the FRF computation. First, we reorganize the signal into cycles with length  $T$ . We then average the signal across the cycles and this is the mean of our signal. We then use the same approximation as in the linear case to compute the PSD and CSD for the signals. That is, the signal is split into Hanning windows with 50% overlap. The approximation of the PSD for the input signal,  $p_{uu}$  is a complex-valued vector of the power associated with each frequency from 0 to the Nyquist frequency with frequency step size  $1/T$ . The approximation of the CSD,  $p_{ux}(f)$ , is a complex-valued matrix of size  $nf_u \times nf_x$  where  $nf_u$  are the number of input frequencies stored and  $nf_x$  is the number of output frequencies stored. Entries in this matrix,  $p_{ux}^{kj}(f)$ , should be interpreted as the CSD between input frequency  $f + kf_0$  and output frequency  $f + jf_0$ . To compute the harmonic transfer function (HTF) between input  $u(t)$  and output  $x(t)$  we divide the CSD of the two signals by the PSD of the input signal. That is

$$H_{ux}^{(k)}(f) = p_{ux}(f, f + kf_0)/p_{uu}(f) \quad (5.7)$$

where  $H_{ux}^{(k)}$  is a complex-valued vector which describes the input-output map from input

frequency  $f$  to output frequency  $f + kf_0$ . If we write the HTF from  $u(t)$  to  $x(t)$  as a doubly infinite matrix  $H_{ux}(f)$ , where the  $(j, k)$ -th entry is  $H(kj)_{ux}(f + kf_0)$ , then all the usual algebraic manipulations of FRFs for LTI systems can be applied to HTFs for LTP systems.

Again we can convert our frequency domain map,  $H_{ux}$ , to the time domain using the inverse Fourier transform. We denote this time domain map as  $h_{ux}(t_r, t_s)$  where  $t_s$  is the time the stimulus is applied and  $t_r$  is the time the response is measured. This map describes changes in output based on short pulse perturbations similar to the LTI case. However, the response to the pulse now depends on the timing of the pulse relative to the periodic input signal and also when the response is measured. Thus, we call  $h_{ux}(t_r, t_s)$  the phase-dependent impulse response function. We now have a matrix of values where each column represents the change in output to a perturbation applied at a particular phase.

To understand how edge cells fire during swimming, we repeat the bending experiments using a sinusoidal bending signal. This bending signal is more realistic to the activation the edge cells receive during swimming. We see that edge cells fire at specific phases of bending depending on the frequency of the stimulus. An example of the recording from deterministic sinusoidal bending is shown in Figure 5.9a. This response serves as our baseline periodic activity. To compute the HTF for edge cell response, we must perturb the periodic system with band-limited Gaussian white noise. This noise signal is added to the sinusoidal bending signal and the resulting edge cell response is recorded. The recording from one noisy bending trial is illustrated in Figure 5.9b. Note the edge cell response still seems to occur at about the same phase of bending despite the added noise. Before computing the HTF, we again analyze the raw edge cell recordings to find

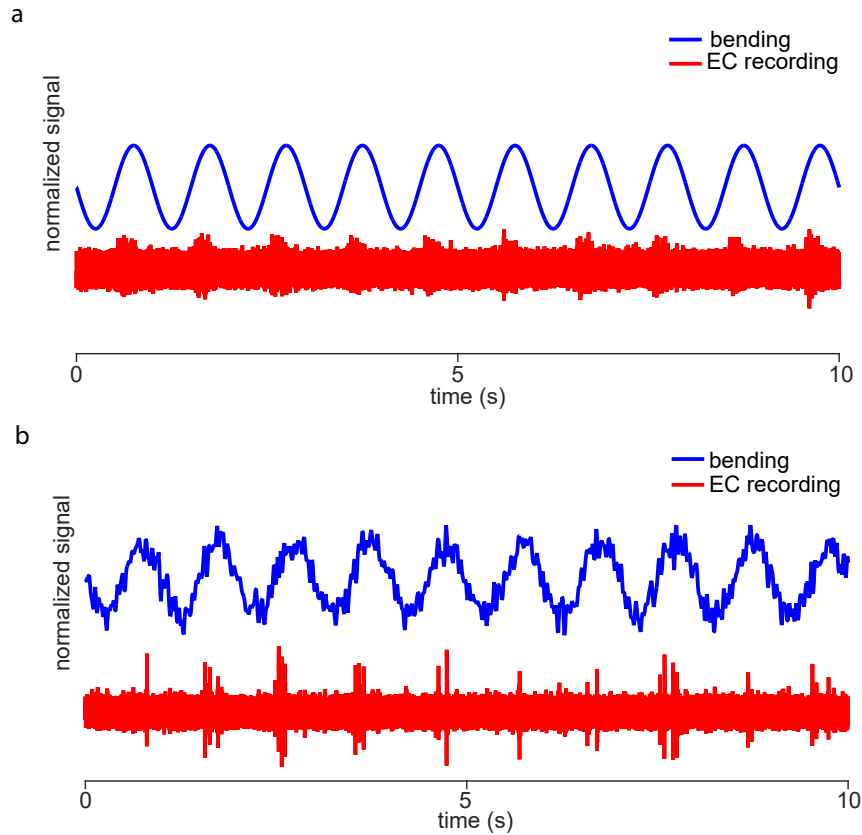


Figure 5.9: Sinusoidal bending and edge cell recordings. a) Normalized sinusoidal bending signal at 1 Hz and the normalized edge cell response recorded from the left lateral tract. b) Normalized noisy sinusoidal bending at 1 Hz and the normalized edge cell recording from the left lateral tract. Note in both recordings the edge cell response occurs towards the peak in bending to the right.

spike times and convolve these times with a Gaussian of width  $s_w = 15$  ms. We then compute the PSD and CSD as described above for 200 second long signals with 20 second long Hanning windows with 50% overlap.

The phase-dependent IRF for one noisy sinusoidal bending experiment is shown in Figure 5.11. Figure 5.11a shows the normalized mean input and output signals. The mean input signal is the mean noisy sinusoidal bending signal which is approximately sinusoidal with bending frequency 1 Hz. The actual bending signal applied the spinal cord had amplitude  $20^\circ$  and the noise had standard deviation of  $5^\circ$ . The mean edge cell activity is

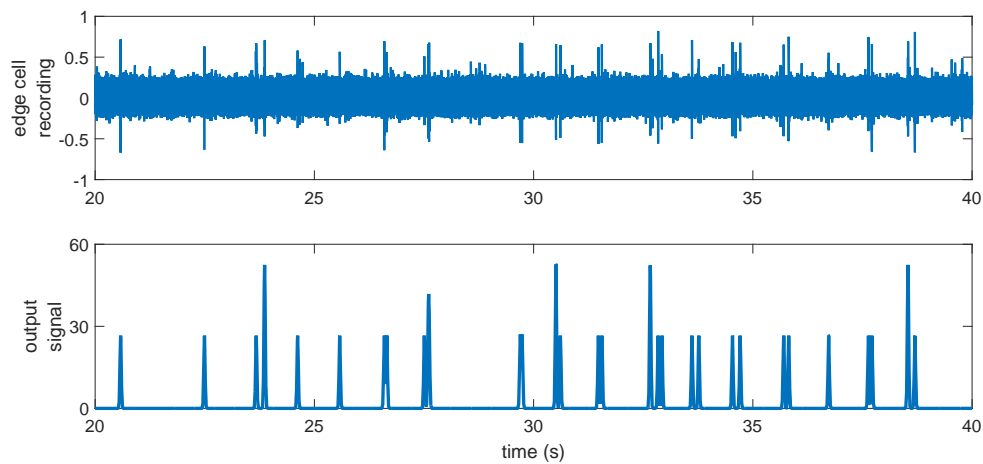


Figure 5.10: a) Recording from left lateral tract in response to noisy sinusoidal bending. b) Output signal used for FRF computation. Spike times found when edge cell recording crossed threshold of 0.4 mV. Spike times then convolved with normalized Gaussians of width 15 ms. Note the larger peaks in the output signal arise from two spikes that occur close together.

the mean of the output signal we compute from the spike times in the recording, shown in Figure 5.10. The darker red regions in Figure 5.11 indicate an increase in response in the same direction as the perturbation. That is, if the spinal cord is bent to the right, we are stretching the left side, and would expect to see the edge cells on the left side activated. Thus, if we perturb while bending is to the right (give extra bending), then we should see an increase in edge cell activity because stretch has been increased on the ipsilateral side. Similarly, the darker blue regions indicate an increase in response in the opposite direction of the perturbation. This means that if we bend to the right side of the body, which would normally excite the edge cells on the left side of the spinal cord, we see a decrease in activity. The green regions indicate there was no change in response. For this recording, we see that the majority of edge cell response occurs at between bending phases 0 and 0.25. This is the only phase where the perturbation alters the edge cell activity and

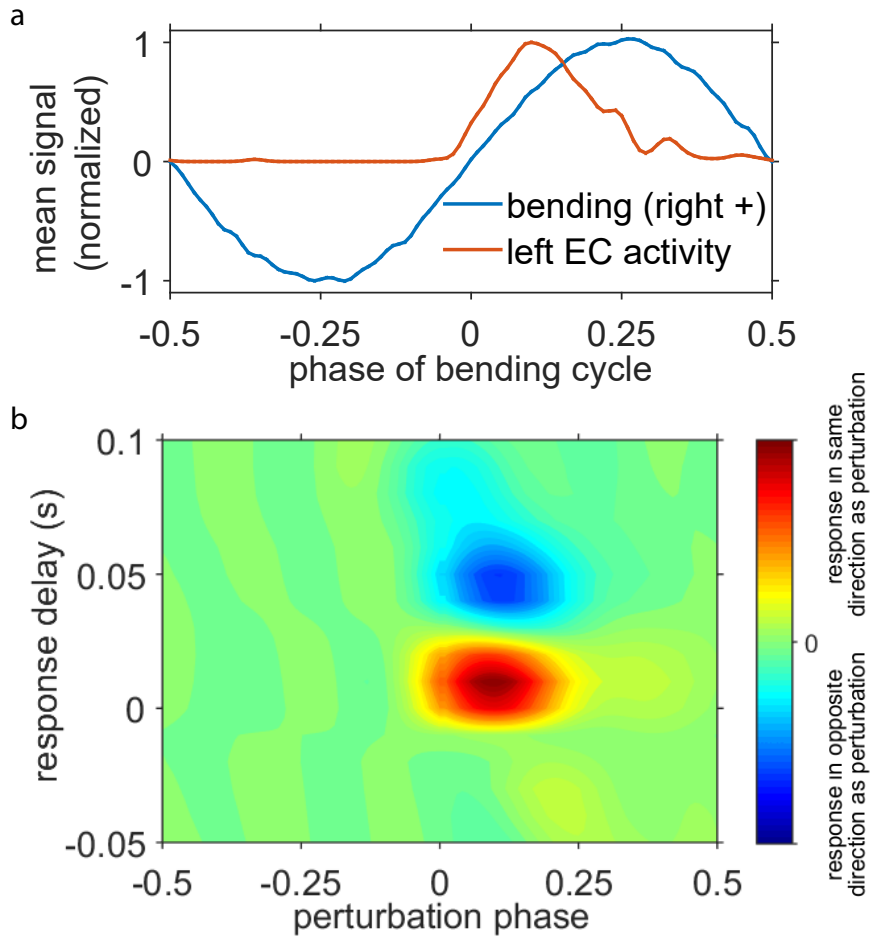


Figure 5.11: Experimental phase-dependent IRF from bending to edge cell activity. a) Normalized mean bending signal and edge cell activity signal. Note bending to the right is positive. b) Phase-dependent IRF from bending to edge cell activity. We only see response to perturbations applied during phases where edge cells are normally active, between phases 0 and 0.25. We see an increase in edge cell activity (red) followed by a decrease in activity (blue).

the effect has very short latency. Note the response to the perturbation appears to come before the perturbation is even applied. This is an artifact of the Gaussian filter we applied to the output signal before computing the HTF. The most interesting response is that a perturbation to the right first increases edge cell activity and which is followed shortly by a decrease in activity. One hypothesis is that this decrease is due to the refractory period of the edge cells which refers to the period after the cells fire where they are not able to be excited again. More experiments will need to be performed to further investigate this activity in response to perturbations.

## 5.6 Modeling the Phase-Dependent Impulse Response

The goal of computing the phase dependent IRF from bending to edge cell activity is to describe the feedback from edge cells to the CPG. From the contour plot in Figure 5.11b we determine the significant edge cell response properties during bending. Specifically, we only see a response to perturbations during bending with positive velocity moving from left to right and we see a short latency increase in activity followed by a decrease in activity. However, the IRF does not give an analytic function that describes the relationship between bending and edge cell response. To model this input-output mapping we compute phase dependent IRFs for various LTP systems. Specifically, we look at LTP systems of the form

$$\ddot{y} + a\dot{y} + ky = b(t)u(t - \tau) \quad (5.8)$$

where  $y(t)$  represents the change in the output signal and  $u(t)$  represents the change in the input signal. Again  $\tau$  represents the time delay between the input and output signals. We consider the case where  $a$  and  $k$  are constant and  $b(t)$  is periodic. The time delay between the input and the output is denoted by  $\tau$ . Note (5.8) is an LTI system when  $b(t)$  is

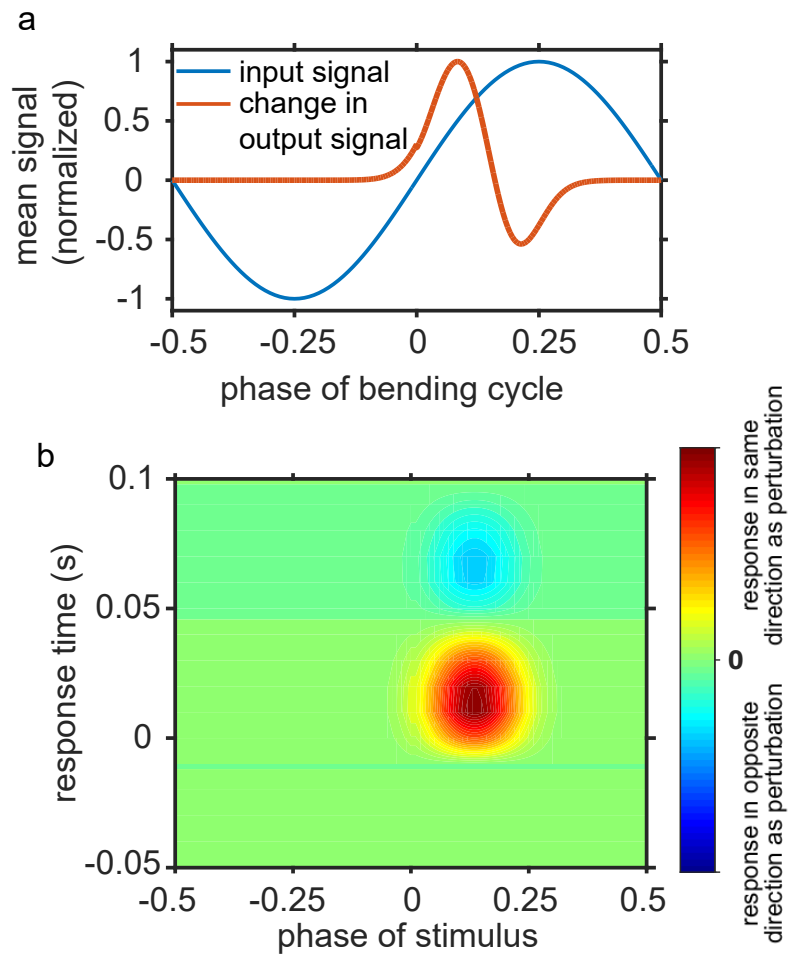


Figure 5.12: Impulse response for  $\ddot{y} + a\dot{y} + ky = b(t)u(t - \tau)$  with  $a = 40$ ,  $k = 4000$ ,  $b(t) = -30((1 + \cos(2\pi t - \pi/4))/2)^{16}$ , and  $\tau = 0.15$ .

constant. Figure 5.12 shows the phase-dependent IRF for input  $u(t) = \sin(2\pi t)$  and output  $x(t)$  which satisfies (5.8) where  $a = 40$ ,  $k = 4000$ ,  $b(t) = -30((1 + \cos(2\pi t - \pi/4))/2)^{16}$ , and  $\tau = 0.15$ . Note the response to perturbations for this function form qualitatively agrees with the experimental IRF for the edge cell data shown in Figure 5.11. Thus, we can use (5.8) to model sensory feedback for the lamprey CPG and qualitatively match the experimental response.

## Chapter 6: **Conclusions and Future Work**

Sensory feedback is an integral part of the locomotor neural network. The CPG can produce periodic neural activity for locomotion without sensory feedback or descending control [19, 68, 3]. However, sensory feedback aids in maintaining steady swimming behavior, especially in the presence of perturbations. We examined the role of sensory feedback, via edge cells, in three contexts: CPG models and entrainment, stochastic entrainment, and edge cell bending experiments.

### 6.1 Modeling Entrainment

CPGs are most commonly represented as chains of coupled oscillators and for the lamprey CPG each oscillator corresponds to an anatomical segment. Each oscillator can be represented with varying degree of biological detail. Motivated by the entrainment analysis of the sinusoidal phase model in which oscillators are connected through sinusoidal coupling functions, we study entrainment ranges in a neural model and a derived phase model. We showed that nonuniform coupling asymmetry in the intersegmental coupling strengths resulted in non-monotonic entrainment ranges as a function of forcing position. This agrees qualitatively with the experimental entrainment ranges measured by Tytell and Cohen [66]. Moreover, since the derived phase model closely approximates the neural model with weak coupling, we also showed that entrainment is lost in the same way in both models. Not only was entrainment lost in the same way, but the derived phase

model preserved the type of bifurcation that occurred where entrainment was lost. Thus, the derived phase model provides a simpler alternative to the neural model yet contains similar entrainment properties. We also can perform similar analytic studies on the effects of intersegmental coupling on analytic bounds of entrainment and how entrainment is lost as done by Previtte et al. [57]. Additionally, the derived phase model can be used as the CPG model in the full model of lamprey swimming. This is important because simulations of the full model consisting of the body, muscles, and fluid dynamics take a long time and the phase model contains less state variables than the neural model.

In these models, we represent the effects of bending via edge cells only in a single oscillator in the chain. That is, we assume that edge cells are active only at the segment where forcing is applied. However, during swimming the edge cells along the entire length of the spinal cord are activated periodically as the body bends. Thus, when we apply forcing to a single segment, intersegmental coupling is responsible for entraining the remaining oscillators in the chain. However, there is experimental evidence that edge cell axons project as far as 15 segments away from the point of bending [33]. Despite our assumption, our models still qualitatively capture the shape of the experimental entrainment range.

## 6.2 Modeling Entrainment with Sensory Perturbations

To better understand the role of sensory feedback during entrainment, we studied the effects of sensory perturbations. Sensory perturbations were incorporated into the entrainment experiments and in the forcing signal for the derived phase model. To create sensory perturbations we added Gaussian white noise to the deterministic sinusoidal bending signal. Experimentally we characterized entrainment by quantifying the variability of

the spike phases in response to noisy bending. In the derived phase model we computed the variability in the relative phases of the oscillators. Recall that when the phase model is entrained, each oscillator has a constant relative phase  $\theta_f - \theta_i$ . The addition of noise to the model will create variation in the relative phase of each oscillator. We see that the noise most strongly affects the oscillator where forcing is applied but drastically decreases in adjacent oscillators. This is due to the relative strengths of the forcing connection and the intersegmental connections. For our simulations we chose the forcing strength  $\alpha_f = 3$  and strong nonuniform coupling asymmetry where ascending connections of length 1 have strength  $\alpha_1 = 0.15$  and descending connections of length 1 have strength  $\alpha_{-1} = 0.03$ . Longer connections have strengths which decay exponentially and follow (2.8). Thus, the noise propagates slightly more to oscillators above the forcing location. However, in both directions the coupling strengths are relatively weak compared to the forcing strength. This assumption agrees with the propagation of noise in the experimental recordings. The variability in spike phases is larger for recordings close to the point of bending and for recordings farther away from the point of bending the variability is not significantly different than the variability seen during deterministic bending. This supports the idea that edge cells deliver information about bending locally and thus, short connections may determine how much influence the sensory information from the edge cells has on the other oscillators in the chain. This result is supported by the relative phases from the experimental recordings. Additionally, noisy bending did not disrupt the CPG signal enough to prevent entrainment when the forcing frequency was close to the intrinsic CPG frequency. Previous models of entrainment did not take into account variability in the forcing signal. We show that both the experimental and computational stochastic entrainment ranges closely agreed with deterministic entrainment ranges for even large levels of noise in the

bending signal. This indicates that the CPG is capable of filtering out noisy sensory input and maintaining a steady rhythmic output despite internal or external perturbations.

### 6.3 Edge Cell Response During Swimming

Entrainment experiments and simulations provided a way to measure the effects of sensory perturbations on CPG output. We know that edge cells are one method of proprioception that detects how the body is stretched during swimming. However, we wish to model how the sensory feedback adjusts the CPG frequency. Thus, we performed several kinds of bending experiments to determine what bending properties are encoded by edge cells. Ramp bending experiments illustrated that particular units within extracellular recordings responded more often to a specific direction of bending. We found units that responded more strongly to bending angle, where the spinal cord was held out to one side, and units that responded more strongly to bending velocity, most often bending away from the recording site. Around half of these units had a significant linear increase in firing rate as bending angle or velocity increased. In addition to bending angle and bending velocity responders, we found units which fired at constant rates across a range of bending velocities. These units are called velocity detectors. Our ramp bending experiments suggest that most units encode either the magnitude of the stretch or the rate of the stretch of the body while some units simply detect that a stretch has occurred. While Hsu et al. [33] showed the distribution of units along the spinal cord that responded to pitch and yaw bending, we classify units based on firing rates during different types of bending. Our results suggest that there could be more than two types of edge cells in the lamprey CPG and that all units do not respond in the same way to stretch.

Since lamprey are anguilliform swimmers, edge cells will be subjected to periodic

stretch and compression during steady swimming. Thus, we perform sinusoidal bending experiments and record edge cell response. While the ramp bending experiments showed that individual units responded to different types of bending, edge cell activity during sinusoidal bending is most often phase locked. That is, the edge cell activity is centered around one particular phase of bending. This activity occurs between the peak of ipsilateral stretch and the maximum rate of stretch. To characterize the mapping from bending to edge cell activity we use a frequency domain technique developed by Jeka and Kiemel [34]. This technique extends the theory of FRF for LTI systems to LTP systems. By adding band-limited Gaussian white noise to the sinusoidal bending signals in our experiments we can compute a phase-dependent IRF. This phase-dependent IRF describes how short pulse perturbations to the bending signals affect the edge cell activity. The edge cell response to perturbations is highly phase-dependent as seen in Figure 5.11. The edge cell activity changes only in response to perturbations that occur during phases where the edge cells are normally activated by bending. Perturbations during these phases cause a rapid increase in edge cell activity shortly followed by a decrease in activity. This decrease in activity could be due to the refractory period of the edge cells or possibly to the inhibition by edge cells with contralateral projections. More data needs to be collected in order to determine the possible mechanisms underlying the increase and decrease in edge cell activity.

The phase-dependent IRF for edge cell experiments is a non-parametric map from bending to edge cell activity that describes how edge cells respond to perturbations during regular sinusoidal bending. From our noisy bending experiments, we saw that only perturbations applied during phases where edge cells are typically active had significant effects on the edge cell activity. For our example recording, this phase occurred between

bending with positive velocity and the peak in bending to the right. Since we record from the left side of the spinal cord, this implies that the total edge cell response during sinusoidal bending is dominated by edge cells with ipsilateral projections that are excited when the spinal cord is bent to the right and the left side is stretched. If a perturbation occurs during this normal edge cell activity then the change in response is characterized by an increase in edge cell firing followed by a decrease. The increase in activity agrees with the experimental results from our ramp bending experiments where an increase in bending velocity or bending amplitude typically caused an increase in edge cell firing rate. The decrease in edge cell activity that follows could occur for several reasons. One hypothesis is that the decrease in response is due to the refractory period of the edge cells. The refractory period refers to the time after a cell fires where it cannot fire again even if it is stimulated. Another hypothesis is that the increase in response is then followed by a decrease because of some inhibitory connections. During swimming, we know that the lamprey CPG units on opposite sides fire in anti-phase. If the increase in edge cell activity then causes an increase in CPG output at the segment, the CPG would want to quickly decrease the output at that segment in order to maintain the correct pattern of activity.

Edge cell responses have been studied in terms of bending to the left and right and bending up and down, but we study the edge cell response during sinusoidal bending. We show that during sinusoidal bending, which mimics the movement seen during lamprey swimming, edge cells respond differently than during periods of linearly increasing stretch. The edge cell response occurs during a single phase of bending, which occurs between the peak bending velocity and peak bending angle when bending away from the recording site. This agrees with previous experiments where edge cells were found to mostly respond to ipsilateral stretch (contralateral bending). Further, we model this response by matching

the phase-dependent IRF with an analytic IRF. This analytic IRF corresponds to an under-damped harmonic oscillator with phase dependent forcing which represents the stretch dependence of the edge cell activity. Moreover, this map can be combined with other open-loop maps in the lamprey swimming system to predict how the closed-loop model would respond to perturbations.

#### 6.4 Future work

Our main goal in studying sensory feedback in lamprey swimming was to find a biologically inspired model which could be used as feedback in a closed-loop model. Currently, Hamlet et al. [29] included a CPG model for activation into a model of swimming which connects a model of muscle and force production, a model of the body kinematics, and a model of the fluid interaction and wake structure. Additionally, they include sensory feedback as a function of curvature and rate of curvature. However, there are many choices for the functional form of the feedback which depends on curvature. Our model of the phase-dependent IRF gives a second order differential equation that can be used to model feedback based on the sinusoidal kinematics of the body during swimming. This functional form provides a starting point for investigating more complicated functions of curvature and its derivative in fully coupled models.

Our edge cell bending experiments are preliminary in the sense that we need to collect more data and average the response across several individuals. We can also compare the response at different bending locations along the spinal cord. We know that entrainment ranges vary non-monotonically as a function of forcing position [66]. This result suggests that sensory feedback acts differently at different locations along the spinal cord. Additionally, Hsu et al. [33] showed that there were differences in edge cell response in

the middle region of the spinal cord. Thus, we predict that the phase-dependent IRF for edge cell activity will differ depending on the location of the bending stimulus. Future edge cell experiments where the bending location varies can inform how sensory feedback differs along the length of the spinal cord. Specifically, how perturbations will affect the strength and sign of the sensory feedback during swimming.

## References

- [1] E. Allgower and K. Georg. *Introduction to Numerical Continuation Methods*. SIAM, Philadelphia, 2003.
- [2] A. Ayali, E. Fuchs, E. Ben-Jacob, and A. Cohen. The function of intersegmental connections in determining temporal characteristics of the spinal cord rhythmic output. *Neurosci.*, 147:236–246, 2007.
- [3] M. B. Berkenblitt, T. H. Deliagina, A. G. Feldman, I. M. Gelfand, and G. N. Orlovsky. Generation of scratching. i. Activity of spinal interneurons during scratching. *J. Neurophysiol.*, 41:1040–1057, 1978.
- [4] Z. Biró, R. Hill, and S. Grillner. 5-HT modulation of identified segmental premotor interneurons in the lamprey spinal cord. *J. Neurophysiol.*, 96:931–935, 2006.
- [5] A. Borgmann, S. L. Hooper, and A. Buschges. Sensory feedback induced by front-leg stepping entrains the activity of central pattern generators in caudal segments of the stick insect walking system. *J. Neurosci.*, 21, 2009.
- [6] H. Broer, R. Roussarie, and C. Simó. Invariant circles in the bogdanov-takens bifurcation for diffeomorphisms. *Ergod. Th. Dynam. Sys.*, 16:1147–1172, 1996.
- [7] J.T. Buchanan. Identification of interneurons with contralateral, caudal axons in the lamprey spinal cord: Synaptic interactions and morphology. *J. Neurophys.*, 47:961–975, 1982.
- [8] J.T. Buchanan. Neural network simulations of coupled locomotor oscillators in the lamprey spinal cord. *Biol. Cybern.*, 66:367–374, 1992.
- [9] J.T. Buchanan and S. Grillner. Newly identified glutamate interneurons and their role in locomotion in the lamprey spinal cord. *Science*, 236:312–314, 1987.
- [10] A.H. Cohen, P.J. Holmes, and R.H. Rand. The nature of the coupling between segmental oscillators of the lamprey spinal generator for locomotion: A mathematical model. *J. Math. Biol.*, 116:3, 1982.
- [11] A.H. Cohen and P. Wallén. The neuronal correlate of locomotion in fish. ‘Fictive swimming’ induced in an in vitro preparation of the lamprey. *Exp. Brain Res.*, 41:11–18, 1980.
- [12] A.H. Cohen and P. Wallén. The neuronal correlate of locomotion in fish. ‘Fictive swimming’ induced in an in vitro preparation of the lamprey. *Exp. Brain Res.*, 41:11–18, 1980.

- [13] N. J. Cowan, M. M. Ankarali, J. P. Dyhr, M. S. Madhav, E. Roth, S. Sefati, S. Sponberg, S. A. Stamper, E. S. Fortune, and T. L. Daniel. Feedback control as a framework for understanding tradeoffs in biology. *Integ. Compar. Biol.*, 54:223–237, 2014.
- [14] N. J. Cowan and E. Fortune. The critical roles of locomotion mechanics in decoding sensory systems. *J. Neurosci.*, 27:1123–1128, 2007.
- [15] N. Ejaz, H. G. Krapp, and R. J. Tanaka. Closed-loop response properties of a visual interneuron involved in fly optomotor control. *Front. Neural Circ.*, 7:1–11, 2013.
- [16] O. Ekeberg. A combined neuronal and mechanical model of fish swimming. *Biol. Cybern.*, 69:363–374, 1993.
- [17] G.B. Ermentrout and N. Kopell. Frequency plateaus in a chain of coupled oscillators. *SIAM J. Math. Anal.*, 15:215–237, 1984.
- [18] N. I. Fisher. *Statistical Analysis of Circular Data*. Cambridge University Press, 1995.
- [19] S. Grillner. On the generation of locomotion in the spinal dogfish. *Exp. Brain Res.*, 20:459–470, 1974.
- [20] S. Grillner. The motor infrastructure: from ion channels to neuronal networks. *Nature Reviews Neurosci.*, 4:573–586, 2003.
- [21] S. Grillner, A. McClellan, and C. Perret. Entrainment of the spinal pattern generators for swimming by mechanosensitive elements in the lamprey spinal cord in vitro. *Brain Res.*, 217:380–386, 1982.
- [22] S. Grillner, A. McClellan, and K. Sigvardt. Mechanosensitive neurons in the spinal cord of the lamprey. *Brain Res.*, 235:1690173, 1981.
- [23] Sten Grillner, Thelma Williams, and Per-Ake Lagerback. The edge cell, a possible intraspinal mechanoreceptor. *Science*, 223(4635):500–503, 1984.
- [24] Sten Grillner, Thelma Williams, and Per-Ake Lagerback. The edge cell, a possible intraspinal mechanoreceptor. *Science*, 223(4635):500–503, 1984.
- [25] L. Guan, T. Kiemel, and A. Cohen. Impact of movement and movement-related feedback on the lamprey central pattern generator for locomotion. *J. Exp. Biol.*, 204:2361–2370, 2001.
- [26] J. Guckenheimer and P. Holmes. *Nonlinear Oscillations, Dynamical Systems, and Bifurcations of Vector Fields*. Springer-Verlag, 1990.
- [27] J. Guckenheimer and P.J. Holmes. *Nonlinear Oscillations, Dynamical Systems and Bifurcations of Vector Fields*. Springer-Verlag, New York, 1983.
- [28] A. Hagevik and A.D. McClellan. Coupling of spinal locomotor networks in larval lamprey revealed by receptor blockers for inhibitory amino acids: Neurophysiology and computer modeling. *J. Neurophys.*, 72:1810–1829, 1994.
- [29] C. Hamlet, L. J. Fauci, and E. D. Tytell. The effect of intrinsic muscular nonlinearities on the energetics of locomotion in a computational model of an anguilliform swimmer. *J. Theor. Bio.*, 385:119–129, 2015.

- [30] W. J. Heitler. Dataview, University of St. Andrews, 2016.
- [31] A. L. Hodgkin and A. F. Huxley. A quantitative description of membrane current and its application to conduction and excitation in nerve. *J. Physiol.*, 117(4):500–544, 1952.
- [32] F.C. Hoppensteadt and E.M. Izhikevich. *Weakly Connected Neural Networks*. Springer-Verlag, New York, 1997.
- [33] L. Hsu, P. V. Zelenin, S. Grillner, G. N. Orlovsky, and T. G. Deliagina. Intraspinal stretch receptor neurons mediate different motor responses along the body in lamprey. *J. Comp. Neurol.*, 521:3847–3862, 2013.
- [34] J. J. Jeka and T. Kiemel. Using perturbations to probe neural control: from standing to walking. *Dynamic Walking*, 2015.
- [35] O. Kiehn. Locomotor circuits in the mammalian spinal cord. *Ann. Rev. Neurosci.*, 29, 2006.
- [36] T. Kiemel and A. Cohen. Estimation of coupling strength in regenerated lamprey spinal cords based on a stochastic phase model. *J. Computat. Neurosci.*, 5:267–284, 1998.
- [37] T. Kiemel, K.M. Gormley, L. Guan, T.L. Williams, and A.H. Cohen. Estimating the strength and direction of functional coupling in the lamprey spinal cord. *J. Comput. Neurosci.*, 15:233–245, 2003.
- [38] N. Kopell and G.B. Ermentrout. Symmetry and phaselocking in chains of weakly coupled oscillators. *Comm. Pure Appl. Math.*, 39:623–660, 1986.
- [39] N. Kopell and G.B. Ermentrout. Coupled oscillators and the design of central pattern generators. *Math. Biosci.*, 90:87–109, 1988.
- [40] N. Kopell, G.B. Ermentrout, and T.L. Williams. On chains of oscillators forced at one end. *SIAM J. Appl. Math.*, 51:1397–1417, 1991.
- [41] N. Kopell, W. Zhang, and G.B. Ermentrout. Multiple coupling in chains of oscillators. *SIAM J. Math. Anal.*, 21:935–953, 1990.
- [42] Y. Kuramoto. *Chemical Oscillations, Waves, and Turbulence*. Springer-verlag, Berlin, 1984.
- [43] M. Lewicki. A review of methods for spike sorting: the detection and classification of neural action potentials. *Network: Computation in Neural Systems*, 9(4):R53–R78, 1998.
- [44] A. F. Lovegrove, L. M. Moroz, and P. L. Read. Bifurcations and instabilities in rotating, two-layer fluids: II beta-plane. *Nonlinear Proc. Geophys.*, 9:289–309, 2002.
- [45] M. S. Madhav, S. A. Stamper, E. S. Fortune, and N. J. Cowan. Closed-loop stabilization of the jamming avoidance response reveals its locally unstable and globally nonlinear dynamics. *J. Exp. Biol.*, 216:4272–4284, 2013.

- [46] R. Mahmood, C. E. Restrepo, and A. El Manira. Transmitter phenotypes of commissural interneurons in the lamprey spinal cord. *Neurosci.*, 164:1057–1967, 2009.
- [47] N. Massarelli, G. Clapp, K. Hoffman, and T. Kiemel. Entrainment ranges for chains of forced neural and phase oscillators. *J. Math. Neurosci.*, 2016.
- [48] A. D. McClellan. Brainstem command system for locomotion in the lamprey: localization of descending pathways in the spinal cord. *Brain Res.*, 457(2).
- [49] A. D. McClellan and A. Hagevik. Coordination of spinal locomotor activity in the lamprey: Long-distance coupling of spinal oscillators. *Exp. Brain Res.*, 126(1):93–108, 1999.
- [50] A. D. McClellan and K. Sigvardt. Features of entrainment of spinal pattern generators for locomotor activity in the lamprey. *J. Neurosci.*, 8:133–145, 1988.
- [51] A.D. McClellan and W. C. Jang. Mechanosensory inputs to the central pattern generators for locomotion in the lamprey spinal cord: Resetting, entrainment, and computer modeling. *J Neurophysiol*, 70:2442–2454, 1993.
- [52] D. L. McLean, M. E. Higashijima, and J. R. Fetcho. A topographic map of recruitment in the spinal cord. *Nature*, 446(7131), 2007.
- [53] N. Mellen, T. Kiemel, and A.H. Cohen. Correlational analysis of fictive swimming in the lamprey reveals strong functional intersegmental coupling. *J. Neurophys.*, 73(3):1020–1030, 1995.
- [54] J. Neu. Large populations of coupled chemical oscillators. *SIAM Journal of Applied Math*, 38(2):305–316, 1980.
- [55] J. Neu. The method of near-identity transformations and its applications. *SIAM Journal of Applied Math*, 38(2):189–208, 1980.
- [56] K. G. Pearson and S. Rossignol. Fictive motor patterns in chronic spinal cats. *J. Neurophysiol.*, 66(6):1874–1887, 1991.
- [57] J. Previte, N. Sheils, K. Hoffman, T. Kiemel, and E. Tytell. Entrainment ranges of forced phase oscillators. *J. Math. Bio.*, 62:589–603, 2011.
- [58] G. Viana Di Prisco, P. Wallen, and S. Grillner. Synaptic effects of intraspinal stretch-receptor neurons mediating movement-related feedback during locomotion. *Brain Res.*, 530:161–166, 1990.
- [59] G. Viana Di Prisco, P. Wallen, and S. Grillner. Synaptic effects of intraspinal stretch-receptor neurons mediating movement-related feedback during locomotion. *Brain Res.*, 530:161–166, 1990.
- [60] A. Roberts, S. R. Soffe, E. S. Wolf, M. Yoshida, and F. Y. Zhao. Central circuits controlling locomotion in young frog tadpoles. *Ann. N.Y. Acad. Sci.*, 860:19–34, 1998.
- [61] E. Roth, S. Sponberg, and N. Cowan. A comparative approach to closed-loop computation. *Curr. Op. in Neurobio.*, 25:54–62, 2014.

- [62] C.M. Rovainen. Synaptic interactions of identified nerve cells in the spinal cord of the sea lamprey. *J. Compar. Neurol.*, 154:189–206, 1974.
- [63] C.M. Rovainen. Neurobiology of lampreys. *Physiol. Rev.*, 59:1007–1077, 1979.
- [64] D. Ryczko, R. Dubuc, and J. Cabelguen. Rhythmogenesis in axial locomotor networks: An interspecies comparison. *Prog. in Brain Res.*, 187:189–210, 2010.
- [65] K. A. Sigvardt. Modulation of properties of neurons underlying rhythmic movements in vertebrates. *Semin. Neurosci.*, 1:55–65, 1989.
- [66] E. D. Tytell and A. H. Cohen. Rostral versus caudal differences in mechanical entrainment of the lamprey central pattern generator for locomotion. *J. of Neurophys.*, 99(5):2408–2419, 2008.
- [67] P. L. Varkonyi, T. Kiemel, K. A. Hoffman, A. H. Cohen, and P. Holmes. On the derivation and tuning of phase oscillator models for lamprey central pattern generators. *J. Comp. Neurosci.*, 25(2):245–261, 2008.
- [68] C. Vidal, D. Viala, and P. Buser. Central locomotor programming in the rabbit. *Brain Res.*, 168:57–73, 1979.
- [69] P. Wallen, O. Ekeberg, A. Lansner, L. Brodin, H. Traven, and S. Grillner. A computer-based model for realistic simulations of neural networks. ii. the segmental network generating locomotor rhythmicity in the lamprey. *J. Neurophys.*, 68:1939–1950, 1992.
- [70] P. Wallen and T. Williams. Fictive locomotion in the lamprey spinal cord *in vitro* compared with swimming in the intact and spinal animal. *J. Physiol.*, 347:225–239, 1984.
- [71] J. C. Weeks. Neuronal basis of leech swimming: separation of swim initiation, pattern generation, and intersegmental coordination by selective lesions. *J. Neurophysiol.*, 45(4), 1981.
- [72] T.L. Williams. Phase coupling by synaptic spread in chains of coupled neuronal oscillators. *Science*, 258:662–665, 1992.
- [73] T.L. Williams, K.A. Sigvardt, N. Kopell, G.B. Ermentrout, and M.P. Remler. Forcing of coupled nonlinear oscillators: Studies of intersegmental coordination in the lamprey locomotor central pattern generator. *J. Neurophys.*, 64:862–871, 1990.
- [74] T.L. Williams and P. Wallén. Fictive locomotion in the lamprey spinal cord *in vitro* compared with swimming in the intact and spinal animal. *J. Physiol.*, 347:225–239, 1984.
- [75] D. M. Wilson. The central nervous control of flight in a locust. *J. Exp. Biol.*, 38(2), 1961.

